M. Rueda Ruiz

Mechanical testing and quantification of crack healing in self-healing yttria-stabilized zirconia thermal barrier coating

TU Delft

Mechanical testing and quantification of crack healing in self-healing yttria-stabilized zirconia thermal barrier coating

By

M. Rueda Ruiz

Novel Aerospace Materials group
Aerospace Structures and Materials department
Faculty of Aerospace Engineering

in partial fulfilment of the requirements for the degree of

Master of Science
in Aerospace Engineering

at the Delft University of Technology,
to be defended publicly on Friday November 25, 2016 at 02:00 PM.

Thesis committee:

Chairman:

Prof. Dr. Ir. Sybrand van der Zwaag

Members:

Dr. Ir. Wim G. Sloof (Daily supervisor)

Dr. Sergio Turteltaub

This thesis is confidential and cannot be made public until December 31, 2017.

Contents

1. Introduction

2. Theoretical background

3. Experimental procedure

4. Results and discussions

5. Conclusions and recommendations

Abstract

Thermal barrier coatings (TBC) are often applied to hot components of modern turbojet engines. These coatings increase the performance of the engine and enhance the lifetime of its structural components. Thus, improving the TBC lifetime is related with a reduction of maintenance costs and increased reliability. As an alternative to conventional design approaches, a self-healing mechanism is implemented in the TBC material. To this end, alumina encapsulated $MoSi_2B$-based YSZ composites were prepared via spark plasma sintering. First, a qualitative study of the crack healing behaviour was conducted using an indentation technique. In most of the cases, indentation cracks fracture the particles in line with the crack path. Then, a sufficient particle-matrix interface strength exists. Upon oxidation at 1100 ºC for 1, 4 and 16 h in laboratory air, the fractured particles oxidize and form glassy SiO_2, that filled the crack. It has been observed that the SiO_2 further reacts with the YSZ matrix and forms a well-bonded healing product, $ZrSiO_4$.

As a second step, a quantitative characterization of the recovery of load bearing capability for the self-healing TBC was performed. For this purpose, two novel mechanical test methods were developed to create a controlled crack that can be stopped, healed and re-tested. This enables to measure in the same specimen the virginal, residual and healed strength of the material. These two set-ups are the Brazilian Disc (BD) test and the Wedge-Loaded Double Cantilever Beam (WL-DCB) test. The application of both the WL-DCB and BD test to the self-healing TBC material was successful because the growth of a crack could be controlled in the brittle material. The WL-DCB test is potentially more suitable for quantification of recovery of load bearing capability. The BD test is more straightforward for determining strength of the material. Application of this BD test to benchmark YSZ material gave a strength value of around 550 MPa, which is accordance with previously reported values for this material.

Following the successful achievement of controlled cracking with both methods, the quantification of load bearing capability in the healed material remains an issue of future work.

Acknowledgements

This master thesis is the product of almost one year of work and it has been a great learning experience that I am sure it will be very helpful in my future career. I am also sure that I could not have accomplished it without the collaboration of all the people that helped me throughout the way, so I would like to dedicate some words to all of them.

First of all, I would like to express my gratitude to my supervisor and chair of my graduation committee Prof. Sybrand van der Zwaag. I want to thank him for the great opportunity that he gave me when he proposed me this interesting and challenging topic for the master thesis. Although I was a bit confused when we had our first meeting for talking about a thesis topic, I think he could see what my potential interests could be and introduced me to this exciting world of high temperature materials and, more in particular, the field of self-healing ceramics. I must say that I am really glad he introduced me to this topic. Also, I would like to thank him for his guidance during the thesis and his very inspiring feedbacks and comments.

I would like to thank my direct supervisor and mentor Dr. Ir. Wim Sloof. The first thing that impressed me was his closeness towards his students and his patience. I was very surprised the first time I saw him coming to the lab to help me with some problem I had. I appreciate all the opportunities I had of learning from him. I want to thank him for teaching me that in research it is always important to be optimistic and that “every problem is a solution”. I also would like to express my gratitude because of all the time that he invested in reading and giving me feedback on the thesis report, and all the formal and informal meetings we had along the thesis.

I also appreciate very much the guidance of my daily supervisor Alexandra L. Carabat for investing so much time in helping me with the thesis, teaching me how to use most of the laboratory equipment and introduce me to the principles of materials characterization and, in general, materials research. I hope her good luck with the completion of her master thesis.

I would like to express my gratitude to Dr. Toshio Osada. I very much appreciate the incalculable amount of time that we have spent together having interesting discussion about the mechanical behaviour of materials, materials for high temperature application and other related topics. I have learnt a lot of new things from him and he really made my thesis experience much better. I want to thank him that he helped me with the preparation of the mechanical test set-ups and his wise advises about how to present the results of my thesis.

I want to express my gratitude to Hans Brouwer and Kees Kwakernaak for his assistance in the lab and also their mentoring. Especially to Kees, for teaching me how to use the SEM, EDS and the Leica sputter coater. I appreciate the help of the people from the X-Ray Diffraction facility as well: Ruud Hendrikx, Richard Huizenga and Niek van der Pers. I extend my gratitude to Sander van Asperen and Dr. Ton Riemslag for helping me in the optical microscopy lab and the mechanical lab, respectively.

The help of Dr. Branko Savija is very much appreciated too, regarding the use of the nanoindentation equipment in the Microlab of Civil Engineering. I also want to thank Prof. Erik Schlangen for letting me use his facilities.

The several meetings and discussions with Dr. Sergio Turteltaub, Jayaprakash Krishnasamy and Sathis Ponnusami regarding numerical modelling and the connection with the test results have been very interesting too and of great value. I thank them for the advises and inputs for the mechanical tests and for the several simulations they did.

The support of all my colleagues from the 4th floor of the MSE department is very much appreciated. Especially Sandi, because our theses were connected by the same European project so we could help each other in many occasions and have interesting discussions. Also, although I have not worked much there, I thank the people from NOVAM group for the good times I had.

Finally, I would like to thank my family and friends for their support during all these years of university, both in Madrid and Delft.

Delft, 14 November 2016

1 Introduction

1.1. Self-healing thermal barrier coating

Thermal barrier coatings (TBCs) are applied to components in the hot section of turbine engines of aircrafts or power plants. These components comprise blades, vanes and combustion chambers. The implementation of thermal barrier coatings was a respond for the need of more efficient engines that reduce CO_2 emissions and fuel consumption. Alternatively, thermal barrier coatings may enhance the lifetime of components if the performance is kept the same than without coating (2). The efficiency of turbojets increases for higher temperatures of the combustion chamber, but this is limited by the maximum operation temperature of materials used. With the development of thermal barrier coatings, a temperature gradient of 100-300ºC (depending on the coating thickness) can be achieved. The TBC system consists of three layers: the top coat, directly in contact with air, that provides thermal insulation of the metallic substrate. The second layer is the bond coat and it provides an efficient oxidation resistance for the substrate material, which is necessary because the top coat is oxygen-transparent. Besides, the bond coat is used for improving adhesion of the top coat to the substrate. The third layer is the thermally grown oxide (TGO), located in the interface between the top coat and the bond coat. It is normally a layer of slow-growing alumina formed because of the oxidation of the bond coat during service. Beneath these layers there is the substrate, which is normally a nickel-based or cobalt-based superalloy. This is the structural element and it sometimes incorporates an internal air cooling system that makes possible to use the turbine at even higher temperature (3) (4).

Among all the layers of the coating system the top coat is the one that provides the thermal insulation. Yttria-stabilized zirconia (YSZ) was appointed as the optimum material for the top coat because of its low thermal conductivity at high temperature, relatively high thermal expansion coefficient, which is advantageous because the difference with the alloy beneath is lower than for other ceramics; and its low density. Other advantages of YSZ are its high melting point (around 2700ºC), its high resistance to ambient and hot corrosion, and high hardness that makes it a good candidate for an erosive environment (4) (5). There are currently two methods for producing the YSZ top coat. One is Air-plasma spraying (APS), in which the powders are melted, accelerated to high velocity, sprayed directly on the surface and rapidly solidified when impacting the substrate. The final microstructure is a pile of "splats" (flattened grains) with pores and microcracks parallel to the surface. Typically, these coatings have a thickness of 300-600 µm. They are commercially more attractive because of the lower production cost and the lower thermal conductivity. However, they are very prone to growth of damage parallel to the surface (4) (6). The other production method is Electron-beam physical-vapor deposition (EB-PVD), in which vapor is generated by heating the material with an electron beam in a vacuum chamber and it condensates onto the substrate. The resultant microstructure is a fine first layer of equiaxed grains in contact with the substrate. The second layer has a columnar structure in which each grain grows normal to the surface and they are separated by nanopores. These TBCs have good adhesion and longer lifetime compared with APS-TBCs. However, top coats prepared by EB-PVD have higher thermal conductivity and are thinner (around 125 µm). Besides, it is more expensive than APS so it is commercially less interesting (4) (6).

Premature failure of the top coat layer may lead to high local temperature in the superalloy beneath the coating causing failure of the component. Therefore, YSZ-TBCs have been subject of extensive research, both for identification of the main failure mechanisms and the ways to enhance its lifetime. The most critical failure mechanism is the growth of the TGO layer between the bond coat and the top coat, that is accelerated because of the presence of a small amount of undesirable oxides such as Cr_2O_3. Upon cooling from the service temperature in-plane compressive stresses will develop in the TGO because of the lower thermal expansion coefficient as compared with the bond coat. Microcracks will nucleate in the geometric imperfections and coalesce until final failure (6) (7). Additionally, for APS-TBCs failure is enhanced due to the undulated shape of the interface bond coat-top coat, that is necessary to improve adherence between both layers. Out-of-plane stresses develop in the interface TGO-Top coat due to the mismatch of thermal expansion coefficient and the undulated interface. Regarding the enhancement of lifetime, most of the research went in the direction of traditional design approaches focused on making the material tougher or stronger. Recently, a new approach for improvement of lifetime in the YSZ-TBC was proposed based on the implementation of an extrinsic self-healing mechanism in the material by addition of sacrificial healing particles in the lower part of the top coat, where damage normally appears.

The self-healing mechanism implemented in the YSZ-TBC is based on damage-triggered high temperature oxidation of the sacrificial particles that produce a flowing healing product that fills the cracks and forms a well-adhered compound by reaction with the YSZ matrix. High temperature oxidation is a degradation mechanism of materials; however, if the oxidation can be controlled by design it is possible to extract great advantages from this phenomenon. A successful design of a self-healing ceramic implies having a crack filled with a well adhered crystalline solid with same or higher strength as the base material (8) (9). The mechanism should only be triggered when oxygen coming from the crack reacts with the healing agent. For extrinsic self-healing ceramics based on sacrificial healing particles additional requirements must be fulfilled. The healing reaction must be only triggered when a crack goes through the healing particle (local, temporary mobility (10) (11)), the healing agent should turn into a flowing substance when reacting with oxygen that fills the crack and it should turn into a solid load bearing material by solid state reaction with the matrix material (8).

The material used for the healing particles is $MoSi_2$ with additions of boron and aluminium. $MoSi_2$ was chosen because of its compatible CTE and because it remains solid at the service temperature in the absence of oxygen. Upon exposure to oxygen at service temperature it forms amorphous SiO_2 (viscous) and volatile Mo-oxides (8). The objective of boron is to increase the fluidity of the amorphous SiO_2 formed during oxidation of the healing particles so that the oxide product can flow into the crack gap and react with the zirconia matrix to form the final healing product, $ZrSiO_4$ (12). The addition of aluminium aims to promote the formation of an oxygen-impermeable protective alumina shell at the interface between the healing particles and the matrix. During manufacturing and further annealing treatment at low oxygen partial pressure P_{O_2} the aluminium in the healing particles should deplete and react in the interface to form a uniform and robust aluminium oxide Al_2O_3 layer. In this way, the healing mechanism will be only triggered by a crack that opens the shell.

A crucial step in the design of the self-healing thermal barrier coating is the quantification of healing efficiency for having an idea of the degree of lifetime improvement. Since the self-healing principle for the YSZ-TBC aims to heal cracks and delay the mechanical failure of the coating, the best way to quantify the healing efficiency is to determine the recovery of load bearing capability in the material by mechanical testing. This is specially challenging in self-healing ceramics because of the low fracture toughness. This makes it difficult to create controlled cracks that can be stopped, healed and retested again. Other authors have addressed this issue by using 3 or 4-point bending set-ups and creating artificial damage with indentation (13) (14) (15). The approach based on 3 and 4-point bending with indentation damage consists on testing three sets of samples: one set of samples without indentation damage, other set with indentation damage and a third set with indentation damage and healing. The comparison of the three strengths provides a quantification of the crack-healing. However, it remains an issue the fact that the strength from three different specimens is being compared for quantifying healing of the material. A more accurate quantification can be achieved if the recovery of load bearing capability is measured in a unique specimen and the way to do this is by creating a controlled crack in the specimen that can be stopped, healed and retested. Although the achievement of controlled and slow-growing cracks in mechanical test set-ups for ceramics is quite challenging, by playing with the design of the specimen and test set-up it is possible to achieve satisfactory results.

Two novel mechanical test methods have been proposed and developed for quantification of crack healing by successfully creating controlled and slow-growing cracks that can be healed and retested. These are two non-conventional tests modified from two already-existing methods, namely: the Brazilian Disc (BD) test and the Wedge-Loaded Double Cantilever Beam (WL-DCB) test.

1.2. Research objectives

The main objective of this project is to develop methods to assess quantitatively crack healing in ceramics; and, more specifically, ceramics used for thermal barrier coatings. This will be achieved by:

- Development of the Brazilian Disc test and the Wedge-Loaded Double Cantilever Beam test for quantification of healing efficiency in self-healing ceramics and application of these set-ups (proof of concept) to the self-healing yttria-stabilized zirconia thermal barrier coating. In addition, the combination of the test results with modelling based on Finite Element simulations should provide accurate values for the strength and fracture toughness of the virginal, damaged and healed material.

Apart from the main research objective of this work, there are two other complimentary objectives:

- Determine the mechanical properties of composites made of yttria-stabilized zirconia with molybdenum disilicide based healing particles by means of depth-sensing indentation techniques.

- Qualitative proof of concept of the self-healing mechanism in the YSZ-MSBA composite by means of studying the healing behaviour of material in which artificial damage has been introduced by indentation.

For these studies the yttria-stabilized zirconia with molybdenum disilicide based healing particles composites were manufactured by Spark Plasma Sintering (SPS).

1.3. Outline of chapters

Chapter 2 compiles a theoretical background necessary for understanding the results presented in this thesis. Chapter 3 summarizes the experimental procedures and equipment used during the project. Chapter 4 addresses the analysis of microstructure, composition and elemental analysis of the TBC composite and the outcomes of the qualitative crack-healing study on the self-healing composite. Next, the results of the mechanical characterization of the YSZ-MSBA composite are presented. First, the results of elastic modulus and hardness determination. Finally, the strength and fracture toughness of the composite are studied by analysis of the results of the BD and WL-DCB tests. The main conclusions and outcomes of the project are summarized in Chapter 5.

2 Theoretical background

2.1. Mechanical properties of brittle materials

In this section an introduction to the mechanical properties of brittle solids is given. However, most of the models and explanations described can be extended to other families of materials.

2.1.1 Elastic behaviour of solids

The elastic behaviour of solids describes the ability of recovering the initial shape upon unloading from a deformed state (1). Normally the elastic behaviour of materials is associated with small deformations, although the order of magnitude depends on the type of material. The elastic behaviour of materials can be described by Hooke's law, which is a simple linear relation between stress and strain:

$$\sigma_{ij} = C_{ijkl}\varepsilon_{kl} \tag{1}$$

σ_{ij} is the stress tensor, ε_{ij} is the strain tensor and C_{ijkl} is the tensor of elastic constants. This is the most general relation, but a simplification can be made for polycrystalline solids by assuming that the material is macroscopically isotropic (same properties in all directions). In this case the elastic behaviour of the material is defined by the Young's modulus (E), shear modulus (G) and Poisson's ratio (ν). Another parameter that describes the linear elastic region of isotropic materials is the bulk modulus (K) that defines the elastic response of a solid deformed by isostatic pressure. These moduli are related by these simple relations (16):

$$E = \frac{3G}{1 + G/3K} \qquad G = \frac{E}{2(1+\nu)} \qquad K = \frac{E}{3(1-2\nu)} \tag{2}$$

The previously stated material properties E, G, K and ν define the macroscopic elastic behaviour of isotropic materials, however the elasticity of materials is directly related to the atomic structure. It is an intrinsic material property that ideally does not depend on the microstructure, unlike strength or hardness which are material properties depending on the microstructure.

Many authors have modelled the elastic behaviour of solids at molecular level as atoms connected by springs and following this relation:

$$F = S_0(d - d_0) \tag{3}$$

In the previous relation F is the atomic force that tends to pull together or push away two atoms (compression/tension) and it is directly related with the macroscopic force applied on the solid. S_0 is the stiffness of the atomic bond. d_0 is the equilibrium distance between atoms (lattice parameter in the case of crystal structure) and d is the interdistance between atoms at a certain force F. Dividing in both sides of the previous relation by d_0^2 and assuming that F/d_0^2 is the stress of the bond and $(d-d_0)/d_0$ is the strain of the bond, then by comparing with the Hooke's law it can be concluded that Young's modulus can be approximated by the following relation:

$$E = \frac{S_0}{d_0} \tag{4}$$

This is a simple relation, but it has very important consequences. The stiffer the atomic bond and the smaller the atomic interdistance (lattice parameter) the larger the Young's modulus will be and hence the stiffer the material.

2.1.2 Effect of microstructure on elastic behaviour: porosity and dispersed particles

In the previous section, it has been stated that the elastic modulus is an intrinsic material property that does not depend on the microstructure, unlike strength or hardness. This is true when considering a microstructure formed just by phases of the same material (neglecting the effect of texture), however there are many cases in which second phases of other compounds are present in the microstructure. These second phases may be particles dispersed in the matrix material, fibres or even porosity, and may be present intentionally or might be undesirable. There can be many reasons for adding a second phase to the matrix of a material. For example, in a thermal barrier coating the volume fraction of porosity is increased so as to lower the thermal conductivity of the coating and accommodate mismatch of thermal expansion. On the other hand, a second phase can be added to create a particular functionality to the material, like in the case of a self-healing thermal barrier coating. In any case, the addition of second phases, either solids or porosity, influences the elastic behaviour of the material. In this section models are presented to describe this influence.

The influence of porosity on the elastic modulus is especially important for ceramics because they have higher volume fractions of porosity than other materials. This is mainly due to the manufacturing process of ceramics based on sintering of powders. Hence, the degree of densification is a measure of the quality of ceramics.

A first approach for modelling the effect of porosity would be to consider pores as a second constituent in a particulate composite. However, the rules of mixture used for modelling the elastic modulus of particulate composites lose accuracy the higher the difference between the elastic modulus of particles and matrix. Therefore, models only focused on porosity have been developed. There are theoretical models and approaches based on experimental fitting. Some of the most frequently employed models are described here.

One of the first approaches was the one developed by Mackenzie (1950) which considers a low concentration of spherical pores (17). In this theoretical model the elastic modulus is given by

$$\frac{E}{E_0} = 1 - aP + bP^2 \tag{5}$$

E_0 is the elastic modulus of the fully dense material, P is porosity volume fraction and a and b are constants that depend on the shape of the pores are approximately 1.9 and 0.9, respectively (18). Spriggs (1961) developed a model applicable to a higher range of porosity volume fraction based on experimental fitting of an exponential law (19)

$$\frac{E}{E_0} = e^{-bP} \tag{6}$$

The parameter b in this equation is fitted experimentally. Another well-known theoretical approach for the elastic modulus is the one developed by Ramakrishnan and Arunachalam (1993). The main advantage of this approach is that it allows to estimate the elastic modulus of the porous solid by knowing only the porosity volume fraction and the elastic modulus and Poisson's ratio of fully dense material (20)

$$\frac{E}{E_0} = \frac{(1-P)^2}{1+(2-3\nu_0)P} \tag{7}$$

Another commonly used approach based on experimental fitting is the model of Phani et al. (1987), which is based on fitting a power law (21)

$$\frac{E}{E_0} = (1-fP)^n \tag{8}$$

In the previous equation f and n are experimentally fitted parameters. Several authors have reported that Phani's model provide the best fitting of both experimental and numerical data. Roberts et al. studied influence of porosity and pore shape on the elastic modulus of ceramics and they could conclude that Phani's model describes accurately the behaviour of their numerical results (22). Flinn et al. also used Phani's model for fitting their experimental data, although they included a slight change in the equation. Instead of using a fitting parameter f, they use $1/P_1$, being P_1 a volume fraction of porosity very close to the measured porosity volume fraction of the green body (23). The idea of normalizing the porosity with the porosity of the green body has been already proposed by other authors. In his book, *An Introduction to the Mechanical Properties of Ceramics*, D. J. Green explains that it is expected the measured Young's modulus of a powder compact to be close to zero when loading the solid in tension (18). Therefore, it makes sense to normalize the porosity volume fraction with the value for the green body. Green gives a simple linear relation $E/E_0=1-P/P_g$, in which the elastic modulus of the material is defined as a function of its degree of densification. P_g is the porosity volume fraction of the green body; hence the elastic modulus is equal to zero when approaching this value. The combination of Phani's model and the elastic modulus as a function of degree of densification given by Green results in a relation like:

$$\frac{E}{E_0} = \left(1-\frac{P}{P_g}\right)^n \tag{9}$$

which is similar to the relation used by Flinn et al. (23) for the study of the influence of porosity in the strength of alumina.

Regarding the effect of second phase particles on the elastic properties, as in the case of porosity, there are many models developed for predicting elastic properties of particulate composites. The most well-known models are well summarized in Green's work (18).

One of the most conservative rules of mixtures is the one proposed by Voigt and Reuss, based on stress/strain averaging techniques.

$$Voigt\ (Upper)\ bound{:}\ M = M_1V_1 + M_2V_2 \quad Reuss\ (Lower)\ bound{:}\ \frac{1}{M} = \frac{V_1}{M_1} + \frac{V_2}{M_2} \tag{10}$$

In these relations V_1 and V_2 are the volume fractions of the constituents, although it could be extended to more than two constituents. M can either be the bulk or shear modulus;

hence, for obtaining Young's modulus and Poisson's ratio the relations in Equation 2 can be used. The Voigt and Reuss (VR) bounds establish a range for the elastic modulus of the composite. In order to come up with a unique value several averaging techniques have been proposed and can be found in literature. The simplest procedure is the one proposed by Hill that consists on making the arithmetic average of the VR bounds.

A more accurate solution was proposed by Hashin and Shtrikman and is based on elasticity energy theorems. Unlike VR bounds, in the case of the Hashin-Shtrikman (HS) model the bounds for the bulk modulus are normally used:

$$\begin{gathered}\frac{K-K_1}{K_2-K_1}=V_2\left[1+\frac{V_1(M_2-M_1)}{M_1+H}\right]^{-1}, being \\ H=\frac{4G_1}{3}\ for\ bound\ 1\ and\ \frac{4G_2}{3}\ for\ bound\ 2\end{gathered} \tag{11}$$

HS bounds are always within the VR bounds so HS bounds are considered more accurate. As for the VR bounds, normally the arithmetic average of the HS bounds is done as a first approximation of the elastic modulus of the particulate composite.

2.1.3 Plastic behaviour of ceramics

Diffusion (creep), dislocations movement and microcracking are the sources of plastic deformation in solids. Plastic deformation is the irreversible nonlinear deformation of solids upon loading beyond the yield stress σ_y. Ceramics exhibit low or no plastic deformation at all prior to fracture. As in the case of the elastic modulus, this behavior is directly related to the atomic structure of ceramics. The mixed ionic/covalent nature of the bond in ceramics is characterized by electrons strongly bonded close to the ion cores, so their movement is hindered. Metals exhibit the opposite situation. Their valence electrons are very mobile and that is one of the reasons for the easy dislocation movement.

Because ceramic materials are characterized by a very high yield stress and normally brittle fracture occurs before yielding of the material, assuming linear elastic behavior of ceramics is a reasonable assumption for structural modeling. Plastic deformation in ceramics can be observed sometimes under compressive loads. The most typical case is indentation test for hardness determination. Hardness measures the resistance of the material to plastic deformation in the surface, so there is a direct relation between hardness and yield stress of the material. As common rule of thumb it holds that $H=3\sigma_y$ (16). When indenting the surface of a ceramic the material is irreversibly deformed. However, normally this plastic deformation under compressive load in ceramics is not related to a dislocation movement, but to microcracking caused by the formation of glide bands and pile-up of dislocations at the grain boundaries (24). This is the source of indentation cracks in hardness testing of ceramics for high loads.

2.1.4 Thermal behaviour of ceramics

Thermal properties are the most important design variables for ceramics because they are normally used for high temperature applications. The first thermal property of interest is the thermal expansion coefficient, which is a tensor property. It describes the deformation of a solid exposed to a certain temperature gradient.

$$\varepsilon_{ij}=\alpha_{ij}\Delta T \tag{12}$$

ε_{ij} is the deformation induced by the temperature gradient and α_{ij} is the tensor of coefficients of thermal expansion. The thermal expansion coefficient is also related to the shape of the potential well that defines the bonding energy between two atoms of the crystal lattice, as for the elastic modulus; hence this coefficient depends also on the crystallographic direction. For polycrystalline solids with no texture (isotropic properties) the macroscopic thermal expansion coefficient can be defined by a unique value called coefficient of linear thermal expansion (CTE).

The CTE is the main design variable when it comes to estimate thermal stresses of a constraint body exposed to a temperature gradient. Ceramics have in general a low CTE because of the high stiffness of the atomic bonds, however the high elastic modulus leads to high thermal stresses which are normally the main damage mechanism of ceramics. A simple model for the thermal stresses in a constraint thermally strained solid is presented in (25):

$$\sigma_{thermal} = CTE(T, T_0)E'\mathrm{n}\Delta T \qquad (13)$$

In the previous equation n is a parameter that varies between 0 and 1, and it represents the constraints in the component. E' is related to the elastic properties of the material and it depends on how the body is loaded. For example, for a state of plane stress $E' = E/(1-\nu)$.

The other important thermal properties of ceramics are thermal diffusivity and thermal conductivity. Thermal diffusivity is a measure of the velocity with which heat is transferred through the material; while thermal conductivity measures the same phenomena but in terms of energy. Both properties can be related with this expression

$$\lambda = a\rho C_p \qquad (14)$$

λ is the thermal conductivity, a is thermal diffusivity, ρ is density of the material and C_p is the heat capacity of the material. Unlike the CTE, thermal conductivity and diffusivity are microstructure dependent and they are based on the movement of phonons through the material. By changing the microstructure, the mean free path of phonons changes.

2.1.5 Fracture behaviour of ceramics

Fracture behavior of solids is described by the strength and fracture toughness. Fracture toughness (K_{IC}) can be defined as the critical stress intensity factor in the crack tip for which brittle fracture occurs (unstable crack propagation). The stress intensity factor can be defined as an "intensification" of the far field stress near the crack tip. Toughness can be defined also in energy terms, as proposed by Griffith (26). The equivalent definition is the critical energy release rate. The critical energy release rate is the value for which the energy released when creating new crack surface is higher than the energy consumed for crack opening. One of the main issues with Griffith's criterion is that he assumed that the only energy dissipation mechanism in the crack tip is the creation of new crack surface. However, this is only true for very brittle solids. G. R. Irwin and E. Orowan, working independently, arrived to the same conclusion that Griffith's criterion could be modified so as to take into account the effect of plastic deformation and toughening mechanisms in the material (27) (28). They defined a new material parameter called critical strain energy release rate, $G_{c,}$ also called toughness of the material. This is a value that defines the moment in which the strain energy is released at a sufficient rate so as to be equal to all the energy dissipation mechanisms in the crack tip.

Strength is the most important design variable in ceramics and it is of statistical nature (29). The tensile strength is limited, in principle, by the necessary stress to break the bond between two atoms. However, due to flaws present in the material the macroscopic strength is much lower because of the stress concentration created by these imperfections in the solid. In order to make more clear the idea that strength determination is statistical by nature let’s look at the Griffith’s flaw-size/strength relation

$$\sigma_f = \frac{K_C}{Y\sqrt{\pi a_c}} \tag{15}$$

Kc is fracture toughness, Y is a geometry constant and a_c is the average size of the critical flaws.

According to this equation the larger the flaw size the lower the strength of the material or, being more precise, it is lower the maximum stress that the material can bear before it fails. The flaws size will depend on the component that is being tested so this is clearly of statistical nature. The way to deal with this issue is to use Weibull statistical analysis.

2.2. Mechanical characterization

In this section the methods used for extracting mechanical properties from the different tests are presented.

2.2.1 Characterization of elastic modulus by depth-sensing indentation

Indentation is the traditional technique for measuring hardness of a material. It is a simple test in which a tip of a very hard material (normally diamond) penetrates in the surface of a material by applying a certain controlled load. Nowadays indentation tests are used for characterization of a much wider range of mechanical properties thanks to the development of instrumented indentation, also known as depth-sensing indentation, in the last two decades. This technique was created by Warren Oliver and John Pethica in 1983 and started commercializing indentation systems with which the force-depth displacement could be measured for the entire time the indenter is in contact with the material (30). They developed this technique motivated by the research of Doerner and Nix, who showed that there could be a relation between the elastic modulus of the material and the spring-back when removing the indenter after indentation (31). Besides the potential of the technique for determining the elastic modulus of a material, Oliver together with George Pharr developed a method for determining the size of the indent from the results of depth-sensing indentation technique. The method became rapidly popular because of its potential to determine hardness without need of optical observation and measurement of indent diagonals.

The determination of the elastic modulus by means of depth-sensing indentation is done by application of this expression (32)

$$\frac{1}{E_{ff}} = \frac{2\sqrt{A_c}}{S\sqrt{\pi}} = \frac{1-\nu^2}{E} + \frac{1-\nu_i^2}{E_i} \tag{16}$$

In this equation E_i and ν_i are the elastic modulus and Poisson´s ratio of the indenter material, respectively. E and ν are the elastic modulus and Poisson’s ratio of the material under study. In order to determine the elastic modulus, it is necessary to give an estimation of the Poisson’s ratio. E_{ff} is the effective elastic modulus calculated from the measurements of the depth-sensing indentation, but without taking into account the influence of the elasticity of the indenter tip. A_c is the contact area between the indenter and the material. S is the stiffness of the contact between the material and the indenter. A_c and S are two parameters that can be calculated from the results of the depth-sensing indentation test.

The area of contact A_c is a function of the contact depth h_c, which is not equal to the maximum penetration measured by the equipment. The maximum penetration is equal to the contact depth and the depth due to elastic deformation, also called sink-in depth. Figure 1 illustrates the difference between the ideal case (left) in which only plastic deformation is produced during the contact and the real case (right) in which elastic and plastic deformation is produced during loading.

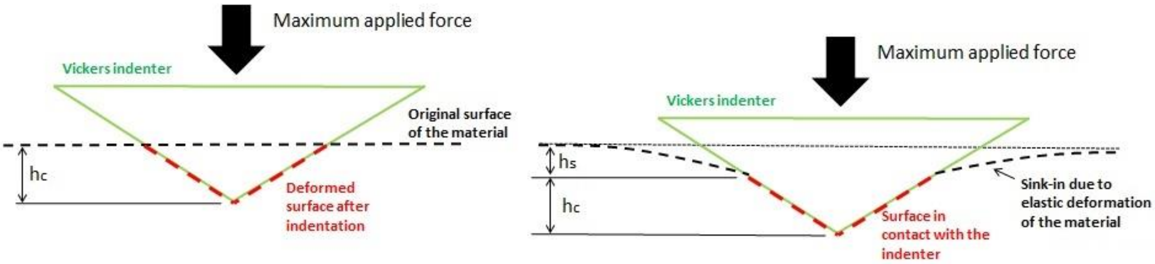

Figure 1 - Cross-section of the indentation site. Ideal (left) and real (right) case.

Therefore, the contact depth h_c can be calculated as the difference of maximum penetration and sink-in depth. The sink-in depth is a parameter that cannot be extracted directly from the test, so a model is needed for calculating the value (32)

$$h_c = h_{max} - h_s = h_{max} - \varepsilon \frac{P_{max}}{S} \tag{17}$$

In this equation ε is a parameter that depends on the indenter shape, and is taken equal to 0.72 in the case of a Vickers indenter (33). P_{max} is the maximum applied load and S is the contact stiffness of the depth-sensing indentation.

As mentioned before, the contact area is a function of the contact depth h_c. Oliver and Pharr proposed the following expression for calculating the contact area between indenter and material (32)

$$A_c = \sum_{0}^{8} C_n (h_c)^{2^{1-n}} = C_0 h_c^2 + C_1 h_c + C_2 h_c^{1/2} + \cdots + C_8 h_c^{1/128} \tag{18}$$

There are 8 constants that need to be determined before performing an indentation test on the material under study. Normally a material of known properties is used for calibration. In practice, the equation is truncated to the first two terms. C_0 represents the area of a perfect diamond indenter with no defects. C_1 is related to tip imperfections and its influence becomes more important the smaller the indentation depth. The function can be even more simplified for deep penetrations ($h_c > 6$µm) and in the case of Vickers indenter the function would be $A_c = 24.5 h_c^2$ (34).

In the calculation of the contact depth, h_c, it has been assumed that all the material surrounding the indent tip sinks and that the sink-in depth can be described by a linear elastic law. However, in many elastic-plastic materials it has been observed that there is pile-up of the material around the contact of the indenter tip. This pile-up of material around the tip leads to an overestimation of the contact area and, therefore, the elastic modulus and hardness are also overestimated, sometimes by a factor of 50% (35). Bolshakov and Pharr examined the conditions for which pile-up occurs by means of finite element simulations. They arrived to two interesting conclusions. First, the main factor that determines the existence of pile-up is the ratio of E_{ff}/σ_y. A large ratio E_{ff}/σ_y leads to more pile-up. The second conclusion is that the work-hardening behavior influences the pile-up. They showed that if the surface has been previously work hardened the pile-up will be reduced. This second conclusion is in line with the results of D. J. Shuman et al. who selected several materials and performed unloading-reloading instrumented indentation test (33). The first conclusion they made was that only the elastic modulus obtained for fused silica by using the unloading curve for the calculation of the contact stiffness was in agreement with literature. The values for steel, nickel, aluminum and copper were overestimated. However, when they calculated the modulus from the contact stiffness of the second unloading curve (after reloading) they realized that the value was much closer to that reported in literature. This means that during the first loading the material was work-hardened and then during reloading only elastic deformation occurred.

The second parameter that can be extracted from the results of depth-sensing indentation is the stiffness of the contact between indenter tip and material. In the original method developed by Oliver and Pharr this parameter is extracted from the unloading curve. It was observed experimentally that the unloading curve generally fits to a power law. The first part of the unloading curve is linear and related to the elastic modulus of the indented material. The following equation is proposed for the unloading curve (32):

$$P = \alpha(h - h_f)^m \qquad (19)$$

, where α and m are the values that must be fitted experimentally. h_f is the final permanent depth before the load is totally removed. The contact stiffness can be calculated from the slope of the initial stage of unloading (dP/dh).

The improvement and development of instrumented indentation equipment has led to a new method which offers a great potential, the Continuous Stiffness Measurement Technique (CSM). This technique is based on applying a dynamic oscillation coupled with the loading force of the indenter. The amplitude of the oscillation is several orders of magnitude smaller than the applied load for indentation and by applying a frequency-specific amplifier it is possible to analyze the response and calculate the contact stiffness distribution along the loading stage of the indentation (36) (37).

Previous to indentation, it is necessary to know the dynamic response of the indentation system, which is defined by the mass of the indenter m, the spring constant K_s of the springs that support the indenter and the stiffness K_f and damping coefficient D of the indenter frame (load and sensing system).

Assuming that the superimposed oscillatory load is:

$$P = P_d e^{i\omega t}, \qquad (20)$$

the displacement response sensed by the system is of this form:

$$h(\omega) = h_0 e^{(i\omega t + \phi)} \qquad (21)$$

being ω the set frequency and ϕ is the phase difference between the force and displacement signals. P_d is the magnitude of the imposed force oscillation coupled with the indentation load. By solving the in-phase and out-of-phase portions of the response it is possible to calculate the contact stiffness, which is given by (36):

$$S = \left[\frac{1}{\left(\frac{P_d}{h(\omega)} \cos \phi \right) - (K_s - m\omega^2)} - \frac{1}{K_f} \right]^{-1} \tag{22}$$

Using this equation for calculating the contact stiffness at each penetration displacement interval and using the model explained in this section, the evolution of elastic modulus along the whole depth range can be determined.

2.2.2 Characterization of hardness by Instrumented and Vickers Indentation

The determination of hardness of a material has been traditionally done by indentation and optical observation of the indents. There are several standard techniques for measurement of hardness in a material, but the focus in this thesis is on Vickers hardness and instrumented hardness.

Vickers hardness measurement is a conventional method that consists on introducing a pyramidal indenter made of diamond in the surface of a material by using a controlled load. After removal of the load the indent diagonals are measured. Then the Vickers hardness is calculated from (38):

$$HV = 0.0018544 \left(\frac{P}{d^2} \right) \ [GPa] \tag{23}$$

, where P is the applied load and d is the average of the two indent diagonals. Although the test is simple, it is important to follow the protocol stablished in the related standard (38) in order to have a trustful result.

Determination of hardness by instrumented indentation has been developed more recently and a depth-sensing system is necessary for carrying out this test. Hardness can be determined by the simple relation

$$H = \frac{P}{A_c} \tag{24}$$

A_c is the area of contact and it is calculated using equation 18. The main advantage of this method is that it does not require optical observation of the indent; thus reducing the test time and avoiding errors measuring indent diagonals.

2.2.3 Indentation Fracture Toughness

Indentation Fracture Toughness (IFT) is a method for estimating the fracture toughness of a brittle material from indentation test. Many different models can be found in literature, all semi-empirical or fully experimental approaches. It is not a standardized technique; in fact, standardization authorities do not recommend the use of this method because of several reasons (39). First, models for calculating fracture toughness from indentation are all based on experimental observation rather than having a solid analytical background. Also the definition of fracture toughness does not match with the physics of what happens during indentation fracture. When indenting a brittle material, a crack starts propagating from the indent tips but it is arrested at some point. The fact that many experimental factors influence the results (like the optical measurement of crack length) is another reason for this method not to be a standard. Even so, its simplicity and low cost makes it attractive for research purposes and many cases are found in literature of indentation fracture toughness used as characterization technique. The work of Y. Feng et al. is a good review of the state-of-art of different methods for calculation of Indentation Fracture Toughness (40). In this review it is highlighted that crack pattern and indenter geometry are the most important parameters that define the difference between the available models in literature. In this research project only Vickers Indentation Fracture Toughness will be studied. The models for Vickers indentation fracture toughness can be divided into two groups, each one for a different crack type. In Figure 2 the two types of crack pattern are shown.

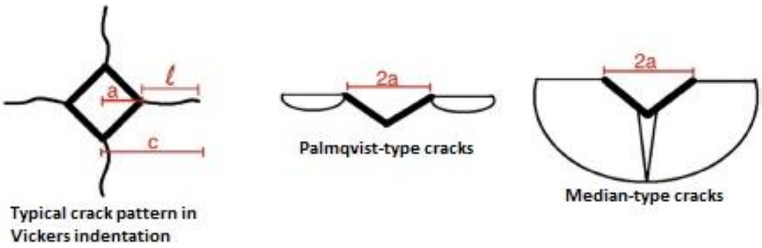

Figure 2 - Typical crack patterns in a Vickers indentation. Figure in the left shows the crack from the top and figures in the right show the cross-section. Adapted from (41).

Median-type cracks are the most common in indentation fracture of brittle materials. In this case the cracks are deeper than the indent and they follow the direction of the indent diagonals. Palmqvist-type cracks are less common, although it has been observed that it is the first type of crack that forms during indentation and then during unloading the crack evolves to median crack (42). However, there are some cases in which Palmqvist cracks are observed even after unloading and, actually, this behavior has been observed for the YSZ (43) (44) (45). The presence of Palmqvst cracks even after unloading is normally associated to tough ceramics (46). They are normally characterized by a low crack-to-indent diagonal (c/a) ratio, below 2.5. The initial model of Evans and Charles based on dimensional analysis (47) was adapted by Niihara et al. for including materials exhibiting Palmqvist cracks, with low crack-to-indent diagonal ratios (46).

An important issue for selecting the right model for indentation fracture toughness is the determination of the real crack pattern after an indentation. Gradual grinding and polishing of the surface is the only way to determine the crack geometry, although this is a destructive method.

Although literature suggests that indentation cracks in YSZ are Palmqvis-type, in this study models for Median cracks will be also considered for comparison. One of the most frequently used models for Median cracks is that of Anstis (48)

$$K_{IC} = 0.016\left(\frac{E}{H}\right)^{0.5}\left(\frac{P}{c^{1.5}}\right) \tag{25}$$

In the case of Palmqvist-type cracks the most frequently used model is that of Niihara (46)

$$K_{IC} = 0.035\left(\frac{c}{a} - 1\right)^{-0.5}\left(\frac{H}{3E}\right)^{-0.4}\left(\frac{Ha^{0.5}}{3}\right) \tag{26}$$

2.2.4 Strength and fracture toughness determination from the Brazilian Disc test

The Brazilian Disc test was created by Carneiro and Barcellos in 1953 and it was first developed for testing of concrete (49). Its simplicity and low cost quickly made it popular and it was extended to other types of materials like rocks and engineering ceramics. It is especially interesting for testing of ceramics because the compressive load reduces the probability of failure at the load introduction points, while the material is being loaded with a tensile stress in the centre of the specimen. Also, the ability for crack arrest due to the high compressive stresses in the load introduction area makes it attractive for testing of brittle self-healing materials. The addition of a diametral groove and a central hole for tensile stress intensification, and the two crack arrest holes in the sides, makes it even more attractive for testing self-healing brittle materials.

Carneiro and Barcellos based the analysis of their test set-up in the Hertzian solution for the stress distribution of elastic discs under diametrically opposite point compression loading (50). The stress distribution along the vertical diameter between the two load introduction points is given by:

$$\sigma_x = \frac{P}{\pi R t} \qquad \sigma_y = -\frac{P}{\pi R t}\frac{3R^2 + y^2}{R^2 - y^2} \tag{27}$$

, where R and t are the radius and thickness of the Brazilian disc, respectively. P is the value of the diametrical opposite point loads. y is the position along the vertical diameter; see Figure 3. Apart from assuming linear elastic and isotropic material, it has been assumed that the load in applied through a unique point of contact (Figure 3-a). Theoretically this is possible, but putting this into practice is very risky because it creates a very high stress concentration in the contact between punch and specimen. This may lead to failure of the specimen in the load introduction point. Therefore, it is suggested to increase the area of contact by using load introduction flat plates or curves surfaces. Hence, the next step was to generate a model for an elastic, isotropic disc with diametrically applied pressure along a central loading angle 2α. The main assumption taken for the development of the new formulation is that the distribution of pressure in the contact between the loading plate and the material is uniform (Figure 3-b).

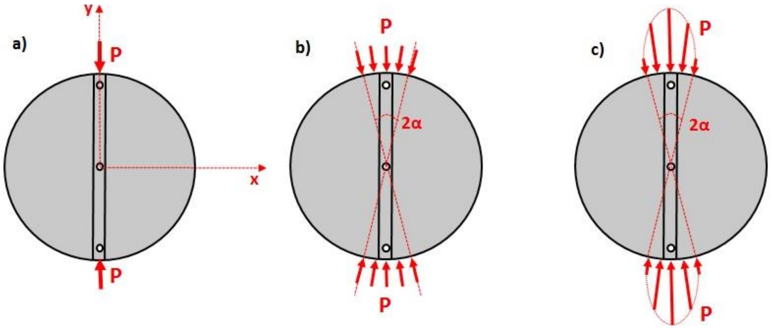

Figure 3 - Different loading configurations according to the different models proposed in literature

The stress distribution along the vertical diameter of the Brazilian disc for a uniform diametrically applied pressure along the central angle 2α was derived by Hondros in 1959 (51):

$$\sigma_x = C_1\left(\frac{P}{\pi R t}\right) \qquad \sigma_y = C_2\left(-\frac{P}{\pi R t}\right) \tag{28}$$

$C_1 = C_1(y)$ and $C_2 = C_2(y)$ are concentration factors and the complete expression can be found in Appendix 2.1. Basically, Hondros' model presents a similar formulation than Hertz's solution, but adding two factors that introduce the influence of the radially applied pressure. It can be easily proven that for $\alpha \rightarrow 0$, C_1 and C_2 tend to one so Hondros' model tends to Hertz's solution. Although Hondros' model provides a good approximation of the stress field in the centre of the specimen, which is the place where tensile failure is expected, the assumption of uniformly distributed radial pressure might lead to errors in some test situations, for example when the loading plates have a curvature. In this case, more advanced models have been developed for predicting the stress distribution in the Brazilian Disc. L. Japaridze has proposed a model that considers the Brazilian disc as a contact problem (52). Then, the normal load in the contact between punch and specimen has an elliptical shape (Figure 3-c). Additionally, the influence of the contact width a, the radius of the punch surface and the elastic properties of punch and specimen are taken into account. The expression for a is:

$$a = \sqrt{\frac{4PR}{\pi t\left(1+\frac{R}{R_{punch}}\right)}\left(\frac{1}{E_1}+\frac{1}{E_2}\right)} \tag{29}$$

As in the case of Hondros' model the distribution of stresses is given by two expressions similar to Hertz's solution and including two concentration factors that are presented in Appendix 2.1.

$$\sigma_x = C_3\left(\frac{P}{\pi R t}\right) \qquad \sigma_y = C_4\left(\frac{P}{\pi R t}\right) \tag{30}$$

$C_3 = C_3$ (y, a) and $C_4 = C_4$ (y, a) are the concentration factors and they vary during loading because they are function of the contact width which is a function of the load.

In the previously presented models the stress distribution is given along the vertical diameter (x=0, -R<y<R) according to the reference system in Figure 3.

In order to complete the formulation for extracting strength from the Brazilian Disc specimen it is necessary to obtain approximations of the stress concentration factors due to the effect of the groove and the central hole. The maximum tensile stress in the two points of the central hole in line with the vertical diameter (x=0, -R<y<R) accounting for the stress concentration factor equals:

$$\sigma_{max} = K_{hole}K_{groove}\sigma_{nom} \tag{31}$$

In the previous equation σ_{nom} is the maximum stress in the center of the disc without groove and hole. K_{hole} and K_{groove} are the stress concentration factors. The values for the stress concentration factors as a function of the specimen geometry can be found in Appendix 2.2. The factors have been taken from *Peterson's stress concentration* factors book (53) and from Schijve (54).

For calculation of fracture toughness, a FE model using Cohesive Zone Modelling approach will be used and the fracture toughness will be fitted from the results of BD test and WL-DCB test.

2.2.5 Strength and fracture toughness determination from the Wedge-Loaded Double Cantilever Beam test

The wedge-loaded double cantilever beam (WL-DCB) test is a potential method for mechanical characterization of brittle self-healing materials because of the inherent ability of double cantilever beam specimens for stable and slow crack growth, and it avoids the need for load introduction holes and clamps. High stress concentrations in the load introduction elements is a common reason for premature failure of a ceramic test specimen. The addition of geometrical features like chevron notches, guidance grooves or crack arrest holes further increases its potential as test method for brittle self-healing materials. The usefulness of chevron notches in WL-DCB specimens has been already proven by other authors, although not for testing self-healing materials. Odette et al. used it for achieving repeatable crack initiation and arrest in metallic materials (55). Due to the shape of the chevron notch, the stress intensity factor will rapidly decrease as the crack goes deeper into the specimen. Many examples of the use of crack guidance grooves can be found. White et al. introduced a groove in a tapered DCB specimen for ensuring a controlled crack growth along the centreline of the specimen (56). Good examples of the addition of a crack arrest hole for quantification of self-healing efficiency are the studies of Rahmathullah and Palmese (57) and Chen et al. (58).

Despite its potential for quantification of healing of self-healing brittle materials, the WL-DCB set-up does not have an extensive analytical formulation for extraction of mechanical properties, unlike the BD set-up. This is mainly due to the uncertainties for modelling frictional effects between the wedge and the sample (59). Even so, some authors have used this test method for extraction of mechanical properties by using formulation based on experimental fitting and finite elements modelling (60) (61). However, this formulation is not general and cannot be used for the set-up used in this project.

Therefore, for the extraction of strength and fracture toughness from the WL-DCB test a FE model using Cohesive Zone Modelling approach will be used. Strength and fracture toughness will be obtained by fitting the experimental results with the simulation.

3 Experimental procedure

3.1. Materials

Two different powders have been used to prepare the matrix of the self-healing composites. It is the same material, yttria-stabilized zirconia (YSZ), but with different characteristics and from different manufacturers. One of the powders is commercial yttria-partially stabilized zirconia with 3 mol% yttria. Manufacturer's designation is TZ-3Y-E and it is made by Tosoh Corporation (Japan). It has a purity of 99.9 wt%, specific surface area of 16 m^2/g and an actual particle size of 40 nm (around 200-400 nm after sintering). The theoretical density of this material equals sintered body in 6.05 g/cm^3. The other type of powder is commercial yttria-stabilized zirconia with approximately 4-5 mol% yttria (7-8 wt% yttria as reported by the manufacturer). Manufacturer's designation is Amperit 827 and it is made by H.C. Stark (Germany). Average particle size (D50) is around 50 µm. It is a powder designed for thermal spraying. Powders for plasma sprayed thermal barrier coatings are normally big in size (for enhancing the creation of a porous coating) and contain normally a 5 mol% yttria (See Section 4.1.1).

For the purpose of this project, the development of a proof of concept for the self-healing capability, many difficulties were found when processing Amperit powders. Therefore, it was decided to use 3 mol% YSZ nano-size powder from Tosoh for the proof of concept.

Regarding the material for the healing particles, several types of MSBA ($MoSi_2$ powders with additions of Al and B in substitution of Si) have been used, all from the same manufacturer (ChemPur, Germany). These are not commercial powder, especially prepared for this project. Two types of powders were prepared: (i) $MoSi_2$ with addition of 2 wt% B and 6 wt% Al and (ii) $MoSi_2$ with addition of a 2 wt% B and 12 wt% Al. Information related to the particle size distribution of the as received state can be found in Table 1.

With these materials different types of composites have been prepared varying the healing particle composition: YSZ + 10 vol% healing particles made of $MoSi_2$ with addition of 2 wt% B and 6 wt% Al in substitution of Si, YSZ + 10 vol% healing particles made of $MoSi_2$ with addition of 2 wt% B and 12 wt% Al in substitution of Si and YSZ + 10 vol% healing particles made of $MoSi_2$ with addition of 2 wt% B and 6 wt% Al in substitution of Si and encapsulated with a thin Al_2O_3 shell via sol-gel prior to mixing and sintering. For the YSZ matrix either Amperit or Tosoh powders are used. It will be specified in each case. The denomination for the composites is YSZ-10MSB6A, YSZ-10MSB12A and YSZ-10MSB6Asol-gel, respectively.

3.2. Manufacturing procedure of specimens

3.2.1 Powder preparation

There are several procedures that need to be done on the raw powders before sintering of specimens. Different powder processing techniques have been done: wet mixing of powders for composites manufacturing, downsizing of coarse powders, sol-gel encapsulation of MSBA particles, wind sifting of the raw MSBA powder and measurement of particle size distribution.

Measurement of particle size distribution was used for quantifying the improvement of particle size distribution of the raw MSBA powder after wind sifting. Also for measuring particle size of raw Tosoh-YSZ and Amperit-YSZ powders after downsizing. A Mastersizer S XG of Malvern (UK) was used.

Wind sifting of the raw MSBA powder is carried out to eliminate small particles and impurities and increase the relative amount of particles with the desired size (~ 30 µm). Wind sifting was performed using an Alpine 100 MRZ laboratory zig-zag classifier. The selected airflow was 15 m^3/h and the classifier rotational speed was set to 5000 rpm. Three cycles were applied for ensuring a homogeneous size distribution. Table 1 shows the improvements of the particle size distribution:

Material	Before wind sifting			After wind sifting		
	D10 [µm]	D50 [µm]	D90 [µm]	D10 [µm]	D50 [µm]	D90 [µm]
MSBA (2 wt% B, 6 wt% Al)	1.6	14.7	47.1	15.6	32.6	57.9
MSBA (2 wt% B, 12 wt% Al)	2.9	18.2	49.7	16.8	32.9	58.6

Table 1 - Results of particle size distribution before and after wind sifting

Downsizing of the coarse YSZ Amperit powder was done with a planetary ball-milling machine PM100 of Retsch (Germany). Dry raw Amperit powders were placed in a zirconia jar, together with 10 mm zirconia balls with a ratio of 3:1 (1 ball for each 3 g of powder). The crucible is hermetically closed and mounted in the machine. The milling is set at 300 rpm during 12 h. Downsizing is done because the as received powder has a big average particle size. However, for sintering in SPS a dense material, it is necessary to have a finer grain. Table 2 shows the change of grain size in Amperit powders before and after downsizing.

Material	Before downsizing			After downsizing		
	D10 [µm]	D50 [µm]	D90 [µm]	D10 [µm]	D50 [µm]	D90 [µm]
YSZ - Amperit	27.4	50.1	80.5	2.4	7.9	15.1

Table 2 - Results of particle size distribution before and after downsizing

Sol-gel encapsulation of healing particles was done prior to manufacturing of some of the composites. Other composites were manufactured without pre-encapsulation of particles. The sol-gel encapsulation is a two steps process in which the MSBA particles are first coated with a boehmite (AlOOH) layer and then calcinated for creating the final Al_2O_3 shell. More details about this process can be found in (62).

Wet mixing was selected for preparation of the powder of the composite specimens. This technique was chosen because the powders for the matrix material (YSZ) and the healing particles (MSBA) are several orders of magnitude different in size (around 100 nm for the YSZ powder and 20-30 µm for the healing particles) and substantially different in weight. Dry mixing could lead to a segregation in the mix of a MSBA-rich area. Wet mixing process starts with weighting the powders, using a balance PM4800 DeltaRange of Mettler Toledo (US), and mixing them in a clean bottle. The weight ratio is selected according to the desired final volume fraction of particles in the composite. Next step is addition of 10 mm zirconia balls for improving the mixing process, 1 ball per 6 g of mix approximately. The bottle is filled with isopropanol up to 2/3 of the volume, then closed and shaken. The cover is sealed with paraffin tape and then introduced in a standard bottle for a Turbula mixer T2C mixer from Willy A. Bachofen (Switzerland). The mixture was kept in the Turbula mixer around 12 hours and then poured in a recipient and dried at 100 ºC for another 12 hours in a conventional oven. Once the mixture is dried, it is passed through a standard 200 µm sieve (ISO 3310-1). When the mixture was already in powder form it was kept in the oven at 100 ºC until sintering process for preventing humidity ingestion.

3.2.2 Spark plasma sintering process

All the specimens in this project have been manufactured with Spark Plasma Sintering (SPS) using a HP D 25 furnace of FCT Systeme GmbH (Germany).

Spark plasma sintering is a relatively new technique that is becoming popular in the field of powder metallurgy and ceramics processing because of the lower sintering temperatures and shorter processing times as compared with conventional sintering techniques. The fast consolidation leads to a low power consumption. Hence, it is an energy saving process, as compared with the conventional sintering techniques (63). In addition to the more competitive processing conditions, it has been proven the superior results of the specimens manufactured by SPS. With this technique, materials with densities close to the theoretical value can be achieved and it minimizes grain growth due to the short sintering time (64).

Most of the work carried out with the spark plasma sintering technique still remains within the materials research and development field. Industrialization of the SPS process is still a challenge and it depends mainly on the availability of suitable equipment that can produce components with optimum cost efficiency (65). Despite many years of research with SPS there is not a complete understanding yet about the mechanism for the high-speed consolidation (63).

The spark plasma sintering technique consists on passing a DC pulsed high electric current with a low voltage through an electrical conducting pressing die (normally graphite) in which the material in powder form is confined. The material is pressed at the same time that the DC pulsed current is applied. In the early stage of the sintering process the applied pulse DC current results in spark discharges that appear in the gaps or in the contact between particles of the material. By Joule heating a very high temperature is reached locally in the points of spark discharge. This local heating causes melting and even evaporation of the surface of the powder and this leads to formation of "necks" or bridges of material around the area of contact between two particles. Another phenomenon that occurs due to the spark discharge is sputtering. This results in the elimination of surface impurities in the powder due to the spark impact pressure generated by the spark plasma. High-speed diffusion and migration of ions are enhanced due to this phenomenon.

In this project the same protocol has been used for all the specimens manufactured by SPS. First, a set of two pressing punches and a hollow die, all made of graphite, are selected depending of the final diameter of the disc. Samples with 20, 30 and 40 mm have been produced. Next, two layers of thin graphite paper are placed in the inner hole of the die and four circle-shape graphite papers are prepared for the contact between the powder and the punches. One of the punches is introduced in such a way that the double graphite paper remains in between the inner wall of the die and the punch. Then two of the graphite papers are placed in the surface of the punch. The powder of the material is weighted and introduced inside the die. The powder is pre-pressed using the second punch. The punch is removed and the two layers of graphite paper are placed. Then, the second punch is placed and the mould is ready for the process. The graphite papers need to be used in order to protect the punches and die from the reaction with the material. Additionally, in order to facilitate demoulding after the process, a fine layer of BN (HeBoCoat 21E, Henze, Germany) is sprayed in the surface of the graphite paper that is in contact with the die and the material. Once the mould is ready, it is placed inside the furnace vessel and the upper piston is closed until the column is pressed with 4-5 kN. Before closing the vessel, a graphite blanket is placed around the graphite die and punches in order to prevent damage of the vessel because of the glowing light of the high temperature sintering. The vessel is closed and the desired process parameters are introduced in the control software. In all the cases, after the holding time at maximum temperature the pistons are released for allowing a “natural cooling”.

Different SPS recipes have been used depending on the size of the specimen. For the 20mm discs sintering is done at 1200 ºC during a holding time of 1 hour, heating rate of 20 ºC/min, natural cooling, a pressure of 50 MPa and vacuum inside the vessel. For the 30 and 40mm specimens the only parameters that change are temperature and holding time. For these specimens a sintering temperature of 1500 ºC and 30 minutes holding time were used. During heating a plateau at 600 ºC during 10 minutes was included for homogenizing the temperature in the disc. All the recipes and manufacturing details of each of the samples can be found in Appendix 3.1.

3.3. Heat treatments

3.3.1 Annealing for in-situ encapsulation

The $MoSi_2$ healing particles used for the YSZ composites contain Al in solid solution for creating the protective alumina shell (See Section 1.1). During the SPS process (in vacuum atmosphere) part of the aluminium in the particles is depleted and a thin alumina shell is formed surrounding the particles. However, the SPS process is not enough for depleting the whole aluminium reservoir. This is the reason why an annealing treatment is needed.

An annealing treatment was applied to all the specimens prepared for crack healing experiments and the BD and WL-DCB samples for mechanical proof of healing. Even the composites prepared with pre-encapsulated particles via sol-gel process need an annealing treatment because the alumina shell created by sol-gel encapsulation has been proven to be not thick enough so as to prevent oxygen diffusion to the particles.

Two different protocols were applied because of the two different furnaces. Both furnaces are from Carbolite-Gero (UK) and the chambers are prepared for performing annealing in controlled atmosphere. One has a 30 mm quartz tube and it has the option of taking in and out the sample without removing the controlled atmosphere, however the bigger furnace (with an alumina tube) does not have this option. This is the reason for the different annealing protocol.

Samples for crack healing experiments have been annealed during 16 hours at 1100 ºC in Argon. The samples are introduced and removed at 1100 ºC. For the BD and WL-DCB specimens the bigger furnace has been used because the samples are bigger than the quartz tube of the other furnace. For this samples also an annealing for 16 hours at 1100 ºC in Argon has been applied, but the samples also experienced the heating and cooling cycles of the furnace because they need to be introduced in the hot area before the chamber is sealed to the controlled atmosphere.

3.3.2 Healing treatments

Healing treatments were performed in a tube furnace TZF 17/600 of Carbolite (UK) with alumina tube and 600mm of heated length (3-zone model). All the treatments were performed in air (open furnace) at 1100 ºC. In order to study the influence of healing time in the microstructure different healing times were applied (1h, 4h and 16h).

3.4. Sample preparation

3.4.1 Surface preparation

A flat and smooth surface is required for microstructure characterization by optical microscopy, scanning electron microscopy, and indentation.

The first step in surface preparation is to eliminate the graphite layer from the SPS specimens. Very coarse-grain abrasive paper is used, CarbiMet SiC abrasive paper of grades P80 and P120. In case the coarse SiC paper is not enough for eliminating the graphite in the surface of the specimen, a grinding diamond pad of coarse grain is used. For this grinding process a MetaServ 250 of Buehler is used.

Next step is grinding/polishing gradually decreasing the grade of the abrasive paper. The process starts with CarbiMet SiC abrasive paper of grades P240 and it is gradually decreased until P4000. The procedure is simple. It needs to be ensured that for each disc the scratches due to grinding go all in the same direction. When changing to a lower grade the grinding lines must be done perpendicular to the previous ones. In this way, the coarse scratches are eliminated until getting a very fine surface finish.

The last step is the use of polishing clothes and diamond paste of different grades. A Ecomet IV of Buehler is used. The surface is polished gradually changing the diamond paste from 3 to 0.25 µm grains. Before and after each process the surface of the material is cleaned in ethanol with an ultrasonic cleaner Branson 2510.

3.4.2 Cross-section preparation

For preparing cross-sections of the material and also cutting SPS discs in different pieces a low speed saw IsoMet of Buehler was used. The obtained surface from cutting is very rough so it needs to be ground and polished according to the process described in Section 3.4.1.

3.4.3 Machining of WL-DCB and BD specimens

Machining of the WL-DCB and BD samples from the sintered SPS discs was done in an external partner, Ceratec Technical Ceramics BV (the Netherlands). Diamond tooling was used in all the cases and different equipment was used for achieving the geometry specified in the drawings (See Appendix 3.2): circular grinding, plane grinding and 4-axis computer numeric control (CNC) machining.

After machining, the surface of all the specimens is analysed with SEM in as-received condition for identifying the type and size of damage introduced in the surface during removal of material (See Section 4.3.1). The observation of the surface condition of the specimens is very important for the mechanical characterization of the material since ceramics are very sensible to machining defects. During machining several types of defects are created in the surface: chipping (or roughness created by the removal of material from a lateral crack), residual stress and microcracks (normally parallel or perpendicular to the grinding direction). The existence of these defects is attributed to the high hardness and brittleness of ceramics. Due to the very low fracture toughness of ceramics, this damage strongly affects the strength of the machined components.

Numerous research has been carried out aiming to predict the severity of machining surface damage as a function of machining parameters in order to predict the strength degradation of the component (66) (67). Particularly severe are the microcracks induced by machining. These microcracks are similar to the typical median cracks observed after indentation fracture of ceramics (See Section 2.2.3). The optical observation of machining cracks right after the process is difficult due to the residual compressive stress field left by the tool that keeps the microcracks closed. If the cracks are loaded in tension, then they will be revealed.

Also, non-destructive techniques such as fluorescent penetration dyes or ultrasonic inspection can be used for quantifying the machining damage.

Normally, polishing follows the machining process for improving the surface quality and reduce the severity of defects; however, it is not possible to fully ensure the elimination of all the surface defects and the process is very time consuming and costly. This is the reason why some authors have proposed to implement self-healing mechanisms for recovering the virginal strength of machined ceramic components (68). In the case of the YSZ-MSBA self-healing composite the healing of machining cracks is not expected since the size of the sacrificial healing particles is much larger than the size of the microcracks. Nanosized healing particles are needed for achieving recovery of strength in machined self-healing ceramics.

3.5. Microstructure characterization

3.5.1 Optical characterization

A VHX-5000 of Keyence (Japan) has been used for light optical characterization of microstructure and surface elements. This is a computerized microscope with magnifications from 5x to 2000x. Automatic image stitching is available by a controlled-displacement stage and autofocus. The 3D tool allows to build 3D maps of the surface.

This equipment has been used for different purposes: measurement of indent diagonals and indentation crack length, determination of porosity volume fraction for highly porous materials and measurement of groove geometry in BD specimens.

3.5.2 Scanning electron microscope and energy-dispersive X-ray spectroscopy

A field-emission scanning electron microscope JSM 6500F from JEOL Ltd. (Japan) has been used for scanning electron microscopy (SEM). This microscope is equipped with an energy dispersive spectrometer (EDS) that operates with a ThermoFisher UltraDry detector using NoranSytem 7 software package for X-ray emission, spectra acquisition and analysis. There are several parameters that can be changed depending on the measurement. The working distance was normally 10 mm for acquisition of high resolution secondary electron and backscatter electron images. For elemental analysis with EDS a working distance of 25 mm is selected. The electron beam energy is set to 15 keV for high resolution images and lower energies (5-7 keV) for EDS analysis.

In the case of pure YSZ specimens and composite specimens it was necessary to apply a thin layer of carbon (about 20 nm) for preventing charging of the sample because the material is not conductive. An auto carbon coater JEC-530 (JEOL, Japan) and a FC-TM10 (JEOL, Japan) thickness monitor were used for this purpose.

3.5.3 X-Ray Diffractometry

For XRD analysis a Bruker D8 Advance diffractometer Bragg-Brentano geometry with graphite monochromator and Vantec position sensitive detector were used. Parameters like the diffraction angle 2θ range and the counting time per step depend on the measurement. The data acquired from this equipment is analyzed using Bruker software DiffracSuite.EVA vs 4.1.

3.6. Mechanical characterization

3.6.1 Experimental procedure for instrumented microindentation and nanoindentation

Depth-sensing micro- and nanoindentation were applied to determine elastic modulus, hardness and indentation fracture toughness. The nanoindenter is designed for providing accurate results for penetration displacements in the order of nanometers (theoretical resolution < 0.01 nm) and up to 500 µm, depending on the stiffness of the material. The load limit of the instrument is 0.5 N; hence in the case of the materials studied in this thesis (high Young's modulus) the maximum achievable penetration depth is in the range of 1-2 µm. The microindenter is designed to provide accurate results in the range of micrometers (resolution 0.02µm). The load limit in 2.5 kN, although the recommended maximum value is 500 N. Apart from this main difference, the working principle is the same. In Figure 4 a picture of both instruments is shown.

Figure 4 - Microindenter (left) and nanoindenter (right)

The nanoindenter is a MTS G200 of Keysight Technologies. The indentation system is coupled with an optical microscope and 4 stages are available for testing different specimens in case the machine operates automatically. Due to the high sensitivity of this machine and the extremely low displacement resolution (<0.01 nm) the equipment only operates under a certain threshold of ground vibration, so normally overnight. The equipment comes with several types of tips. For the purpose of this project a diamond Berkovich tip has been used, and it is normally checked under the optical microscope and cleaned before testing. Additionally, before the start of each test the machine is calibrated using a reference material (fused silica).

This machine offers several types of test. Only the Continuous Stiffness Measurement (CSM) technique was used in this project. For this option, it is necessary to know the parameters of the dynamic response of the indentation system. Typical vales can be found in the data sheet. Leaf spring stiffness is around 100 N/m, damping coefficient is 0.02 Ns/m and stiffness of the load frame is around 5 MN/m. From these parameters and the displacement response from the oscillatory force the software calculates the contact stiffness according to the model explained in Section 2.2.1.

All the measurements in the nanoindenter have been carried out following the same protocol and using the same test parameters. Only the maximum penetration depth was changed. The surface approach velocity was set to 10 nm/s, strain rate target 0.05 1/s, harmonic displacement equal to 2 nm, frequency target of 45 Hz and a surface approach distance of 1µm. The depth limit was initially selected to 1 µm, however after the first tests it was realized that the elastic modulus slightly decreases in the range from 500 nm to 1000 nm; hence the next tests were set with a maximum depth displacement of 2µm in order to ensure that the elastic modulus goes to an asymptote.

The surface of the specimens must be prepared according to the procedure in Section 3.4.1. Smooth and flat surfaces will provide less scatter in the results. The tests are done automatically. For setting up the measurement it is necessary to specify the position of the indents beforehand. In the case of bulk material random arrays of 25 indents were set. The interdistance between indents in the array is around 30 µm. In the case of the composites, indents are sufficiently small so as to be made either on top of a particle or on top of matrix. For each composite specimen 10 indents were made on top of particles and 10 on top of matrix. All these settings are selected in the control software of the nanoindenter called "Nanosuite".

The microindenter is a ZHU2.5 of Zwick. The indentation system is coupled with an optical microscope. This machine does not have the option of automatic testing.

Several types of tests can be set in the microindenter and also different types of indentation tips and from different materials are available. For the purpose of this project a diamond Vickers indenter was used and the test option was a force-controlled loading-unloading scheme. The software of the machine ("TestXpert") automatically calculates the contact stiffness from the unloading curve by fitting a power law between the points of 98% P_{max} and 20% P_{max}. The contact stiffness is calculated by computing the tangent to the power law in the point of 98% P_{max}. Hardness and elastic modulus are then calculated with the model explained in Section 2.2.1.

All the measurements in the microindenter have been carried out following the same protocol and test parameters. Only the load has been changed in order to study the load dependency of the measurements. The test is force-controlled and the same speed for loading and unloading was selected, equal to 5 N/s. The waiting time at the point of load application is 20 s. These values have been selected according to the experience with testing other ceramics.

Unlike the nanoindenter, the microindentation equipment is manual so load and position of the indent is selected before each measurement. In the first tests a load sequence from 2.5 to 20 N (in steps of 2.5 N) and from 50 to 200 N (in steps of 50 N) was performed. This was done for studying the load dependency of the measurements, but it was realized that it is not necessary to have such a small step size; so for the rest of tests the load sequence was 5-10-20-50-100-200 N. In each specimen 3 series of the same load sequence were done in order to perform a statistical analysis.

The surface preparation for the specimens tested in the microindenter was the same than for the nanoindenter and it is explained in Section 3.4.1. The position of the indents is selected manually and no distinction was made between the samples of pure material (YSZ) and composite because the indent size is big enough so as to cover matrix and several particles. For each serie all the indents were aligned in a row with an interdistance of 5-10 times the indent diagonal, as it is recommended in the ASTM standard for Vickers Hardness (38).

3.6.2 Experimental procedure for strength and fracture test set-ups

3.6.2.1 Test description

Two non-conventional test set-ups have been used for strength and fracture testing of the self-healing YSZ-MSBA composites. The lack of standardization of methods for strength and fracture testing of self-healing ceramics makes it necessary the use of novel techniques for characterization of the material. The main objective of these techniques is to create a controlled and slow-growing crack, so that it can be stopped and healed before total failure of the specimen. This turns into a major challenge when testing ceramics because of its low fracture toughness and tendency to rapid and uncontrolled crack growth.

The two set-ups for testing the YSZ-MSBA composite come from two tests already used for other applications, but the geometry of specimens and test set-up have been modified in order to achieve the slow and controlled crack growth. One is the Brazilian Disc (BD) set-up, which is commonly used for testing concrete. The other is a Wedge-Loaded Double Cantilever Beam (WL-DCB) test, which is less popular than the Brazilian Disc set-up. Several modifications were introduced for promoting the slow and controlled crack growth. In the BD set-up a central V-shaped groove is added for guiding the crack. A central hole is included for promoting the initiation of a crack in the centre of the specimen that will propagate towards the edges of the groove where two crack arrest holes were added for creating a very high compression stress at the crack tip when approaching the end of the groove. In the WL-DCB set-up also a crack guidance groove was included. A chevron notch was added in order to have a decreasing stress intensity factor as the crack propagates. A hole for crack arrest is also used in the WL-DCB set-up.

Both tests are displacement-controlled and the lowest displacement rate possible is selected in order to increase the chances of having a controlled and slow-growing crack. Both set-ups were designed for being mounted in a universal testing frame in which the load is introduced by displacing a bench. Four different outputs can be obtained. One is the reaction load in the fixed part of the set-up, which is measured by means of a load cell. The other three outputs are displacements, two measured by extensometers and the other is the displacement of the movable beam/bench of the loading frame. In Figure 5 a sketch of the set-up is shown, including the deformed state of the structure and the location where the displacements are measured.

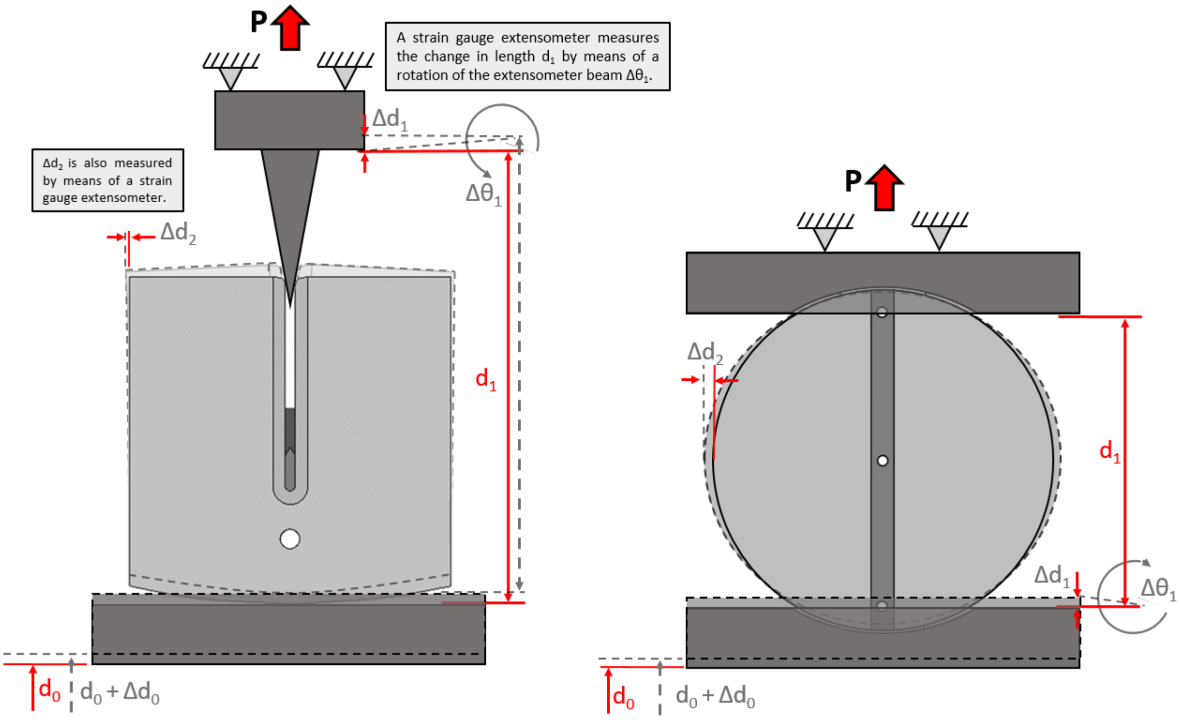

A strain gauge extensometer measures the change in length d_1 by means of a rotation of the extensometer beam $\Delta\theta_1$.

Δd_2 is also measured by means of a strain gauge extensometer.

Figure 5 – Sketch of the two set-ups for strength and fracture testing

Displacement Δd_0 is that of the bench of the loading frame. This displacement includes the deformation of the testing frame; hence it is higher than the real displacement that the specimen sees. This is the reason for measuring the displacement Δd_1. This displacement only corresponds to the change in length d_1, which is the closest value possible (within the set-up constraints) to the real displacement that the specimen sees. Additionally, a lateral displacement, Δd_2, is measured. This displacement is directly related to the crack mouth opening in both specimens. As it can be seen in Figure 5, the points of measurement of displacement are different in the BD and WL-DCB set-up. This is due to constraints of the set-up regarding the placement of the extensometers.

Hardened steel components are used for loading and aluminum components are used for auxiliary extensions. Additionally, in the BD set-up, two very thin (0.25 mm) annealed nickel plates are used for the contact between the specimen and the loading jig. The deformation of the nickel plate accommodates slight geometry differences and surface roughness in between these two elements in order to avoid undesirable high stress concentrations that might lead to premature failure of the specimen.

Technical drawings of the specimens, loading components and auxiliary elements for placement of extensometers can be found in Appendix 3.2.

3.6.2.2 Test procedure

The same equipment is used for the two strength and fracture test set-ups (BD and WL-DCB set-ups), with variations in test parameters and configuration.

A 100 kN electromechanical universal test frame Instron 5500R (UK) is used. For controlling the equipment and acquiring test results Instron software Bluehill is used. A 10 kN and a 1 kN load cell are also available. The noise range increases with the maximum load, so a suitable load cell must be selected depending on the expected maximum load in order to have the lowest noise range. Three different displacement outputs are obtained. One is measured by the displacement bench of the test frame. The other two displacements are measured by two dynamic strain gauge extensometers Instron 2620 (UK). The direct measured value is the voltage difference from a Wheatstone bridge of strain gauges that is installed inside the extensometer. The transducer turns this value into displacement in between the two knife edges of the extensometer. When the knife edge moves, the extensometer beam rotates and this is sensed by the strain gauge. All the extensometers are calibrated before use. A special calibration fixture that comprises a micrometer is used. The extensometer is mounted in standard position (using rubber bands) and ensuring that no pre-strains are introduced. With the micrometer and the software the extensometer transducer is calibrated.

Acoustic emission measurements are done with a Physical Acoustics AEWin 1.70 (2005) software module. The sampling rate employed is 2 MHz with a 20 dB amplification factor. The acoustic signal is triggered when the signal level from the microphones exceeds 5mV. Prior to mounting the sample in the test set-up two microphones are attached to one of the surfaces using paraffin wax.

A high-speed camera Phantom Miro 310/311 of Vision Research (USA) is used for capturing the fracture moment. The camera captures the groove of both specimens where it is expected that the crack will appear. Suitable light sources are used for obtaining a clear image of the groove. A LabVIEW software is used for data acquisition from the high speed camera. This software is connected to the Instron load frame and the camera. The software saves the recording of the camera until the memory is full, then it deletes all the data and continuously records new data. The software is triggered when there is a drop in load of certain predefined magnitude. When the software is triggered, it does not delete the last recording from the camera, that should correspond to the moment of fracture.

A detailed explanation on how to prepare and operate these two test set-ups can be found in the test protocols for WL-DCB and BD tests in Appendix 3.3. Also it is explained how to check the accuracy of the extensometers measurement.

3.6.2.2.1 Wedge-Loaded Double Cantilever Beam set-up

The WL-DCB test set-up consists of an Instron universal test frame, suitable loading materials and auxiliary extensions, a 10º wedge made of tempered steel, two extensometers, a high speed camera with suitable light sources, and two microphones attached to an acoustic emission equipment.

For the WL-DCB set-up a 1 kN load cell is used because it is expected that the maximum test load is much lower than 1 kN. This was checked by testing a dummy YSZ specimen.

The two extensometers are placed using auxiliary extensions and rubber bands. It is important to notice that the configuration of the extensometers in this set-up is not the standard configuration as proposed by the manufacturer in which the extensometer must be in a free-standing position and attached directly to the specimen using rubber bands. The point of contact between the specimen and the extensometer is a standard knife edge that keeps the same point of contact during displacement of the specimen and rotation of the extensometer. For the WL-DCB set-up is not possible to use a free-standing configuration; hence the unmovable beam of the extensometer is attached with rubber bands to a fixed surface. The manufacturer recommends not to fixed the extensometer using the moveable beam of the device. In case of using this non-standard configuration a customized knife edge (See Appendix 3.3) must be used in order to ensure that the same point of contact is kept during testing for improving accuracy of the measurement.

A special auxiliary extension is also used for placing the light source of the camera. The light is set so as to have a clear image of the groove in the specimen. The camera is also focused to this area.

Details of the set-up can be seen in Figure 6.

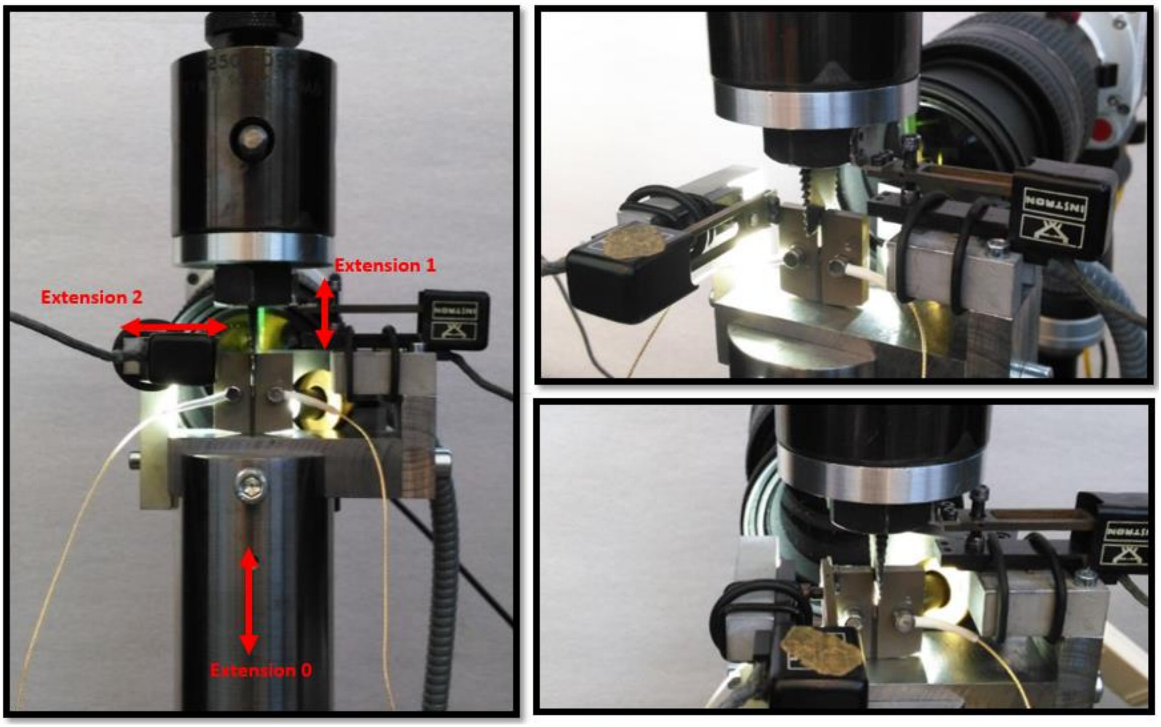

Figure 6 - Details of the WL-DCB test set-up

The control parameters are set before the start of the test. The test is controlled by the crosshead displacement of the bench. A very slow displacement rate of 0.01 mm/min is selected to promote stable crack growth and to avoid complete fracture of the specimen.

The drop in load at the moment of fracture will be used as trigger for switching from loading to unloading scheme. Based on previous experience with a dummy specimen, a drop in load of 10% of the maximum load is selected. A load threshold of 10 N is selected. Below this value there will be no switch from loading to unloading ramp. For the unloading ramp a speed of 0.1 mm/min is selected. Since the specimen will already be fractured, it is not necessary to keep the slowest rate possible.

Before the start of the test the extensometers are brought into contact with the specimen. First, the specimen is preloaded up to 1-10 N until it is fixed. Both extensometers are balanced to zero before touching the specimen. Then, both are brought into contact. It is important to notice that there will be a pre-strain that must be taken into account during post-processing. The bench displacement is set to zero once both extensometers are touching and the specimen is preloaded.

3.6.2.2.2 Brazilian Disc set-up

The BD test set-up consists of an Instron universal test frame, suitable loading materials and auxiliary extensions, thin Ni deformable plates, two extensometers, a high speed camera with suitable light sources, and two microphones attached to an acoustic emission equipment.

A 100 kN load cell is used because it is expected the maximum load of some of the specimens to be higher than 10 kN. Two dummy YSZ zirconia samples were tested in order to determine typical test parameters.

Unlike the WL-DCB set-up, in the BD set-up one of the extensometers (Extensometer 1 that measures the displacement in between the upper and lower sample holders) can be placed following the standard rules imposed by the manufacturer. The extensometer is attached to the upper and lower sample holder using rubber bands and standard knife edges. For the extensometer 1 it is necessary to use one of the standard 12.5mm extension, that is screwed to the unmovable beam of the extensometer as recommended by the manufacturer. In the case of the extensometer in contact with the specimen (Extensometer 2 that measures the lateral displacement of the sample) the configuration is non-standard. The same configuration than for the extensometers of the WL-DCB set-up is used, using the customized knife edge that realizes the same point of contact during all the test (See Appendix 3.3).

The loading elements are two stiff punches in which the sample holders are placed. The sample holders have a curved surface in order to have a surface contact (and not line contact) with the specimen. A thin pure Ni plate (LS378859 of Goodfellow, UK) of 0.25mm thickness is placed in between the specimen and the holder. The purpose of this plate is to accommodate the difference between the shapes of the specimen and the sample holder. In this way the contact area is increased and the possibility of creating dangerous stress concentrations in the load introduction area decreases. The pure Ni plates, that come in as rolled condition, must be annealed in order to recrystallize the structure and grow the grain for making the plates softer. The Ni plates are cut to the necessary dimensions and annealed at 1000 ºC during 1 hour in Ar atmosphere.

Details of the set-up can be seen in Figure 7.

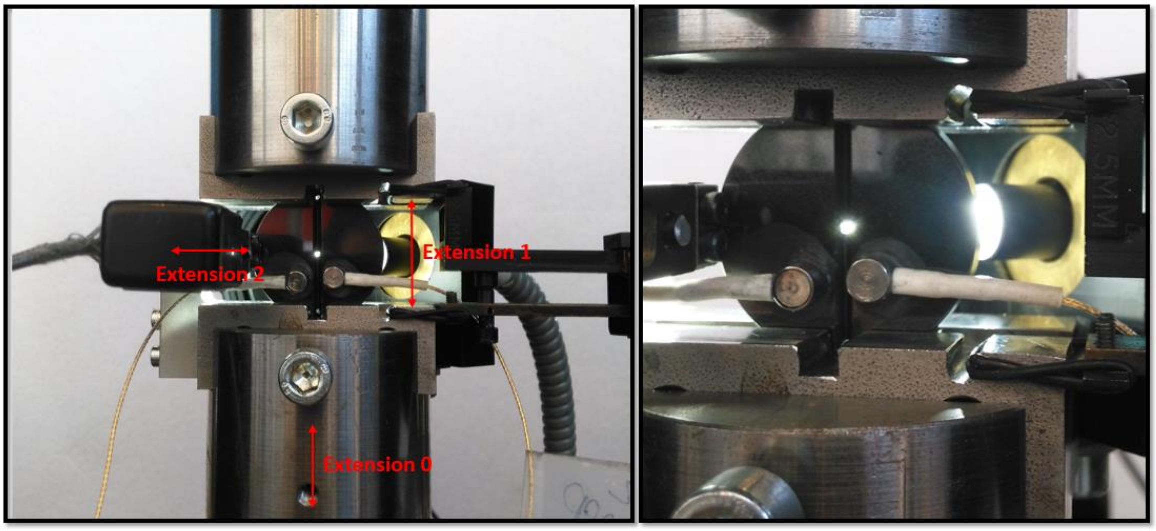

Figure 7 – Details of the BD test set-up

The BD test set-up consists on a preloading, loading and unloading scheme. The switch from loading to unloading scheme is triggered by the controlled fracture of the specimen. The test is controlled by the crosshead displacement of the bench of the load frame. The preloading is done for deforming the Ni foils placed in between the holder and the specimens so that the plastic deformation associated with this element can be neglected from the load-displacement curve of the fracture test. Based on previous experience with dummy BD samples, the preload is set up to 3 kN with a displacement rate of 0.01 mm/min. The unloading is triggered when the load cell senses 3 kN and it is unloaded also with 0.01 mm/min. The fracture test starts right after unloading from the preload (the unloading is stopped at 100 N approximately). For the loading scheme the same rate is selected, 0.01 mm/min, and the switch to the unloading ramp will be triggered by the controlled fracture of the specimen. A 1% drop in load is selected for triggering the switch from loading to unloading. The load threshold is set at 3 kN, which means that the switch from loading to unloading will not be triggered if fracture (and subsequent drop in load) occurs below 3 kN. For the unloading scheme the same rate, 0.01 mm/min, is selected. All these test parameters are selected based on the experience with testing several dummy samples.

Before the start of the test the extensometers and microphones must be installed. First, the microphones are glued to the sample. The specimen is then placed in the set-up, taking special care on the alignment, and it is preloaded up to 100 N, approximately. Then, the extensometers can be installed. Extensometer 1 is attached with rubber bands to the set-up and balanced to zero. Extensometer 2 is first balanced to zero and then brought into contact with the specimen. The extension 0 is also zeroed at this stage.

4 Results and discussion

4.1. Material analysis and proof of healing

In this chapter the results are presented for the study of composition and microstructure analysis of the YSZ-MSBA self-healing composites manufactured by spark plasma sintering. The microstructural analysis of the two components (matrix and material of the healing particles) manufactured separately is discussed in Section 4.1.1. The composition and microstructure of the sacrificial healing particles is rather complex; hence it is important to address a microstructural analysis of monolithic MSBA manufactured by SPS. In Section 4.1.2 the microstructure of the self-healing composite manufactured by SPS is discussed. Finally, Section 4.1.3 shows the potential for healing of this composite material based on local and controlled high temperature oxidation of the sacrificial healing particles.

4.1.1 Microstructure analysis of monolithic MSBA and YSZ

The material for the matrix of the self-healing composite is zirconium oxide (ZrO_2) doped with yttrium oxide (Y_2O_3), yttria-stabilized zirconia (YSZ). This is the material used as a top coat of the thermal barrier coating system (See Section 1.1) and it is a fix requirement in the design of the self-healing thermal barrier coating.

Zirconia undergoes two phase transformations with increasing temperature. First, from monoclinic to tetragonal at 1173 ºC and then from tetragonal to cubic at 2370 ºC. The tetragonal-monoclinic transformation is associated with a significant volume change (5-9%) that compromises the stability of the material as many microcracks are generated due to internal stresses (69). By doping with yttria it is possible to make the tetragonal phase stable at room temperature. However, even tetragonal YSZ undergoes a stress-induced martensitic transformation from tetragonal to monoclinic, which is beneficial for the mechanical properties, but not for the thermal barrier coating application. The state of the art for TBCs is doping with 7-8 wt% Y_2O_3 because the metastable t' phase is formed, that does not undergo martensitic transformation (4).

In the present work to types of YSZ have been used (See Section 3.1), one with 4.5-5 mol% yttria (Amperit) which is the material for the TBC and the other 3 mol% yttria (Tosoh). Both materials are analysed and compared. In Figure 8 the result of the XRD analysis of both materials sintered as a monolithic disc is shown.

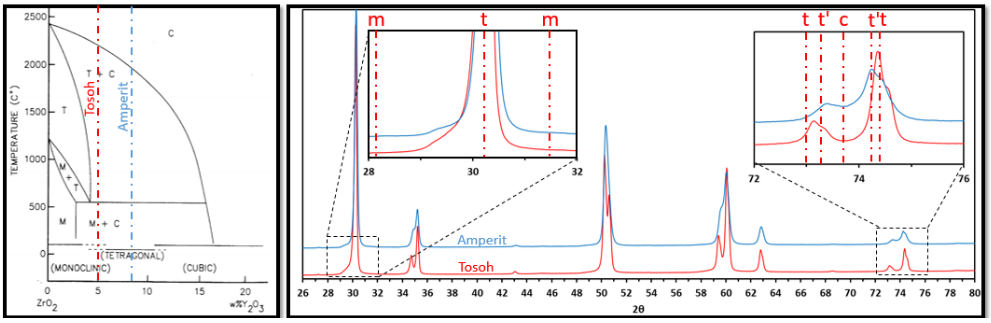

Figure 8 - Phase equilibrium and XRD patterns of pure YSZ from Tosoh and Amperit powders (before annealing and sintered at 1200 ºC). Phase diagram adapted from (70) and XRD references from (71).

As it can be seen from the results of XRD, there is no monoclinic phase present in any of the two YSZ materials, neither cubic phase. According to the phase diagram, at the sintering temperature (1200 ºC) both tetragonal and cubic are the stable phases, however according to the XRD result only the tetragonal remains at room temperature. This can be seen in the detail of the XRD pattern between 72 and 76º. This is the main area of interest for distinguishing tetragonal (t), t' and cubic (c) in a YSZ pattern. No peak is found in the position of the cubic phase, so it can be said that most probably this phase is not present. Regarding the presence of t' phase in the Amperit YSZ, the XRD result suggests the existence of this phase over the tetragonal; while in the Tosoh material the peaks are closer to the tetragonal phase. Therefore, although it cannot be fully ensured because the peaks of t and t' are very close, it can be concluded that the main phase in the Amperit material is t' and tetragonal in the case of Tosoh.

The material for the healing particles is $MoSi_2$ with additions of B and Al in substitution of Si (See Section 1.1). The addition of B and Al leads to changes in the microstructure of the particles that have an effect on the mechanical properties and the performance of the self-healing mechanism. The addition of Al to $MoSi_2$ is well reported in literature. When adding Al to the stable tetragonal C11b phase of $MoSi_2$ it substitutes Si up to the solubility limit around 3 at%. Above this limit a new phase, hexagonal C40, appears. By further adding aluminium the whole microstructure evolves to the hexagonal C40 phase (72) (73) (74). Less literature is available on the Boron addition to $MoSi_2$. Unlike aluminium, boron does not dissolve in $MoSi_2$ and it precipitates in the form of borides with composition Mo_xB_y (72).

Plates of monolithic $MoSi_2$ with addition of B and Al were manufactured by SPS using the same powders than for making the composites. Three different plates were made from three different materials: $MoSi_2B$ (2 wt% B), $MoSi_2BAl$ (2 wt% B, 6 wt% Al) and $MoSi_2BAl$ (2 wt% B, 12 wt% Al). These are nominal design compositions. These plates were produced for studying the mechanical properties of the healing particles material and for performing microstructural analysis.

The microstructural analysis shows that the two materials containing nominal 6 and 12 wt% Al exhibit a fully hexagonal crystal structure. Other minor phases are observed in the microstructure like borides, Mo_5Si_3 and oxides. In the case of the alloy that does not contain aluminium a fully tetragonal crystal structure is observed, also with oxide impurities and borides present in the microstructure. The phases present are in accordance with the phase equilibrium shown in the phase diagrams (See Figure 10) and the presence of oxide impurities is related to the difficulty of getting a sufficiently low P_{O_2} when sintering powders in the SPS and the presence of oxygen entrapped in the starting powders. The presence of oxide impurities in polycrystalline $MoSi_2$ is a common phenomenon also observed by other authors (75) (76) and it is difficult to avoid it. One solution is to alloy $MoSi_2$ with elements that will preferentially oxidize over Si, like C (75) or Al as it is done in this project (although not with the objective of improving the mechanical performance).

Taking a closer look to the results of the elemental and X-ray diffraction analysis the differences between the three materials can be identified. Figure 9 shows the microstructure of the three materials and the results of the XRD analysis performed on the surface. In all the cases the major phase has a grey-like contrast, which is the hexagonal $MoSi_2$ phase in the case of the Al-containing alloys and fully tetragonal phase in the case of the alloy only containing boron. According to the EDS analysis, the lighter areas are borides in all the cases. However, the XRD shows that different types of borides are present in the materials. The 2wt%B-6wt%Al containing material and the 2wt%B containing alloy exhibit the same Mo_2B_5 boride, but the 2wt%B-12wt%Al containing alloy presents a boride of type MoB. Additionally, the XRD of the 2wt%B-12wt%Al containing alloy gives evidence of the presence of Mo_5Si_3 phase. This phase normally shows a light-grey contrast similar to the borides. The dark areas present in all microstructures are oxide impurities coming from the manufacturing process. These phases are not observed in the XRD pattern because of the small volume fraction and also, in the case of SiO_2, this is an amorphous phase so it does not appear in the diffraction pattern. The EDS analysis indicates the presence of only SiO_2 in the case of the 2wt%B containing alloy. In the case of the Al containing alloys the EDS analysis suggests that the majority of impurities are aluminium oxides, however silicon peaks appeared in some cases. This suggests the presence of SiO_2 or mullite (SiO_2/Al_2O_3), but it could be also the reflection from the surrounding $MoSi_2$ matrix.

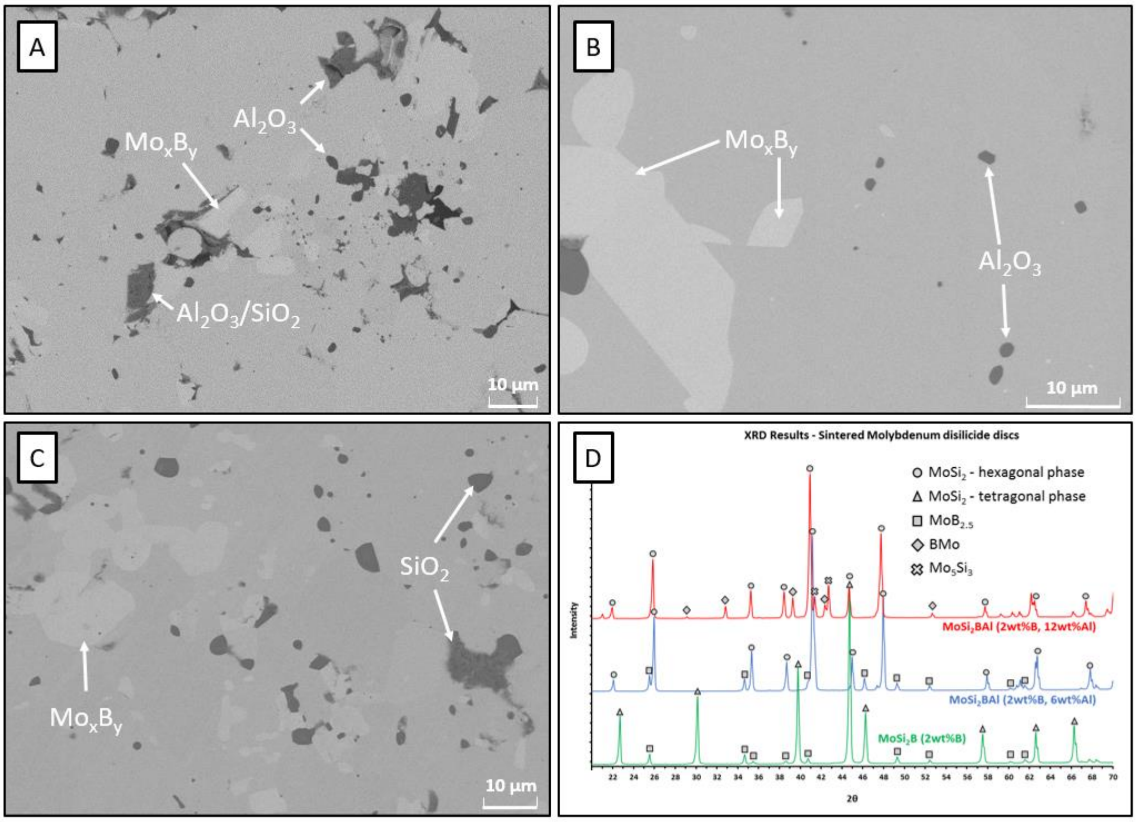

*Figure 9 – Typical microstructures (BEI images) of sintered plates of (**A**) $MoSi_2BAl$ (2 wt%B, 6 wt%Al), (**B**) $MoSi_2BAl$ (2 wt%B, 12 wt%Al) and (**C**) $MoSi_2B$ (2 wt%B). XRD results of the three specimens is shown in **D**.*

The previously explained observations describe the stable microstructure of the three different $MoSi_2$ alloys manufactured at 1500 °C. A last step in the analysis of the microstructure consists on comparing the results with the equilibrium phase diagram of the material at the sintering temperature. During cooling there is not enough time for diffusion of the elements so the microstructure at 1500 °C is assumed to be “frozen” at room temperature. This is the reason for analyzing the equilibrium at 1500 °C. Anyhow, the microstructure should not be much different if a much lower cooling rate is applied because by looking at the ternary diagrams at lower temperatures the phase equilibrium does not deviate much from the one at 1500 ºC.

Figure 10 shows the ternary diagrams of Mo-Si-Al and Mo-Si-B systems. The first important observation is the presence of an equilibrium line in the Mo-Si-Al diagram in which only $MoSi_2$ is present by adding aluminum in substitution for Si. Along this line there is first a fully tetragonal structure, then coexisting tetragonal and hexagonal, followed by fully hexagonal phase. However, in the case of Mo-Si-B system there is no solubility of B in the MoSi$_2$ so the addition of boron leads to the formation of Mo$_x$B$_y$-type compounds. The comparison of the XRD results with the equilibrium diagrams suggests that the observed structure in the manufactured monolithic MoSi$_2$ plates is feasible, in terms of thermodynamic equilibrium. The position of the three compositions have been plot in the diagrams of Figure 10, but the boron addition in the Al-containing alloys have been subtracted in order to make the representation easier and more realistic. In the case of the 2wt%B material and the 2wt%B-6wt%Al material only MoB$_{2.5}$ is observed in the XRD patterns, apart from the major MoSi$_2$ phase. This suggests that the addition of Al displaces the point A in the Mo-Si-B diagram along the Mo-constant line. However, this trend is not followed by the 2wt%B-12wt%Al containing alloy. The XRD pattern in this case shows the presence of Mo$_5$Si$_3$ and MoB. This suggests that the point A in the Mo-Si-B diagram is displaced to the left, to the area where MoB, MoSi$_2$ and Mo$_5$Si$_3$ coexist. In the case of the Mo-Si-Al diagram the result suggests that the point C is displaced up to the area where the hexagonal phase coexist with Mo$_5$Si$_3$. Two possible explanations for this phenomenon are considered. First, the combined effect of Al and B (that would be better represented in a 4-elements quaternary diagram) could be the reason for this phase equilibrium in the 2wt%B-12wt%Al containing alloy. The second reason, more likely, is the loss of part of the aluminum during the manufacturing process. The low melting point of aluminum (≈700 °C) leads to partial loss of the aluminum that melts during the SPS process and it comes out of the mold. This has been observed after sintering of the plates and the amount of melted Al was even more pronounced for the 12 wt%Al containing alloy. This loss is higher the higher the content of aluminum so it makes sense that the deviation from the Mo-constant line in the Mo-Si-Al ternary diagram is more pronounced in the 12wt%Al containing alloy. In the case some Al is lost during manufacturing the ratio of Mo and Si automatically increases, so the composition would displace to the lower-left side in the Mo-Si-B diagram and to the up-right side in the Mo-Si-Al diagram. So the final composition, in both diagrams, would be in an area where the phases in equilibrium are the ones observed in the XRD pattern: MoB, MoSi$_2$ and Mo$_5$Si$_3$.

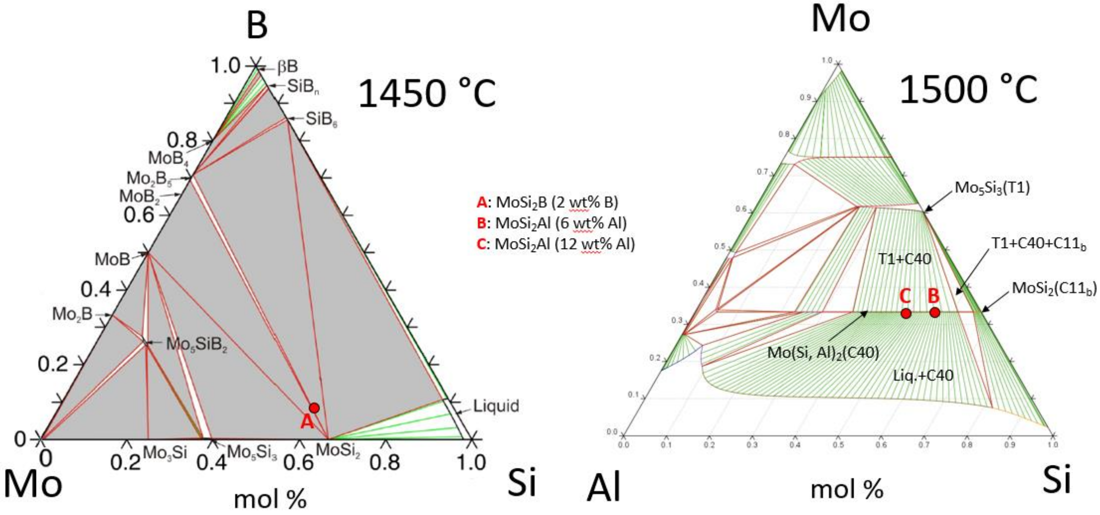

Figure 10 – Ternary diagram of Mo-Si-Al for 1500 ºC (right). This diagram has been done in ThermoCalc by using a thermodynamic database extracted from (77). Ternary diagram of Mo-Si-B system (left) for a temperature nearly equal to the sintering, adapted from literature (78).

4.1.2 Microstructure analysis of the self-healing composite

In this section the microstructure of the particle-dispersed composite will be presented. Cross-sections of three different composites have been analysed: YSZ-10MSB6A, YSZ-

10MSB12A and YSZ-10MSB6Asol-gel (See Section 3.1). In all the cases the YSZ matrix has been prepared from Tosoh powders. Powders were sintered at 1200 °C for 1 hour. The composites were annealed in Ar atmosphere (1100 °C for 16 hours) to create an alumina protective shell.

With the analysis of the healing particles powder before sintering it can be concluded that the phases present are not the stable ones, as compared with the results of the previous section. In both the 2wt%B-6wt%Al containing and 2wt%B-12wt%Al containing powders the tetragonal and hexagonal phase of $MoSi_2$ are present, although according to the previous results the only stable phase for these aluminium contents is hexagonal. This suggests the existence of a non-homogeneous aluminium distribution in the initial bulk $MoSi_2BAl$ before been processed to powder. This is an important issue to take into account because the powders of tetragonal phase are particles that will have an initial low content of Al and, therefore, the protective shell might not be sufficient to prevent premature oxidation of the particles that are not opened by a crack. Despite this drawback, the XRD results show that the major phase in both cases (powder containing 6 and 12 wt% Al) is the hexagonal, being even higher the proportion for the 12 wt% powder. Further analysis on the composites after sintering and annealing (See Figure 12) shows that in the 2wt%B-6wt%Al containing composites the $MoSi_2$ tetragonal becomes the major phase and there is not remaining hexagonal phase. This means that most of the aluminium was depleted to the particle-matrix interface to form the alumina protective shell. In the case of the 2wt%B-12wt%Al containing composites the major phase is hexagonal even after annealing, although a slight increase of the tetragonal phase is observed during annealing. SEM observation on the microstructures does not show substantial changes in the microstructure after annealing treatment, but it is a useful tool for characterizing the quality of the encapsulation process and assess the presence of undesired phases. EDS elemental analysis does show evidences of the Al depletion during annealing process and it has been used for identifying the phases present in the microstructure of the composites. It can be said that the main outcome from the elemental and optical analysis is that the microstructure of the composite is very heterogeneous, with a majority of particles showing a good encapsulation, but also cases of particles that do not have shell or it is incomplete due to impurities or low aluminium content.

The first step in the microstructural assessment of the YSZ-MSBA composite is to analyse the initial status of the healing particles before sintering. XRD pattern of the raw powders is shown in Figure 11. The particles with sol-gel encapsulation are the same than the 2wt%B-6wt%Al containing particles, so the XRD pattern was not included because the only difference is the presence of very weak corundum peaks (α-Al_2O_3).

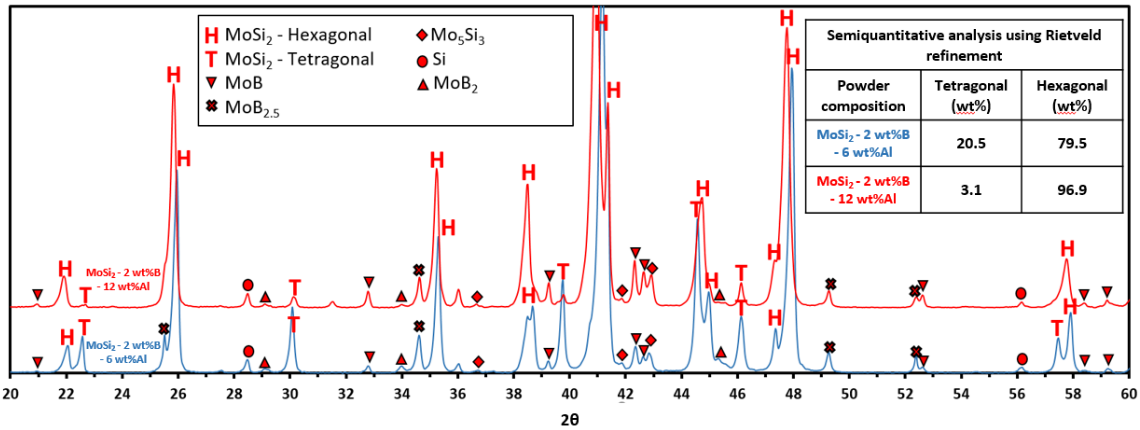

Semiquantitative analysis using Rietveld refinement

Powder composition	Tetragonal (wt%)	Hexagonal (wt%)
$MoSi_2$ - 2 wt%B - 6 wt%Al	20.5	79.5
$MoSi_2$ - 2 wt%B - 12 wt%Al	3.1	96.9

Figure 11 – XRD of raw MoSi2BAl powders for 2 wt% B-6 wt% Al (blue) and 2 wt% B-12 wt% Al (red)

The main outcome of the results shown in Figure 11 is the presence of tetragonal phase in the powders of both compositions, being higher in the case of powders containing 6 wt% Al. According to the previously discussed results of section 4.1.1, the only stable phase for the two types of powders (with 6 and 12 wt% Al) used in this work is the hexagonal phase. This suggests that during manufacturing of this material (probably casting) the aluminum distribution during cooling was not homogeneous; thus tetragonal phase was formed in the Al-poor areas. The presence of tetragonal phase in the initial powder is detrimental for the quality of the composite because it will lead to presence of some poorly encapsulated particles.

Other phases are observed in the XRD patterns of the raw powders. Mo_5Si_3, MoB, MoB_2 and $MoB_{2.5}$ are present in both powders, been higher the content of Mo_5Si_3 and MoB in the 2wt%B-12wt%Al containing powder and higher the content of MoB_2 and $MoB_{2.5}$ in the 2wt%B-6wt%Al containing powder. This result is not in complete accordance with the ternary diagrams and results of the previous section in which it was concluded that $MoB_{2.5}$ is the only stable phase in the 2wt%B-6wt%Al containing alloy, apart from the main $MoSi_2$-hexagonal; and Mo_5Si_3 and MoB are the only stable phases in the 2wt%B-12wt%Al containing alloy apart from the $MoSi_2$-hexagonal. Again, this is probably due to inhomogeneity of the casted material that was milled to powders. Additionally, the XRD result indicates the presence of Al and Si impurities.

The study of microstructural evolution after sintering of the composite and annealing treatment by analysing the X-ray diffraction patterns is more complex than the raw powders because the composites only contain 10 vol% particles so the peaks from the phases present in the healing particles are very weak as compared with the peaks of the matrix material. In Figure 12 the XRD patterns of polished cross-section of the composites after sintering and after annealing are shown.

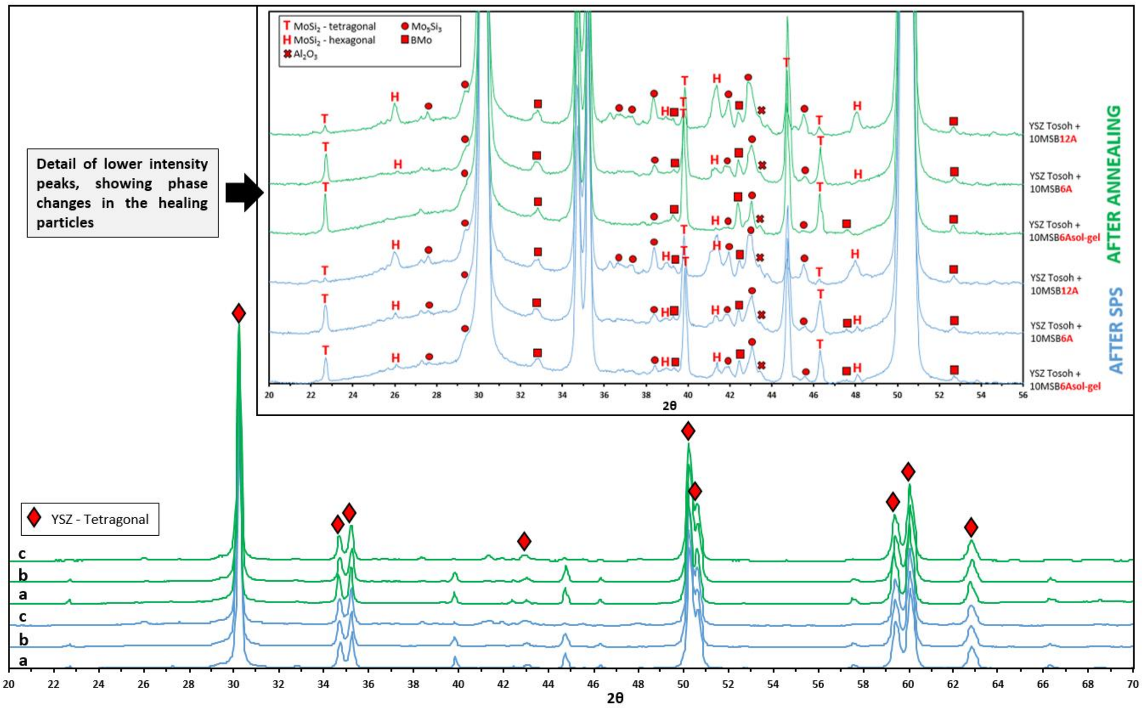

*Figure 12 – X-Ray diffraction patterns of polished cross-sections of three different composites before annealing treatment (blue) and after annealing (green). The three composites are (**a**) YSZ-MoSi2BAl (2 wt% B, 6 wt% Al) with pre-encapsulated particles via sol-gel, (**b**) YSZ-MoSi2BAl (2 wt% B, 6 wt% Al) and (**c**) YSZ-MoSi2BAl (2 wt% B, 12 wt% Al).*

In all the cases the matrix is fully YSZ-tetragonal phase, which is in accordance with the phase diagram for the sintering temperature, 1200 °C (See Figure 8). The composition of the healing particles embedded in the YSZ matrix can be analysed by zooming in to the low intensity peaks. In the case of the 2wt%B-6wt%Al containing composites the major phase is the $MoSi_2$-tetragonal, while the raw powder had around 80% hexagonal and 20% tetragonal. This phase change is due to the aluminium depletion from the particles to the interface and formation of Al_2O_3 during exposure at high temperature in low P_{O_2}. By looking at the ternary diagram of the Mo-Si-Al system in Figure 10 it can be seen that when reducing the Al content, the composition moves to the right towards the area where tetragonal and hexagonal coexists and then by further decreasing the Al content the equilibrium point moves to the area of fully tetragonal phase. Hence, during sintering there is a phase change in most of the particles. After annealing, the only significant change observed is the slight decrease of the hexagonal peaks in the 2wt%B-6wt%Al containing composites. In the case of the 2wt%B-12wt%Al containing composites the result is different. A majority of hexagonal phase still remains after sintering and even after annealing. However, this does not necessarily mean that the alumina shell has not been formed. The 2wt%B-12wt%Al containing composites have a larger Al reservoir, so it is more difficult to deplete all the aluminium to the particle/matrix interface. A slight increase of the tetragonal peaks is observed after annealing, so this proves that the annealing treatment at low P_{O_2} promotes the depletion of Al to the interface and the formation of Al_2O_3. Besides the main tetragonal and hexagonal phases of $MoSi_2$, other phases are identified. Mo_5Si_3 and MoB are present in all the composites, being higher the amount of Mo_5Si_3 in the 2wt%B-12wt%Al containing composites, as it was expected from the analysis of the raw healing particles powder.

The main conclusion that can be extracted from this analysis is that the concept of in-situ encapsulation of the particles during manufacturing and heat treatment by alloying the healing particles with Al is feasible. However, no information regarding the quality and morphologies of the alumina shell can be extracted from these XRD results.

The quality assessment of the encapsulation of the particles and the overall morphology of the composites is done using a combination of microscopical (SEM) and elemental analysis. In Figure 13 a selection of the most typical microstructures of the three types of composites (YSZ-10MSB6A, YSZ-10MSB12A and YSZ-10MSB6Asol-gel) are presented.

The extraction of quantitative data from the SEM observation regarding the quality of the shell is difficult because of the large heterogeneity of the microstructure and the particles morphology. Despite this, some differences can be noticed between the three types of composites. In general, it has been observed that the alumina shell is thicker in the case of the YSZ-10MSB12A and YSZ-10MSB6Asol-gel composites. Some cases of excessive alumina shell formation have been observed in the YSZ-10MSB12A composites, as it can be seen in Figure 13-F'. This phenomenon has been observed only in the 12 wt% Al containing composites. In addition, the shell of the YSZ-10MSB6Asol-gel composites is more homogeneous than the shell of the YSZ-10MSB12A composites. As it can be seen in Figure 13 - E' and F', the interface of some of the particles is formed by a mix of Al_2O_3 and Mo_5Si_3; while in the case of the YSZ-10MSB6Asol-gel composites the shell is normally continuous along the whole interface and there is no interference between the Al_2O_3 and Mo_5Si_3 layers. The presence of this Mo_5Si_3 layer is another consequence of the encapsulation process and it is mainly caused by the formation of some SiO_2 in the interface. During high temperature exposure at very low P_{O_2} the aluminium reacts first (as compared with silicon) because of its lower Gibbs free energy; hence according to this principle only a layer of alumina should be formed in the interface with the particles because once it is formed it does not allow the oxygen to go inside the particle (due to the low diffusion of oxygen in alumina). However, in reality the irregular shape and non-homogeneous composition of the particles make the aluminium distribution not even. Therefore, there are spots where silica is preferentially forming and this causes the formation of Mo_5Si_3 (the composition moves up towards the area where $MoSi_2$ and Mo_5Si_3 coexist according to the ternary diagram in Figure 10). This is one of the explanations for this continuous Mo_5Si_3 layer that can be observed in almost all the particles shown in Figure 13. Another possible explanation is the depletion of Al from the particle to the interface. By looking again to the ternary diagram of Mo-Si-Al it can be seen that when the content of Al is lowered and the Si and Mo content are kept constant the mole fractions of Mo and Si increase so the composition moves up and right towards the area where $MoSi_2$ and Mo_5Si_3 coexists. The problem with this hypothesis is that it does not clearly explain why a uniform layer is formed between the particle and the alumina shell. According to this hypothesis the Mo_5Si_3 should be present in the whole particle because the depletion of aluminium occurs in all the particle. A third, less likely, explanation for this phenomenon is the existence of a different alumina phase rather than the desired α-Al_2O_3. There might be other alumina phases that are more oxygen transparent, so this would explain the formation of silicon oxide and Mo_5Si_3 in between the particle and the alumina layer.

Regarding the morphology of the shell in the YSZ-10MSB6A composites, the alumina layer is generally thinner than in the other two cases, but it is also quite continuous and homogeneous as in the YSZ-10MSB6Asol-gel composites. However, in some cases the particles only exhibit a Mo_5Si_3 layer in the particle-matrix interface. This is an undesired phenomenon because the particles are not protected and they will oxidize upon high temperature exposure in air. The same phenomenon is observed in the YSZ-10MSB12A composites, but not in the case of composites with sol-gel pre-encapsulation.

Another interesting finding of the SEM/EDS analysis is the presence of molybdenum borides in the particles, as it is expected according to the thermodynamic equilibrium and the previous explanations of Section 4.1.1. From the oxidation and self-healing performance point of view the presence of these borides is beneficial because upon oxidation at high temperature they lower the viscosity of SiO_2, enhancing the filling of cracks. However, from the point of view of encapsulation and stability at high temperature, the borides are undesired because they do not dissolve aluminium. When a large boride phase is present in the particle-matrix interface, no alumina protective shell will be formed. The same applies when large precipitates of Mo_5Si_3 are present at the interface. An example of this is shown in Figure 13-E’, where it can be noticed the absence of alumina shell in between the molybdenum boride and the matrix. Also in one of the figure showing an overall picture of the YSZ-10MSB6A composite it can be seen a Mo_5Si_3 impurity. These are particle that are entirely Mo_5Si_3 and are they not encapsulated.

A last important observation from this analysis is the presence of a finely dispersed distribution of alumina in the zirconia matrix (small black dots present in all the pictures of Figure 13). This is probably by the presence of Al in the raw powders of the healing particles. During wet mixing of powders, the Al impurities get mixed in the zirconia powders and after sintering they appear as a finely dispersed distribution of alumina spots.

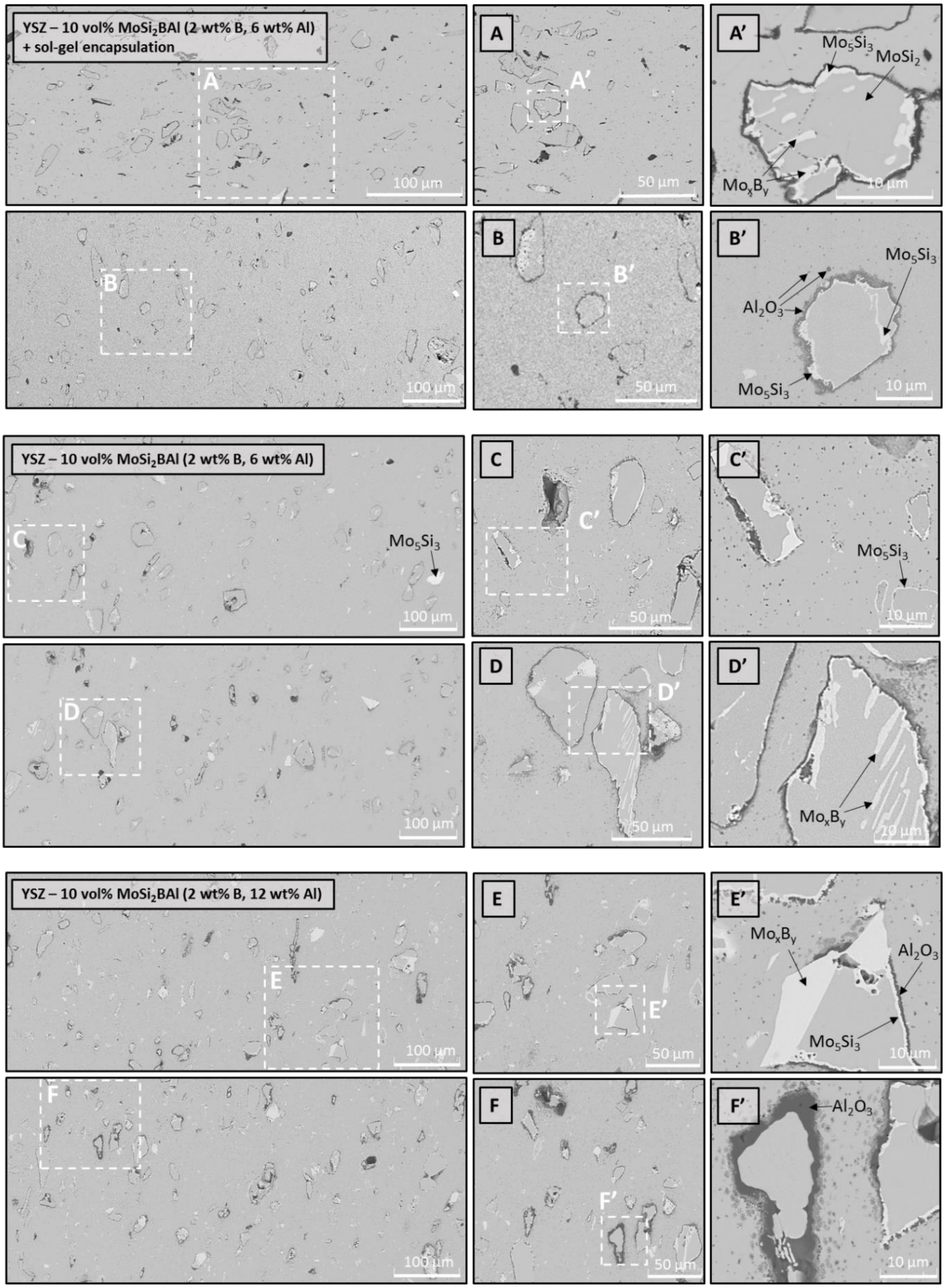

Figure 13 – Typical microstructures of the three types of composites after annealing: YSZ + 2 wt% B-6 wt% Al (with and without sol-gel pre-encapsulation) and 2 wt% B-12 wt% Al

4.1.3 Proof of healing concept

The working principle of the self-healing mechanism of the YSZ-MSBA self-healing composite has been studied through indentation crack-healing. The study of the self-healing capability based on indentation crack healing presents several limitations: i) indentation cracks are used in this study while the types of cracks that this system will encounter during service are cracks due to CTE mismatch (thermal stresses), ii) only a surface analysis (2D) is performed, and iii) the material is manufactured via SPS and fully dense in order to neglect porosity effect in the self-healing reaction.

The outcomes of indentation crack healing studies on the YSZ-MSBA system show promising results on its self-crack-healing ability. The self-healing reaction can be successfully triggered because there is an interaction between indentation cracks and the healing particles (See Figure 14). It has been observed that the main factors for having a crack going through the healing particle are the position of the particle with respect to the indentation crack and the strength of the particle-matrix interface. The self-healing reaction occurs according to the designed concept. SiO_2 is formed in the fracture surface of the particle and it flows (due to the B addition) outside the particle, filling the crack gap and reacting with the YSZ matrix to form $ZrSiO_4$ (See Figure 16). The stability of non-cracked healing particles protected by the alumina shell remains still an issue under study.

As it was mentioned, one of the important challenges in the design of extrinsic self-healing ceramics is to ensure that cracks in the composite will meet the sacrificial particles and trigger the healing reaction (See Section 1.1). In general terms, three main mechanisms can be encountered in a composite with dispersed particles: particle fracture, crack deflection due to effect of particle and interface debonding.

In this study it was found that the main factor defining the interaction between the indentation crack and a healing particle is the position of the healing particle with respect to the original indentation crack path (in a material without healing particles). The morphology of Vickers indentation cracks in ceramics is well known. In the surface four cracks are observed, originating from the four tips of the plastically deformed area. The cracks follow the direction of the indent diagonals. In depth direction the morphology is more complex as it depends on several parameters (material, load or indent geometry). Normally the fracture starts with a radial or Palmqvist-type crack emanating from the tips of the indent (with elliptical shape) and it evolves to median-type cracks upon unloading (42) (40). When particles are positioned in the preferential path of the indentation crack, it has been observed that there is particle fracture in all the cases. Several examples are shown in Figure 14 - C and D. Another important conclusion is that the crack path is partially deflected by the interaction with the healing particles. This phenomenon is especially clear in Figure 14 – D. This crack deflection has been only observed when there is particle fracture, but no crack deflection has been observed due to the effect of particles close to the preferential path of the indentation crack, despite the predictions given by Ponnusami et al. (79), in which it is concluded that the crack path may be deflected depending on the toughness and strength mismatch between particle and matrix and the presence of flaws in the healing particles. However, the experiment does show that the interface strength and the presence of interface flaws plays an important role in the type of crack-particle interaction, as concluded also by Ponnusami et al. Even if the particle is inside the preferential crack path of the indentation crack, there will be interface debonding instead of particle fracture if the interface is weak or if there are pre-existing voids in the interface. Figure 14 - A and B show two examples of crack-particle systems in which the relative position of the particle with respect to the crack path is the same. In one case the crack goes through the particle while in the other case the crack is deflected and goes through the interface. This result shows the importance of having a well-bonded flawless interface between particle and matrix for the design of the self-healing material because, even if the particle is in the direction of the crack, the crack will go preferentially through the interface if there is not a good bonding.

In this series of experiments, the dominant mechanism observed is particle fracture in the cases a particle was inside the preferential path of the indentation crack. Crack deflection to the interface was observed in few cases, and no crack deflection due to the effect of particles close to the crack path has been observed. This result is positive for the design of the YSZ-MSBA composite because it means that the self-healing mechanism will be activated in most of the cases when microcracks appear in the material. Although this experiment was performed on a fully dense material, this trend can be also extrapolated to the porous composite. The fully dense material is more conservative in terms of studying the crack-particle interaction because the crack has more potential paths for propagation than in a material with pores. If the same of higher interface strength and bonding can be achieved for the porous material manufactured by APS then it can be concluded that the crack will preferentially go through the particle when the particle is in the direction of the crack path.

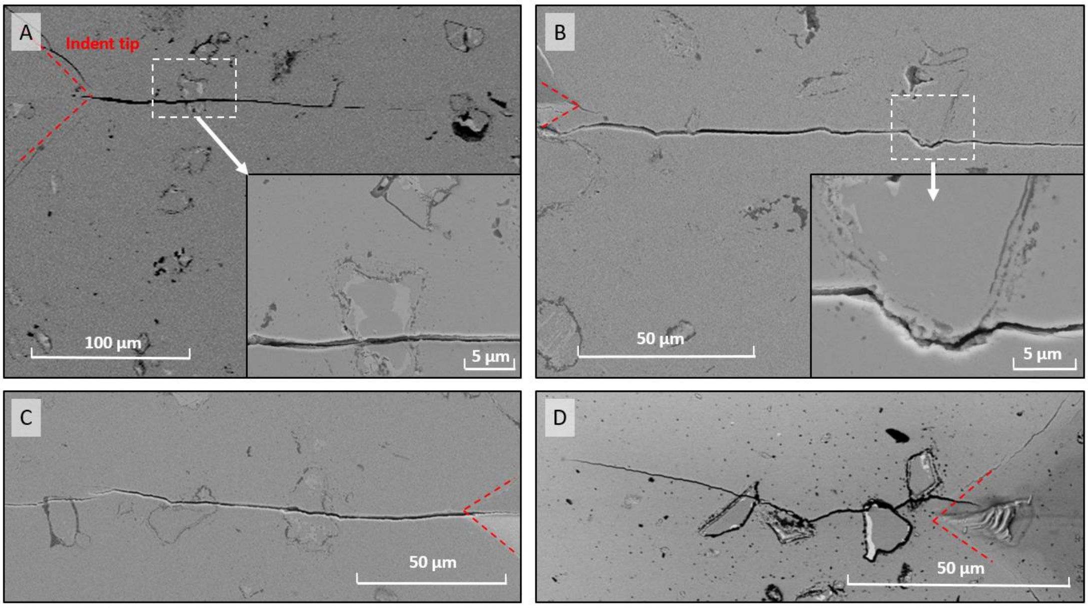

Figure 14 – Examples of crack-particle systems in the self-healing YSZ-$MoSi_2BAl$ composite

Achieving full particle fracture is important for the self-healing mechanism because the available fracture surface for oxidation is larger so a higher amount of oxidation product will be formed and, therefore, a higher portion of the crack can be filled. Even if the crack goes through the interface of a particle, it is expected to have a partial healing of the crack. In the case of crack going to the interface a smaller surface is available for oxidation. Figure 15 shows and example of a crack running through two healing particles. In one case there is full particle fracture while in the other case the crack only touches the particle in the interface with the matrix. After 1 hour healing clear differences are observed. In the case of the crack running entirely through the particle the whole crack is filled with the healing product (Figure 15 - A and C). However, in the case of a crack only touching the particle (Figure 15 - B and D) the crack is only filled in the portion close to the particle and there is still a large amount of crack that was not filled because of the insufficient available fracture surface for oxidation. Additionally, the particle shown in Figure 15 - B and D is closer to the indent tip so the crack opening is larger than for the particle shown in Figure

15 - A and C. For a healing time of 1h (healing temperature 1100 ºC), the larger crack opening leads to less amount of healing than in the particle with less initial crack opening.

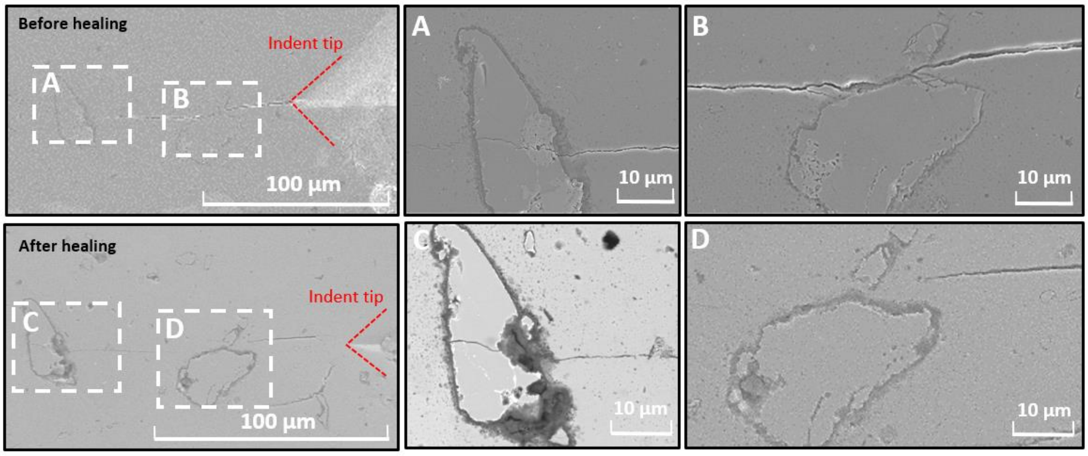

Figure 15 – Example of healed indentation crack (after 1 hour) showing several degrees of healing. The part of the crack going all through the particle shows complete healing. The part of the crack going through the interface shows only a partial healing.

A further look to the crack-particle system of Figure 15 - A and C is interesting since it can be used to validate the designed concept for the self-healing YSZ-MSBA composite. Figure 16 is a closer look to this crack-particle system. In the image, it is difficult to clearly assess the healing of cracks, so elemental mapping analysis have been performed for further proving the concept. By taking a look to detail A of Figure 16 it can be seen that the alumina shell has a similar contrast than the SiO_2 filling the part of the crack inside the particle. The same contrast can be observed inside the crack of detail B, so this suggests that the crack is filled with SiO_2. This means that one hour is not enough time for healing a crack of around 200 nm. Although it is difficult to appreciate in the image, in detail M2 there is a part of the crack with a narrower crack opening than the rest. In this portion of the crack the contrast observed in the backscattered electron image is different than the SiO_2 contrast. It shows a lighter grey contrast. This evidence suggests that $ZrSiO_4$ was already formed in the narrower section of the crack after one hour of healing.

Further evidences proving that the healing concept works as designed are provided with the elemental analysis maps. Detail M1 shows a closer look to the part of the crack inside the particle, which is the place where the healing reaction starts. By looking at the X-ray maps of oxygen and silicon it can be seen clearly that the crack is filled with SiO_2 and there is no zircon forming inside the particle. The complex multi-layered structure of the shell can be also seen in this spectral image. In direct contact with the $MoSi_2$ there is a thin layer of Mo_5Si_3 (more Mo counts and less Si counts as compared with the $MoSi_2$ area); then, a clear layer of Al_2O_3, which looks intact after the high temperature oxidation in air; and last layer is a mixed alumina-YSZ area.

Details M2 and M3 are two closer looks to the indentation crack after healing for one hour. Spectral image M2 shows an interesting result. There is also Al_2O_3 filling part of the crack, together with SiO_2. Probably this is due to the presence of some aluminium left in solid solution inside the healing particles or also due to partial decomposition of the alumina shell in the interface between particle and matrix. This behaviour has been also observed in other crack-particle systems after healing. As it was mentioned before, in the narrower part of the crack some $ZrSiO_4$ is formed. By looking to the central part of the crack in between the two alumina spots in detail M2, it can be observed the presence of some Si and

Zr. This suggests the existence of zircon which is the final desired healing product. In detail M3 the amount of alumina filling the crack is much lower as compared with the amount of silica. The presence of a small void can be confirmed by looking at the spectral images of all elements that do not show any filling product.

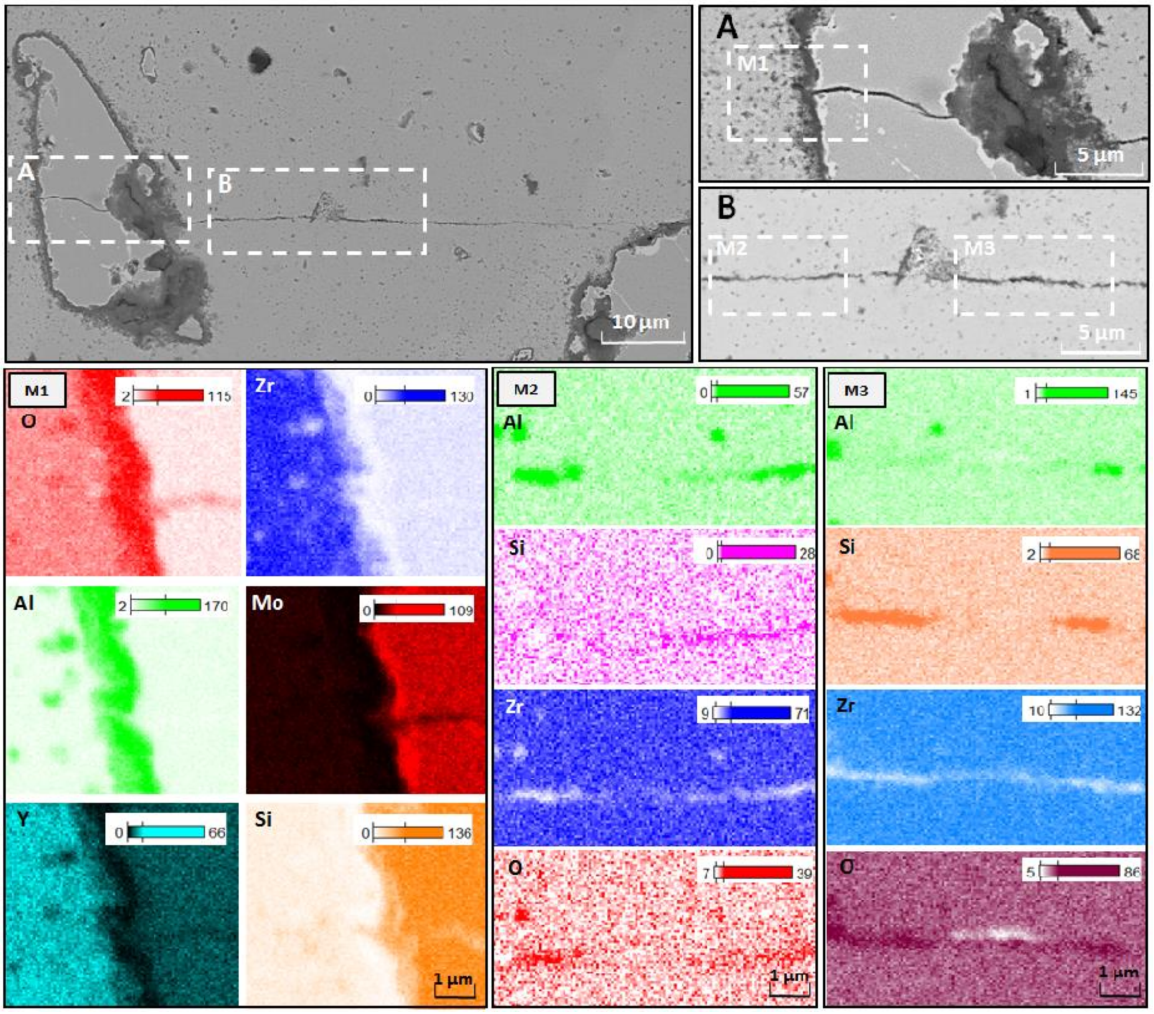

Figure 16 – Healing of an indentation crack after 1h exposure in air. Several compounds can be seen from the different contrasts in the BEI image of the after healing crack-particle system. The EDS spectral maps further prove the concept.

Coming back to the requirements for healing in the YSZ-MSBA composite (See Section 1.1), these experiments showed that the healing mechanism can successfully be triggered because of the sufficient interface strength of most of the particles and the healing reaction is developed according to the design. First the amorphous silica is formed in the fracture surface of the particle and it flows outside the particle. The amorphous silica reacts with the matrix to form the final healing product, $ZrSiO_4$. Although not predicted by design, it was also observed the formation of some alumina spots along the crack path. This is attributed to the presence of aluminium left in solid solution inside the particle after the annealing treatment.

4.2. Mechanical characterization of the material: Elastic modulus and hardness

In this chapter, the results of the determination of elastic modulus and hardness of the YSZ-MSBA composite are presented. In Section 4.1.1 three models for the elastic modulus are presented. One model for predicting the elastic modulus of the material as a function of porosity volume fraction in the matrix. A second model for predicting the Young's modulus of the healing particles as a function of aluminium addition and also taking into account the boron addition. The third model is a classical rule of mixtures that uses the input of the two previous model for predicting the elastic modulus of the composite as a function of volume fraction of healing particles. In Section 4.1.2 a similar set of results is presented for predicting hardness of the material, although in this case no rule of mixtures is presented because there are no standard procedures for predicting hardness of particulate composites from the hardness values of its constituents. Finally, in Section 4.1.3 the results of Indentation Fracture Toughness experiments are shown. The value presented in this last section can be considered a first approximation to the fracture toughness of the composite material and, therefore, it can be used as an input for the finite elements-based simulations for determination of strength and fracture toughness of the material from the BD and WL-DCB test set-ups.

All the results presented in this chapter have been obtained from depth-sensing indentation technique and the application of models for extraction of properties (See Section 2.2.1, 2 and 3). The complete set of results for the microindentation and nanoindentation testing can be found in Appendix 4.1 and 4.2. In the case of nanoindentation, the elastic modulus and hardness as a function of penetration displacement for each of the tested specimens is shown. The first region of the curve, for low penetration displacements, that shows a sharp increase of hardness and Young's modulus is normally related to the transition from a purely elastic contact to a elasto-plastic contact (80). The value that should be trusted is the one for the higher penetration displacements. In the case of microindentation experiments, the load-dependency of elastic modulus and hardness was studied. It was found out that the accuracy of the displacement sensor is poor for loads below 50 N, therefore only values above this limit were used for determination of elastic modulus and hardness. For Vickers Indentation the values between 10-50 N can be trusted because the hardness result only depends on the optical observation and not on the displacement sensor of the machine.

4.2.1 Characterization of elastic modulus

YSZ has a relatively low elastic modulus, around 210 GPa (81), as compared with other ceramic materials that normally exhibit values above 300 GPa. This is one of the reasons why it is used as thermal barrier coating, because its lower elastic modulus minimizes the thermal stresses due to CTE mismatch between the different layers of the coating system. On the other hand, $MoSi_2$ has a much higher elastic modulus, around 440 GPa (82) (83) (76) for single crystals. Therefore, according to the common rules of mixtures used for particle-dispersed composites, the Young's modulus of the monolithic composite will be higher than pure YSZ, so higher than the current TBC system. This is a detrimental effect in terms of thermal stresses.

The effect of porosity in the elastic modulus of the zirconia matrix was first studied. It was found out that an exponential law is the best fit for the experimental results. Since YSZ is a well-known commercial material there is a large amount of reference data for comparison. The comparison of the experimental results from indentation with NIST-trusted references (81) shows good agreement. Therefore, from this model and the typical porosity values of

TBC system a good prediction for the elastic modulus of the TBC system without considering the influence of healing particles is 125-160 GPa (See Figure 17). As a second step, the elastic modulus of monolithic MSBA was studied in order to have a prediction of the elastic modulus of the healing particles material. The main finding is the decrease of elastic modulus due to the Al addition. This is attributed to the phase change from tetragonal to hexagonal structure and to the further substitutional solid solution of Si by Al in the hexagonal phase. The effect of borides present in the microstructure is less clear, although their influence is negligible as their volume fraction is below 10%. For the alloy only containing boron the experimental elastic modulus was much below the reported value in literature for single crystal $MoSi_2$. This was attributed to the effect of SiO_2 impurities (with a very low elastic modulus), as it has been noticed also by other authors (76). However, it is expected the elastic modulus of tetragonal healing particles to be close to the reported value for single crystal.

By using the two predicted elastic modulus from matrix and healing particles it is possible to build a rule of mixture for predicting the elastic modulus of the composite. Only experimental data for 10 vol.% healing particles was used to validate the rule of mixtures and it shows good agreement, although more validation data is needed for having a more reliable model.

Regarding the model for predicting the effect of porosity in the elastic modulus of the YSZ matrix, among all the models presented in Section 2.1.2 only three were selected for fitting the experimental data because these are the most commonly used. In Figure 17 the results and experimental fittings of the porosity effect in the elastic modulus of YSZ are shown.

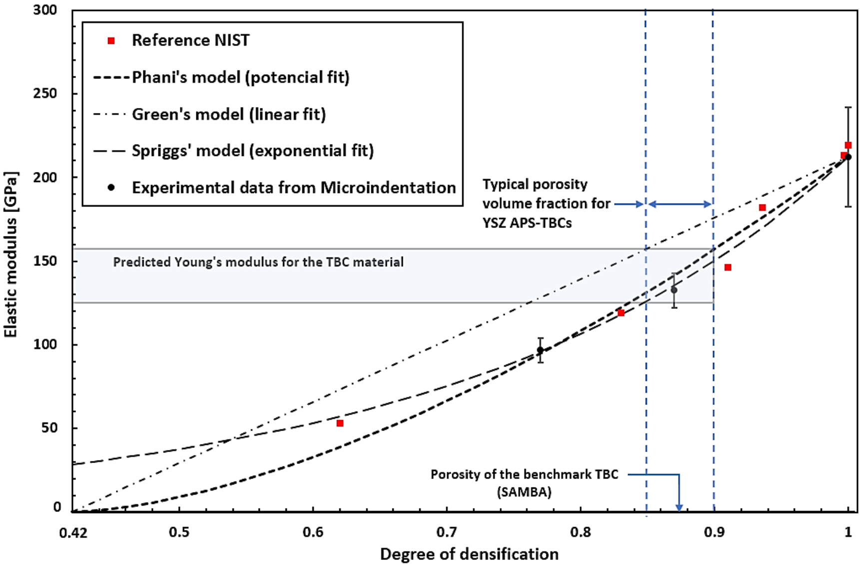

Figure 17 – Effect of porosity in the elastic modulus of YSZ

The experimental results have been compared with NIST-trusted references and it shows good agreement with the data (81). For porosity volume fractions lower than 0.2 the exponential and potential fittings are very similar. However, for higher porosities both models diverge. The linear model is only valid for very high densifications (>0.98). Both the linear and potential model have been normalized with the Green density, that is 0.42 for YSZ. Since the exponential fit is closer to the experimental data, this is the model that will be used for predicting the Young's modulus of the matrix:

$$E = 212\, e^{-3.46(1-D)}$$

where D is the degree of densification of the YSZ matrix.

It is important to mention that the experimental results for fully dense YSZ and porous YSZ are from materials with different characteristics. The material of the fully dense YSZ specimens is Tosoh and the material for the porous samples is Amperit (See Section 3.1). The grain size does not have an influence on the elastic modulus since this is an intrinsic property of a material. However, the effect of yttria addition must be taken into account because it may change the nature of the bond in the material and affect the macroscopic Young's modulus. Other authors studied the effect of yttria additions in the elastic modulus of zirconia and found out that there is not a significant difference (84) (85). Therefore, it is valid to use materials with different yttria contents for this study.

Regarding the high scatter in the experimental data for the fully dense specimens, several explanations are possible. Errors from the indentation measurement is one possibility. Also it was considered that the reduction of zirconia (loss of oxygen) during powder sintering might have an effect in the Young's modulus, as it has been suggested by other authors (86). In any case, the scatter range of the experimental data for the fully dense specimens is within acceptable limits as compared with other results found by other authors. Especially interesting is the paper of Ingel and Lewis. They measured the elastic constants for YSZ single crystal with different yttria contents and then they gave an estimation for the macroscopic Young's modulus based on computing the Voigt-Reuss and Hashin-Shtrikman bounds from the elastic constants of the single crystal. According to their results, the Voigt-Reuss bounds are at 250 GPa and 190 GPa, respectively. Therefore, this gives an idea of the area of validity for measured Young's moduli of YSZ. The measured Young's moduli by indentation in this study are within these bounds; hence, the results can be considered valid.

In Figure 17 an estimation for the elastic modulus of the TBC has been also included. Typical porosity volume fractions for TBC manufactured by APS are in the range of 10-15% (69). Therefore, the estimated elastic modulus according to the experimental exponential law is 125-160 GPa.

The second study performed is the analysis of the influence of B and Al addition in the elastic modulus of $MoSi_2$. It was found out that the addition of Al in substitution of Si decreases the elastic modulus in the case of the 6 wt%Al and the 12 wt%Al containing alloys. Besides, it was observed that the elastic modulus of the 12 wt%Al containing alloy is even lower than the 6 wt% Al alloy. The same trend has been reported by other authors (72) (73) (87) (88). This change in elastic modulus is caused by the phase change from tetragonal to hexagonal induced by the Al addition (See Section 4.1.1). Other authors have also related the change in elastic modulus with the phase change of $MoSi_2$, however no explanations can be found in literature about the further decrease of elastic modulus for fully hexagonal $MoSi_2$ when adding more Al, as it can be observed in the results of indentation testing shown in Figure 18.

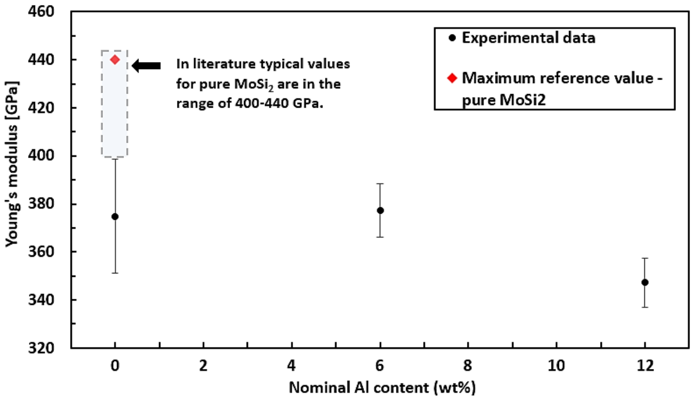

Figure 18 – Effect of alloying $MoSi_2$ with Al and B in the Young's modulus of the material

As it is observed in Figure 18, the elastic modulus decreases from 380 GPa for the 6wt%Al containing alloy to 350 GPa for the 12 wt%Al containing alloy. The most likely explanation for this phenomenon is the influence of the substitutional solid solution of Al in the $MoSi_2$ hexagonal structure. The substitution of Si by Al changes the nature of the atomic bonds in the structure so probably this is related to the change in the elastic modulus. However, there is no literature that backs up this reasoning, although experimental results from other authors also show the further decrease of elastic modulus by adding more Al to fully hexagonal $MoSi_2$.

The reason for the lower elastic modulus in the hexagonal $MoSi_2$ is well reported in literature. Y. Qiao et al. studied the differences of elastic modulus by means of first principle investigations According to their work, the Young's modulus along the [1 0 0] and [0 1 0] direction for the tetragonal and the hexagonal structures is almost similar and the difference is on the modulus along the [0 0 1] direction that is around 100 GPa higher for the tetragonal lattice. This is due to a stronger interaction between the Mo and Si atoms in the [0 0 1] direction for the tetragonal lattice (89).

Regarding the effect of boron addition, no clear influence has been found as the boron concentration is constant for all the alloys. The formation borides have been explained in 4.1.1, but it is difficult to assess their influence in the elastic modulus because there is no literature regarding the elastic modulus of molybdenum borides.

Another interesting finding in this study is the unexpectedly low Young's modulus for the elastic modulus of the alloy only containing boron (0 wt% Al). A Young's modulus of 375 GPa results from the indentation experiments. According to the previous explanations, the elastic modulus of this alloy should be higher than the one for the 6 wt%Al and 12 wt%Al containing alloys because the material is fully tetragonal. A Young's modulus close to 440 GPa was expected for the alloy only containing boron. However, 440 GPa is the value for single crystal and without impurities. In this study polycrystalline $MoSi_2B$ was manufactured and a substantial amount of SiO_2 impurities were found. SiO_2 has a very low elastic modulus compared with $MoSi_2$ (could be regarded as a void); hence its presence decreases the Young's modulus of the polycrystalline material. This effect has been also reported by other authors (76). On the other hand, the Al containing alloys do not form SiO_2 since Al_2O_3 is preferentially formed. The elastic modulus of alumina is close to the one of tetragonal $MoSi_2$, so no significant influence is expected from the Al_2O_3 impurities. Although it is not addressed here, the presence of SiO_2 in the alloy only containing boron also decreases the strength of the material.

The healing particles size is in the order of magnitude of the grains so it is expected the Young's modulus of the particles with the Al fully depleted in the interface to be close to the reported Young's modulus for tetragonal $MoSi_2$ single crystals, 440 GPa. However, for the composites in which the in-situ encapsulation process has not been performed yet, assuming fully hexagonal structure in all the particles, the recommended Young's modulus for modeling purposes is 375 GPa for the 6 wt%Al containing particles and 350 GPa for the 12 wt%Al containing particles.

Finally, with the inputs from the two previous studies a rule of mixtures is stablished (from equations 10 and 11) that gives an estimation of the Young's modulus of the YSZ-MSBA composite. An elastic modulus of 230 GPa is predicted for fully dense composites with tetragonal-$MoSi_2$ healing particles, so after complete depletion of Al to the interface. A Young's modulus of 226 and 224 GPa is predicted for the composites with hexagonal-$MoSi_2$ healing particles containing 6 and 12 wt%Al, respectively. Composites in which the Al has not been depleted yet to the interface will have hexagonal-$MoSi_2$ healing particles. Experimental values have been used for validating the rule of mixtures, but only for 10 vol.% addition of particles and composites with 6wt%Al containing healing particles. More data would be necessary to have a complete validation. In Figure 19 the rule of mixture for a composite containing 6 wt%Al healing particles (with sol-gel pre-encapsulation) is shown.

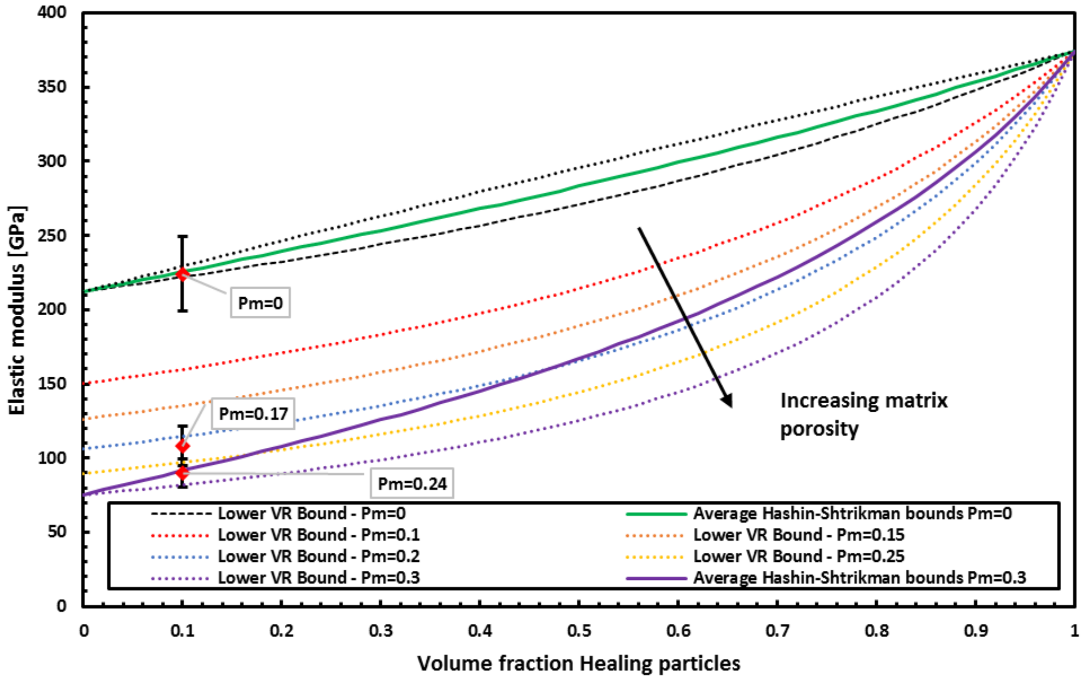

Figure 19 - Rule of mixtures for predicting the elastic modulus of the YSZ-MSBA composite.

This rule of mixture has been used for representation because the composites tested for validation of the model are 2wt%B-6wt%Al containing composites and no heat treatment for Al depletion was applied. The experimental data for fully dense material fits the model, and more deviation is observed for the porous composite. This is normal considering that the measurement of porosity volume fraction in the composites contains certain standard deviation. It can be also observed that for lower degrees of densification of the matrix there is a higher separation between the average of the Hashin-Shtrikman bounds and the Voigt-Reuss bounds.

4.2.2 Characterization of hardness

The results of previous section demonstrate that $MoSi_2$ is a stiffer material compared to the YSZ matrix; hence the overall Young's modulus of the composite is slightly increased (for an addition of 10 vol.% healing particles) as compared with the commercial YSZ used for TBC systems. In the case of hardness, comparing YSZ and $MoSi_2$ is more difficult because this property is microstructure dependent. Parameters like grain size, presence of impurities, second phases or work of hardening affect the hardness value. In the case of the materials studied in this project, YSZ (200-400 nm average grain size) is generally harder than $MoSi_2$ (20-30 µm average grain size) because the grain size of Tosoh-YSZ is much smaller than the grain size of healing particles. Although a complete comparison of hardness values is complicated due to the microstructure-dependency, just assuming the influence of grain size, a typical value for YSZ (200-400 nm average grain size) is around 15 GPa (90) and for $MoSi_2$ (20-30 µm average grain size) is in the range of 9-10.5 GPa (91) (75) (92). However, for nanosized $MoSi_2$ (similar grain size than YSZ) some authors have found a hardness value close to the one of zirconia, around 14 GPa (76).

In Figure 20 the results of this study are shown. The effect of porosity in the hardness of the YSZ matrix is shown in the left plot and the influence of boron and aluminium addition in the hardness of $MoSi_2$ is shown in the right plot.

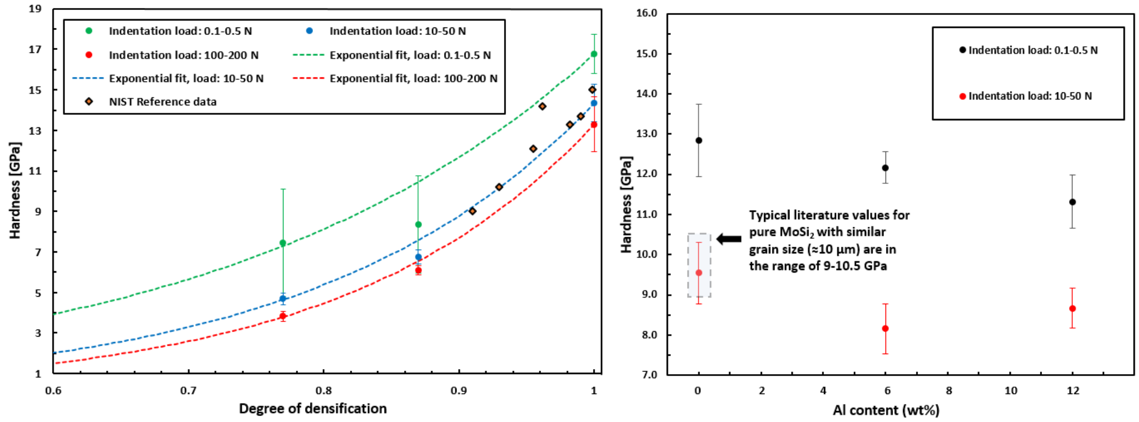

Figure 20 – Effect of porosity in hardness of yttria-stabilized zirconia (left) and effect of aluminum and boron addition in the hardness of $MoSi_2$

A first important observation, common for both plots, is the influence of indentation load/size in the hardness results. A significant difference is noticed between the results of nanoindentation (load 0.1-0.5 N) and microindentation (10-50 N and 100-200 N). Although the difference is less significant, there is also a size effect between the hardness values for 10-50 N (used for Vickers Hardness) and the hardness values for high loads 100-200 N (used for elastic modulus and fracture toughness determination). This effect has been reported by many authors and modelling of size effect has been also subject of numerous research (93) (94) (95). For study of the porosity effect and composition of healing particles, the same load ranges have been used in order to neglect the size effect.

The results of the left plot of Figure 20 show the effect of porosity in the hardness of the YSZ matrix. Hardness decreases for lower degrees of densification and the best fit of the experimental data is an exponential law in all the cases. The experimental results from nanoindentation (0.1-0.5 N) in the porous specimens exhibit high scatter, most probably due to the fact that the indentation size is in the same order of magnitude than the pores size. Therefore, for this study it is better to rely on the microindentation data. Nevertheless, the scatter range for the fully dense specimens is acceptable both for nanoindentation and microindentation. The same trend showing a decreasing hardness with increasing porosity has been also obtained by other authors. A good example in the work of Cottom and Mayo (90). Their values of hardness for YSZ as a function of porosity are recommended by NIST as reference values for this material. These reference values have been represented in the left plot of Figure 20 and it shows good agreement with the experimental data for medium loads (10-50 N) and similar grain size. The reason for the decreasing hardness for increasing porosity has been also subject of research. Indentation is a process governed by the elasto-plastic deformation of dense material. However, in porous material there is an important additional effect which is the increased densification (porosity filling) of the material beneath the indenter due to the very high contact stresses. This densification of the material beneath the indenter leads to lower elastic recovery of the indent so the resultant imprint is bigger than for the fully dense material (81) (96).

Regarding the effect of boron and aluminium additions in $MoSi_2$, the results shown in the right plot of Figure 20 show a decreasing hardness value in the transition from tetragonal to hexagonal structure of $MoSi_2$ induced by the Al addition, that confirms the results of other authors (74) (89). In other words, alloying $MoSi_2$ with Al makes the material more ductile at room temperature. This is due to the easier [1 0 0] (0 1 0) and [1 0 0] (0 0 1) shear deformations of the hexagonal structure as compared with the tetragonal lattice (89). As in the case of the elastic modulus, there is not clear explanation for the influence of boron in the alloy because all the alloys contain the same amount of boron and there is not much literature about mechanical properties of molybdenum borides.

A size effect is also observed in the experimental results for the $MoSi_2BAl$ alloys. It is interesting to notice the difference between the trends of nanoindentation data (0.1-0.5 N) and microindentation (10-50 N). Looking at the results for medium loads, it can be seen that the hardness for both alloys containing Al is lower than the tetragonal-$MoSi_2B$, which is in accordance with the previous explanation. Furthermore, the 12 wt%Al containing alloy exhibits higher hardness values as compared with the 6 wt%Al containing alloy, while in the nanoindentation data the hardness decreases for higher Al content in the alloy. The most likely explanation for this phenomenon is the presence of impurities and second phases in the microstructure that affect the hardness results for medium loads. According to the literature, the correct trend is the one shown by the nanoindentation data. Hardness decreases for increasing Al content, as it is shown by Liu et al. in their first-principle investigations (73). Their results show that the elastic constants C44 and C66, which are directly related to hardness, decrease when adding Al as compared with pure $MoSi_2$ and then they show that by further addition of Al C44 and C66 keep decreasing. Therefore, the microindentation data for medium loads is the one that does not obey the expected trend. The most possible explanation for this is the effect of impurities and second phases. It is well-known that the presence of SiO_2 is detrimental for the mechanical properties of $MoSi_2$ since is lowers the strength (75), thus another positive effect of the Al addition is the preferential formation of Al_2O_3 instead of amorphous SiO_2. Also the amorphous silica lowers the hardness; hence in the Al containing alloys the hardness is increased due to the alumina formation. However, this mechanism competes with the softening due to the transition from tetragonal to hexagonal. It may happen that in the case of the 6 wt%Al containing alloy the effect of softening due to the phase change is much stronger than the effect of alumina precipitates, but in the 12 wt%Al containing alloy the effect of alumina dispersion increases with respect to the 6 wt%Al containing alloy, so this results in a higher hardness. By looking at the microstructure of both alloys in Figure 9 a finer grain dispersion of alumina is observed in the 12 wt%Al containing alloy so this could be another reason for the higher hardness. Also the molybdenum borides could play a role in the higher hardness.

As it was mentioned before, there are no rules of mixture for hardness of composites because it is a property strongly depending on the microstructures. Anyhow, just as a final result, the general trend that has been observed is a lower hardness in the composite specimens, both for the fully dense and the porous material. For fully dense composites a hardness value of 13.1 ± 1.8 GPa has been obtained.

4.2.3 Indentation fracture toughness

As it was stated at the beginning, the main objective of this chapter is to characterize hardness and elastic modulus of the YSZ-MSBA composite. However, since indentation has been used as experimental tool, also the Indentation Fracture Toughness (IFT) method can be used for giving a first approximation of the fracture toughness of the composite. The method could be applied successfully only to the pure YSZ specimens. For the composite specimens a majority of undesired lateral cracks are formed after unloading. In the case of the monolithic $MoSi_2BAl$ specimens there are many cracks emanating from the indent edges, but there are not four preferential cracks following the indent diagonals direction. In the case of the pure YSZ fully dense specimens the majority of indentation cracks are the four typical cracks emanating from the indentation imprint tips and following the direction of the indent diagonals. Therefore, the Indentation Fracture Toughness method can be applied for the pure YSZ and give an estimation of the fracture toughness.

In Figure 21 the IFT results for pure YSZ are shown. In the left plot the indentation (surface) crack length and the crack-indent diagonal ratio versus indentation load is presented and it helps to determine the morphology of the indentation cracks in YSZ and the suitable IFT model. Besides, two representative pictures of an indentation before and after polishing are shown in order to have a more complete understanding of the phenomenon. As it can be seen in the left plot, the l/a for all the load cases is within the range of validity of models of Palmqvist type cracks. This suggests that the crack geometry, even for the highest load, is of Palmqvist-type. According to Niihara et al., median-type cracks normally exhibit a well-develop surface crack in which the c/a (l/a + 1) ratio is normally above 3 (46). This is one evidence for confirming the formation of Palmqvist cracks in YSZ (even for high loads), but also further evidence is provided with the picture of an indentation spot before and after polishing of the surface. It can be seen clearly that the indent tip of the polished surface does not touch the crack tip. This means that the crack has the typical semi-elliptical shape of the Palmqvist-type crack. In the polish surface of an indentation with median-type crack normally it can be seen that the crack tip touches the indent tip and when the indent is totally erased there is still remaining crack. In this case, although it is not shown here, after polishing and totally erasing the indents there was no crack beneath the indent. Besides, other authors have also demonstrated that the morphology of indentation cracks in YSZ is Palmqvist-type (43) (44). Only for very high indentation loads (much above the loads used in this study) there is a transition from Palmqvist-type to kidney-type and finally to median cracks (45).

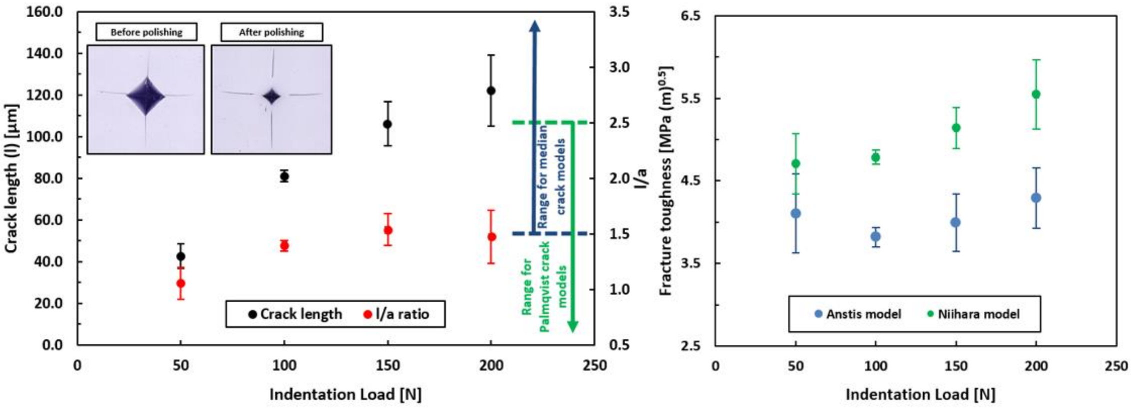

Figure 21 – Indentation Fracture Toughness of pure YSZ (right) and crack length as a function of load (left) of the indentation cracks used for estimating IFT of pure YSZ.

In the right plot of Figure 21 the IFT as a function of indentation load is plotted. Two models have been used for the calculation, as it is explained in Section 2.2.3. Anstis model is one of the most used models for materials exhibiting median-type cracks, which is basically a modification of the model based on dimensional analysis proposed by Evans and Charles (47). As explained in Section 2.2.3, Niihara made Evans' approach more general by introducing a modification in the model that included low crack-to-indent diagonal (c/a) ratios, which is the typical case in indentations exhibiting Palmqvist-type cracks, so the second used model is Niihara's. As it has been explained in the previous paragraph, the evidences from optical observation suggest that Palmqvist cracks are formed for the whole load range, and this is supported by literature; hence Niihara's model should provide the most accurate prediction for the fracture toughness of YSZ. However, also Anstis model for median cracks has been used for comparison. The result shows a higher fracture toughness in the case of Niihara's model. Averaging for the whole load range a value of 5 ± 0.5 MPa$\sqrt{m}$ is obtained applying Niihara's model, which is close to other reported IFT values for YSZ (44) (45).

4.3. Strength and fracture testing

In this chapter the results of the strength and fracture test performed on the WL-DCB and BD specimens are presented and discussed. The objectives of these two novel mechanical testing set-ups are to accurately determine the strength and fracture toughness (fracture energy) of the self-healing composite material and quantify the recovery of load bearing capability due to the activation of its the self-healing capability. Each test has its own particularities. For the WL-DCB test it is expected to create slow-growing and controlled cracks of short length (< 10 mm). The aim is to accurately determine the fracture toughness (fracture energy) of the material. For the BD test it is expected to create a controlled fast-growing crack of large length (10-20 mm), but that does not result in a fully fractured specimen. The BD set-up aims for an accurate determination of strength. In both cases the most important achievement of the test is to successfully arrest a crack in the brittle material in order to heal it and assess the recovery of load bearing capability.

The initial state of the material and the specimens prior to test is studied in a first section. Then, the results of fracture testing and determination of material properties are presented.

4.3.1 Specimens analysis prior to test

As the strength strongly depends on the flaw distribution in brittle materials (See Section 2.1.5), the analysis of surface quality in the test samples is important. In Section 3.4.3 the machining process used for the test specimens was described and it was explained the type of defects that these type of heavy machining processes introduces in the material. In this section the surface finishing of the WL-DCB and BD specimens is shown, focusing only on the most stressed area of the specimen, where it is expected that brittle fracture will start. In Figure 22 the typical surface condition of WL-DCB specimens in the most stressed area is shown. The most stressed area in the wedge specimen is the tip of the chevron notch. A first important observation from the SEM images is the clear difference in the chevron notch tip geometry between the design and the real produced specimens. According to the design, the tip of the chevron notch should be straight and not curved as it can be seen in Figure 22. This is most likely a limitation of the machining tool. The other important observation from these results is the difference in the surface finish between the specimens manufactured with Tosoh powders (left) and Amperit powders (right). The surface of the samples manufactured with Amperit powders is clearly rougher, as it was expected, because the grain size of this material is 10-20 times bigger than the material manufactured with Tosoh powders. The rougher surface is related to a higher amount of chipping from the removal of material. The chipping size is around the size of the grains (around 10 µm). Chipping is also observed in the surface of the specimens manufactured with Tosoh powders, but the amount and size is smaller.

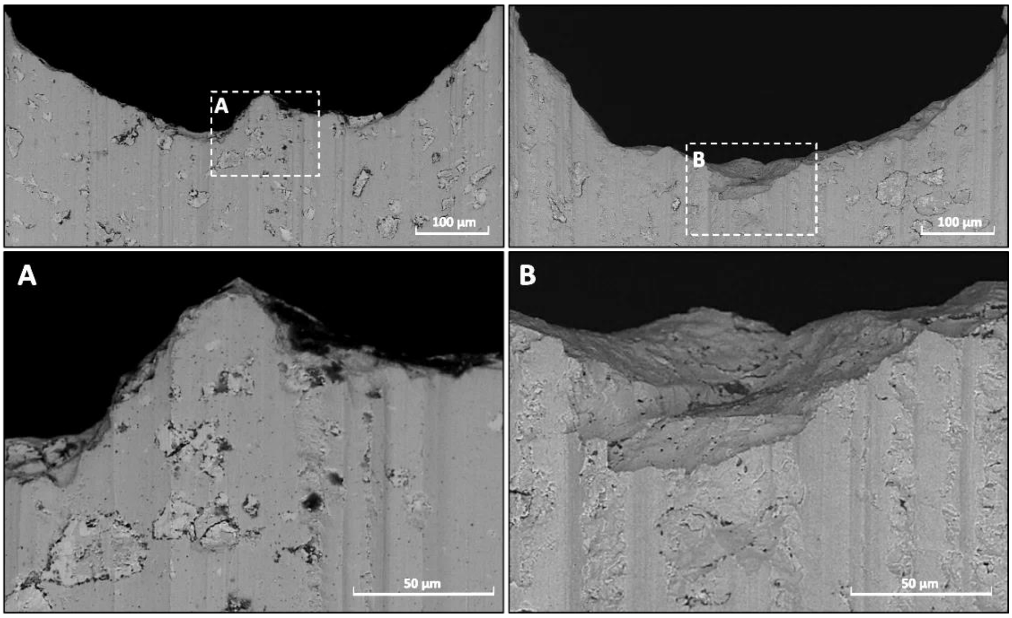

Figure 22 – Initial surface condition in the most stressed area of the WL-DCB specimen

Similar surface finishing can be found in the BD specimens. The area of maximum tensile stress in the Brazilian Discs is at the central hole of the specimen, at the bottom of the diametral groove. In Figure 23 the typical surface condition of the BD specimens is shown. Again, a clear difference between the samples manufactured with Tosoh powders (left) and the samples made with Amperit powders (right) is observed. In both cases there is chipping due to material removal during machining and the concentration per unit of area is much higher in the case of the samples manufactured with Amperit powders. Also the straight machining lines are clearly visible, suggesting that the tool used is a circular diamond blade (and not spherical tool) for machining of the BD disc grooves. The size and morphologies of the chippings in the case of Amperit specimens is the same as observed for the Amperit WL-DCB specimens. The size of the chipping is about 10 µm, corresponding with the grain size of the material.

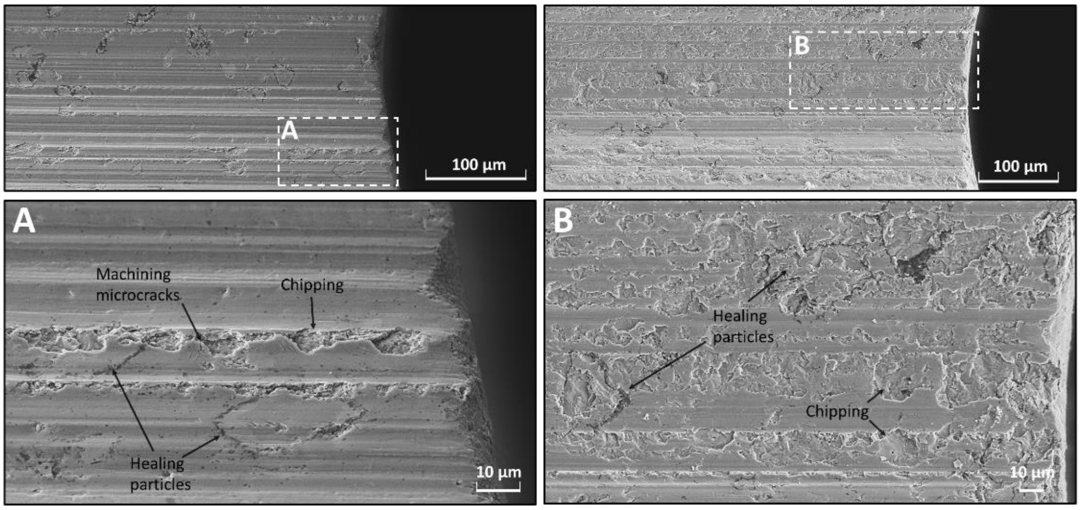

Figure 23 - Surface condition in the most stressed area of the BD specimen

The microstructure of the WL-DCB and BD specimens has been also studied. The focus of the microstructural analysis of the cross-sections of the WL-DCB and BD samples is to determine the quality of the healing particles and the encapsulation approach. In Figure 24 the typical microstructure in three different depth-levels (thickness direction) is shown. Clear differences are observed in the different spots along the thickness direction; hence the microstructure is not homogeneous.

The top left image of Figure 24 shows the microstructure of the material close to one of the surfaces of the sample. Often the alumina shell around the particles is not fully complete, so the healing particles are not entirely protected. Also a very thick layer of Mo_5Si_3 is observed, which is not in accordance with the cross-section images of the material sintered at 1200 ºC shown in Section 4.1.2. A very interesting feature, also not observed in the microstructure of the specimens manufactured at 1200 ºC, is the one shown in Figure 24-B. It looks like cracks appeared in the matrix surrounding the healing particles which are poorly protected by the alumina shell. This feature has been observed in other particles close to the surface and not fully encapsulated by the Al_2O_3 layer. There are some cases of fully encapsulated particles close to the surface and in those cases no cracks in the matrix surrounding the particles were observed. EPMA of these areas of abnormal morphology suggests that the reason is the destabilization of the YSZ matrix due to loss of yttria. Subsequently this may cause phase transformation from tetragonal into monoclinic, associated with a volume expansion of around 5%. This volume expansion is the one that could induce the fracture of the matrix around the particles. Apparently, a reaction occurs between an element of the healing particles and yttrium. Therefore, these not-protected particles will potentially oxidize when exposing the material at high temperature and oxidizing atmosphere.

The left middle picture of Figure 24 has been taken from the volume of the material near to the core (half thickness). In this case the microstructure is quite similar to the one shown in Figure 13 for the composites sintered at 1200 ºC. The majority of particles are fully encapsulated and the feature shown in Figure 24-B has not been observed.

The left lower picture of Figure 24 is from a spot of the microstructure close to the opposite surface of the sample. At this side a lower degree of densification of the matrix is observed, which suggests a pressure and temperature gradient during sintering of the powders in the SPS.

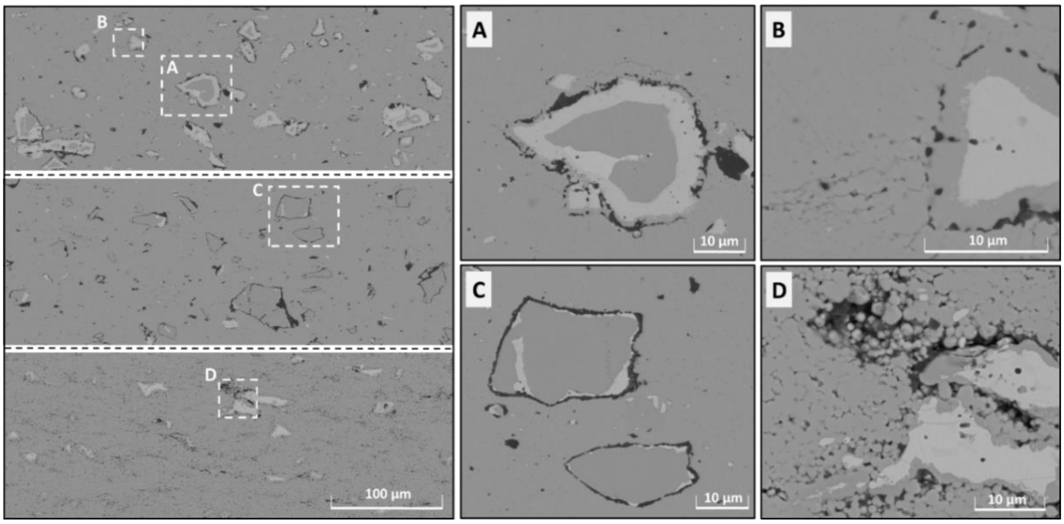

Figure 24 – Microstructure along thickness direction in the cross-section of BD and WL-DCB specimens

The results presented in this section regarding the microstructural and surface analysis of the WL-DCB and BD specimens shows several points for improvement in the material and sample manufacturing for future developments.

4.3.2 Fracture test results and determination of material properties

4.3.2.1 Brazilian Disc (BD) test

The BD test is one of the methods used for quantification of the recovery of load bearing capability in the YSZ-MSBA composite. The test results, combined with analytical and numerical calculations, can be used for extracting mechanical properties. The BD method is especially designed for obtaining the strength of the material. It is expected that this value will be mostly influenced by the shape of the stress concentration grooves and holes and by the surface defects created by the heavy machining process (See Section 3.4.3). As explained before (See Section 2.2.4), the stress concentration elements are necessary for promoting a preferential path for the crack and for controlling its extension. Another advantage of including these stress concentration elements, from the point of view of quantifying the healing efficiency of the material, is that the strength (maximum load bearing capability) will be mainly determined by the geometry of these elements and the surface condition after machining. If the same geometry and surface conditions can be reproduced in all the specimens, then the deviation of strength should not be very large from one specimen to another, which is an advantage for the quantification of healing efficiency.

The load-displacement curves for the tested YSZ-MSBA composites are presented in Figure 25. The load is represented as a function of the displacement measured by the extensometer attached to the loading jigs. This is especially important in the BD test because high loads are reached and the difference between the direct displacement measured by the bench of the loading frame and the extensometer becomes larger, leading to high discrepancies with the numerical models (See Section 3.6.2.1). In all the cases the specimens were preloaded up to 3000 N for pre-deforming the Ni plate placed in between the specimen and the loading jigs and accommodate the sample. The load-displacement curves for all the specimens are very similar up to 3000 N. In this region the displacement is mainly determined by the elastic deformation of the material and the Ni plate because all the plastic deformation already occurred during pre-loading. The Young's modulus of all the composites is the same so it makes sense that all the specimens exhibit the same displacement up to around 3000 N.

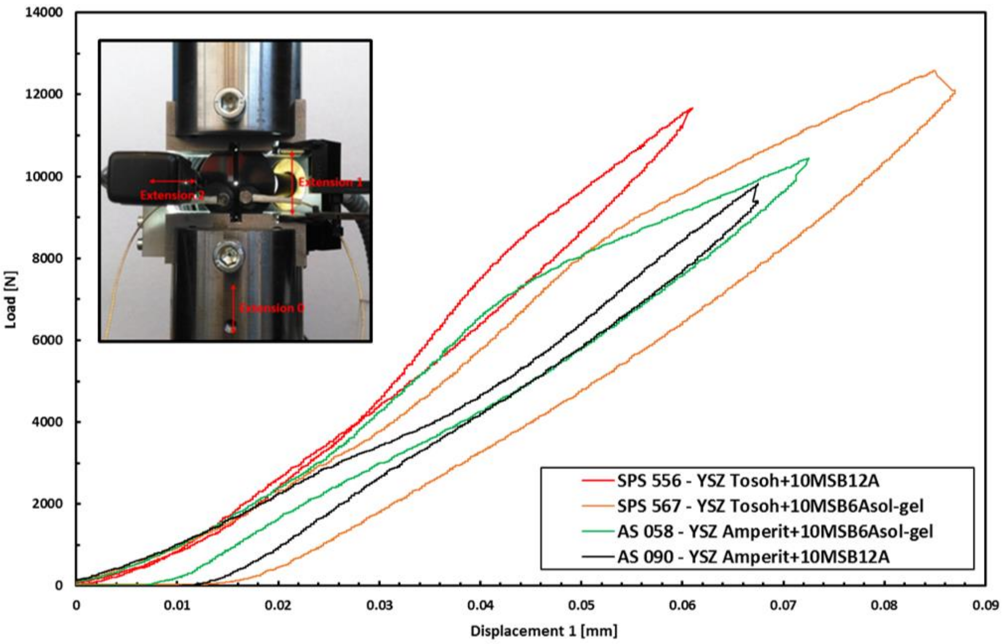

Figure 25 – Load and displacement measured in the fracture test of the BD specimens

Above 3000 N the load-displacement curve of each material is different, there is a change in slope. This is, most probably, due to the plastic deformation of the Ni plate that is slightly different for each specimen (due to geometry differences in the micro-level in the contact between the sample and the loading jig); hence the different loading path for each sample. Additionally, elastic deformation of the specimen and the Ni plate contribute to the displacement output obtained from the test.

The deformation of the Ni plate is certainly very important for understanding the displacement measurement from the test set-up and for the FE simulations of the BD set-up. The initial thickness of the annealed Ni plates is 0.25 mm (See Section 3.6.2.2.2) and, as it can be seen in Figure 25, the maximum displacement for all the samples does not reach 0.1 mm, around 2 times lower than the thickness of the Ni plates. Therefore, the plastic deformation of these plates has a significant influence on the displacement and must be completely understood for matching these results with numerical simulations.

Another interesting observation from the results of Figure 25 is the similar change in slope in all the specimens for a load in the range of 8000-9000 N, except the specimen AS090 that presents the opposite behavior (first a decrease in slope and then an increase), but this is most probably due to an abnormal contact between sample, Ni plate and loading jig. The decrease in slope around 8000-9000 N for the other three specimens is associated with the yielding of most of the Ni plate, that starts to be dominant over the other deformation mechanisms (elastic deformation of Ni plate and specimen) around these loads. In Figure 27-C the normal contact stress distribution along the Ni plate as a function of load is presented, extracted from the analytical model presented before (See Section 2.2.4). Also the plastic stress-strain law for benchmark pure annealed Ni with the same yield stress as the one given by the manufacturer (150 MPa) is shown (97). The different curves represent different positions along the Ni plate measured as the angle from the central diameter (the one aligned with the groove), so 0 is the center and 20 the edge of the plate. In the plot, around 8000-9000 N most of the Ni plate (around 80%) is stressed above the yield point so it makes sense that in the load-displacement curve a decrease in the slope is recorded, that is directly related with the shape of the plastic stress-strain law for pure Ni shown in Figure 27-C. Besides, also around 10 kN there is full contact between the BD specimen, the holder and the Ni plate, as it can be observed in Figure 27-B; hence around this load the whole Ni plate is under stress and it will deform.

The final region of interest in the load-displacement curve of the BD specimens is the moment of fracture. The expected behavior is the one shown by sample SPS567. There is a loss of load bearing capability, accompanied with an increase in the displacement that is directly related with the crack mouth opening. After a drop of the load by 1%, the load frame switches to the unloading scheme (See Section 3.6.2.2.2) and the specimen is unloaded until zero load, being the residual displacement representative of the residual crack mouth opening and the permanent plastic deformation of the Ni plate. Another important outcome from the fracture test of specimen SPS567 is the achievement of a controlled crack growth (not sudden drop in load) with a gradual decrease of load as the displacement increases. This is the desired result in terms of modelling for extracting strength and fracture properties of the material by inverse analysis. For the other three specimens, the displacement outcome during fracture was not as expected. Instead of increasing, the displacement decreased during the drop in load (see Figure 25). As no physical phenomenon can explain this behavior, the resultant abnormal displacement has been attributed to an error in the measurement of the extensometer. Probably during fracture, that occurs in a very short period of time, the extensometer moved because of a non-proper contact between the extensometer knife edge and the loading jig. Therefore, the residual displacement after unloading of these three specimens cannot be trusted.

A first conclusion that can be drawn from the results in Figure 25 is that the displacement measurement from the BD test set-up includes many contributions: elastic and plastic deformation of Ni plate, elastic deformation of the sample and errors in the displacement measurement during fracture. This makes complex the comparison of this test results with numerical simulations in order to extract mechanical properties of the material and it could be a reason for proposing other displacement measurement techniques for future developments, like digital image correlation, that can neglect the measurement of undesired deformations and measure directly the displacement of the sample. However, in the BD set-up mechanical properties can be extracted from the load output by using analytical models (See Section 2.2.4), so the extraction of properties does not only rely upon the successful match of experimental results and numerical simulations. The strength or maximum tensile stress of the material can be estimated by using this approach.
As a first step in the application of this analytical model, it was compared with a numerical model based on a linear-elastic FE simulation of the loaded BD sample. For the comparison, the calculations were made using the same geometrical parameters and material properties. In Figure 26 the result of the validation analysis is shown. As it can be seen, the close match between the analytical and numerical solution (error less than 10%) allows to conclude that the use of this analytical model for estimating the strength of the material from the BD test is valid.

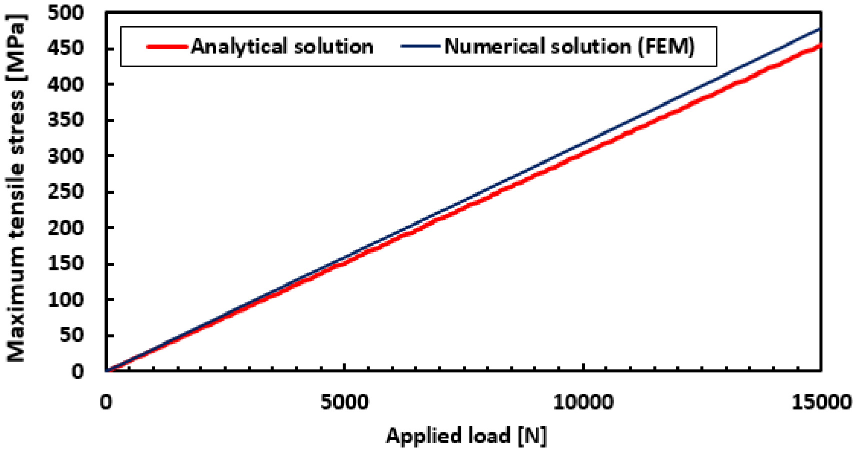

Figure 26 - Validation with FEM analysis of analytical model for extraction of strength from maximum applied load BD specimen

The output from this analytical model is a function that transforms applied load into maximum tensile stress in the specimen. Thus the stress in the area located at the two sides of the central hole and at the bottom of the groove. As an input, the geometry of the specimen (extracted from experimental observation (See Section 3.5.1) and Appendix 4.3), the elastic modulus (taken from the values shown in Section 4.1.1) and the geometric stress concentration factors (from Appendix 2.2) must be introduced in the model. Figure 27-A shows the relation between applied load and maximum tensile stress according to the analytical model. In the region of partial contact, the relation is almost linear and it becomes completely linear in the region of full contact. Figure 27-B and C show the contact length and contact stress as a function of load. These two results, although they are part of the stress calculation, are mainly important for estimating the deformation of the Ni plate, combined with the plastic stress-strain law of the material.

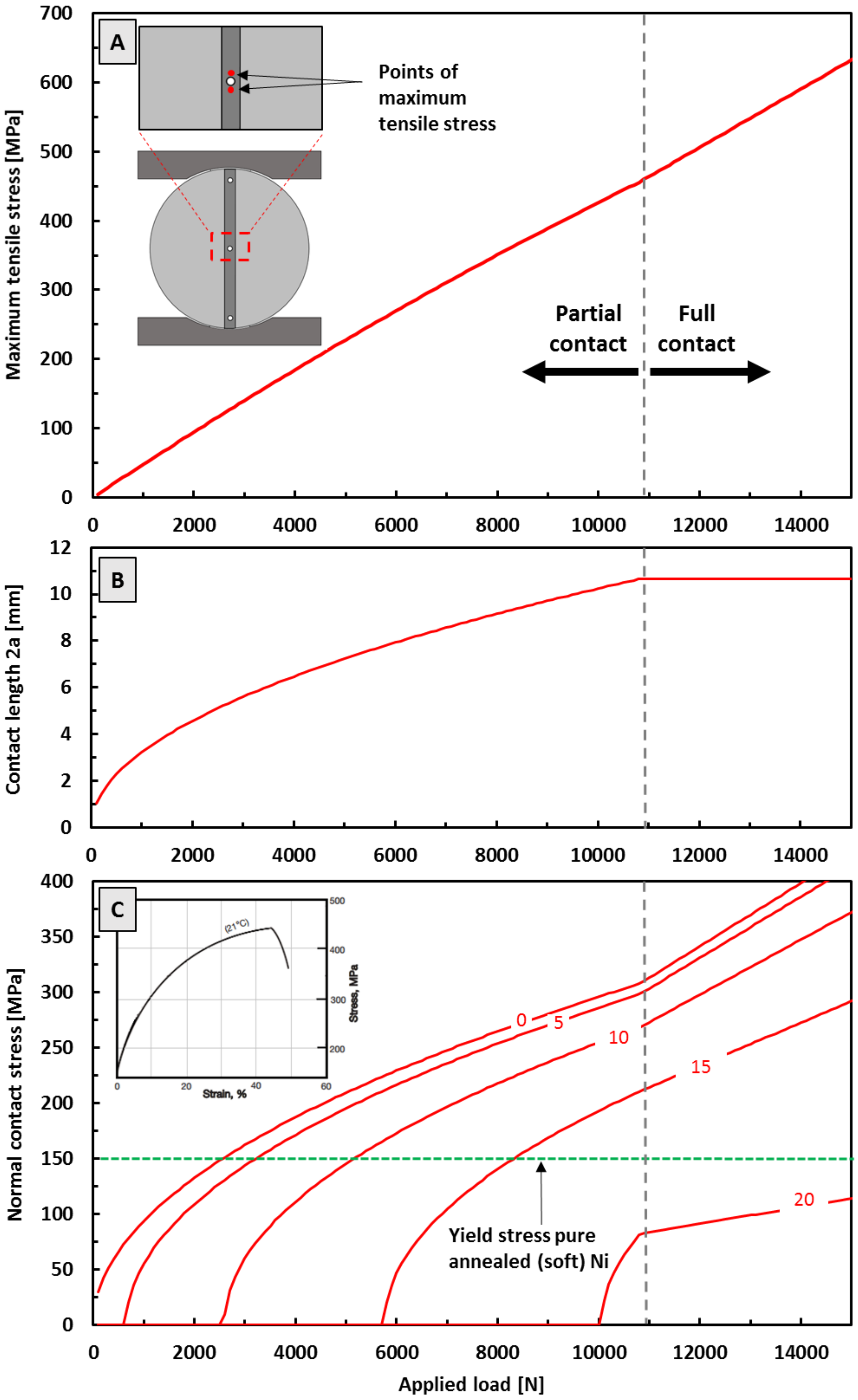

Figure 27 - Relation between maximum tensile stress and applied load (A), contact length as a function of applied load (B) and normal contact stress as a function of applied load (C)

From this model and the maximum applied loads during the test, the strength of the different composites has been calculated and compared with benchmark YSZ samples (See Figure 28). It is important to notice that the benchmark strength for Amperit YSZ must not be compared with the composites because the degree of densification of the pure Amperit YSZ (around 80-90%) is lower than the composites so it is expected to be weaker, besides the fact that YSZ Amperit (4-5 mol% yttria) has essentially lower strength than YSZ Tosoh (3 mol% yttria) because of the lower fracture toughness (85) (98). Therefore, only Tosoh composites are compared with the benchmark. As can be seen in Figure 28, no significant strength variation occurs between the benchmark YSZ and the composites. The addition of the sacrificial MSBA particles does not substantially decrease the performance of the material. The strength is mainly determined, in both the composites and the benchmark, by two factors. One is the geometry of the stress concentration elements (groove and central hole), that act as artificial initial defects. Second, the surface condition after heavy machining for removal of material. The surface flaws are, indeed, the most important factor determining the strength of the material and, during machining, severe damage is introduced in the surface (See Section 3.4.3). An estimation of the size of the initial surface defects can be calculated from Equation 15. Assuming that the geometric factor Y is 0.7 (for elliptical surface cracks), taking a value of fracture toughness of 5 MPam$^{0.5}$ (See Section 4.1.3) and the maximum obtained tensile stress value for pure Tosoh YSZ, 574 MPa, the size of the critical surface crack is estimated to be around 50 μm. This result is in good agreement with the studies of other authors. One of this studies by T. Kosmac et al. (99), in which they test in 3-point bending different YSZ (3 mol% yttria) of the same manufacturer (Tosoh) and with different surface condition. They also obtained a strength value of around 550 MPa for the specimens in which the most loaded surface was previously heavily ground with coarse (150 μm) diamond burr. They also estimate an initial size of the surface crack around 50 μm and they validate this estimation with SEM observation of the fracture surface. Therefore, these results can be used for validating the strength values obtained in the present work. Also it is good to compare the results with the given values in the manufacturer datasheet of the material (100). A value of 1 GPa for the 3-point bending strength is reported, that corresponds to a specimen polished according to the standard JIS R1601, so the size of surface cracks is smaller.

By performing the same estimation using the strength results of the composites, a value of 60-65 μm is estimated for the surface defects in the composite. Therefore, it can be concluded that the addition of particles slightly makes more severe the machining microcracks, but the performance is not greatly decreased overall. Also the slightly lower strength could be due to a small decrease of fracture toughness due to the addition of relatively coarse healing particles.

From Figure 28 it can be also observed that the strength value for the Amperit composites is slightly lower than for Tosoh composites. This could be due to different factors. First, as explained before, the Amperit composites contain YSZ with 4-5 mol% yttria, which is a material that exhibit lower value of fracture toughness (85) (98). The lower strength value might be also related to a much higher grain size that increases the average size of the flaw population in the material. Additionally, the bigger grain size makes the surface of the specimen rougher (See Figure 23).

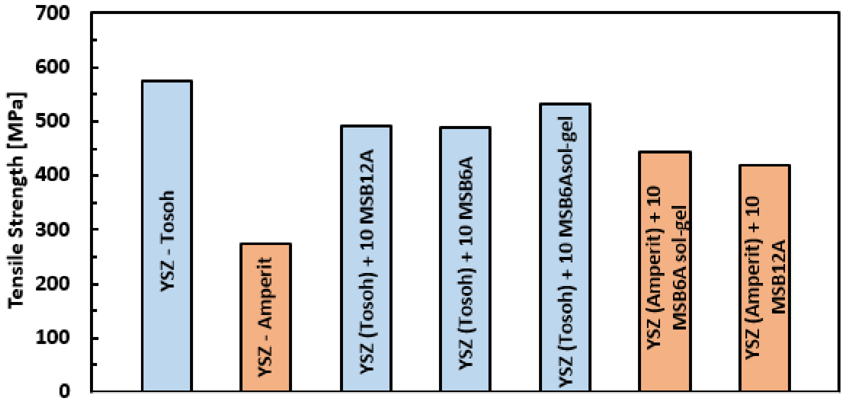

Figure 28 - Tensile strength of YSZ-MSBA composites and comparison with benchmark YSZ

The second main outcome from the BD test is the fracture analysis by optical observation after the test. In general, it can be said that the main objective of the test has been fulfilled because it is observed (See Figure 29) that the crack in each of the specimens does not fully propagate towards both sides of the groove. However, there is a very small amount of material left intact so the specimens are very weak after the fracture test. This is a problem for handling. There is a risk, as well, that the sample breaks during the heat treatment due to thermal stresses in the small intact area of the groove.

In Figure 29 the crack width distribution along the central groove is presented and SEM results showing details of the crack path close to the side holes. From this result, it can be concluded that only specimens SPS556 satisfies the main requirement of this test set-up. The crack initiated in the central hole is arrested in both side holes. This is the reason why the residual displacement after unloading (See Figure 25) is the lowest of all the samples. However, the objective is not completely fulfilled as two new cracks initiate at the other side of the side holes, but they do not propagate until the end.

In the case of the other three specimens the crack has propagated all the way until the end of the groove in one of the sides and it remains intact in the other side; thus, the residual displacement after unloading (See Figure 25) is larger than the one of specimen SPS556. However, there is a difference between the fracture of specimens SPS567 and AS090 and specimen AS058. In the case of samples SPS567 and AS090 the crack initiated in the center propagates until one of the edges of the groove, but in the case of AS058 the crack is arrested in both holes and a new crack initiates at the other side of one of the holes and propagates until the edge so at the end the specimen remains intact only in one of the sides. This is the reason for the lower residual displacement of specimen AS058 as compared with SPS567 and AS090. Additionally, in the sample AS058 any new crack is initiated at the other side of the side hole where the sample remains intact, while in AS090 and SPS567 a new crack initiates but it does not propagate until the end of the specimen.

The previously presented results suggest that future work on the BD test set-up could consider the modification of the test specimen for promoting that the preferential fracture mechanism is the one observed in specimen SPS556 because the crack is arrested in both holes and the maximum crack width is within acceptable limits that allow to heal the material at a reasonable temperature and time. Additionally, a controlled crack of shorter length would be very beneficial for the success of the test because it would reduce the risk of complete specimen fracture during the heat treatment and it would make the sample easier to handle.

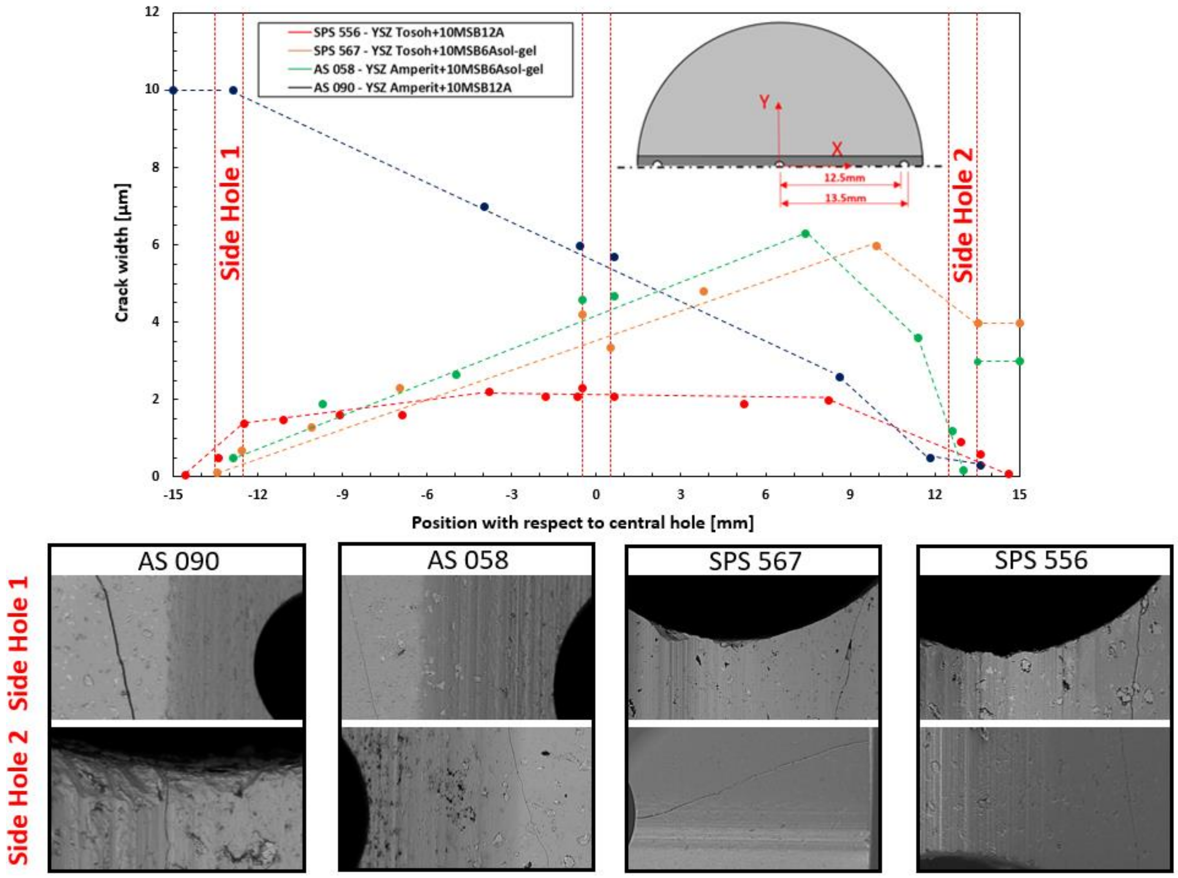

Figure 29 - Crack with distribution after fracture test of the BD specimens

In terms of extraction of mechanical properties, this test proves to be suitable to characterize the fracture behavior of the material through the application of an analytical model that estimates the strength. Besides, the results are in good agreement with observations from other authors.

4.3.2.2 Wedge-Loaded Double Cantilever Beam (WL-DCB) test

The WL-DCB test is the second mechanical test that has been used for quantification of healing in the YSZ-MSBA composite. The material has been tested until fracture in order to create the controlled crack that will be later on healed and re-tested. The measurements done during the fracture test (load, displacements and crack geometry), combined with FE modelling, can be used for extracting mechanical properties of the self-healing material. In particular, the WL-DCB set-up is specially designed for extracting the fracture toughness of the material because of the slow crack growth.

For the WL-DCB test there are no analytical models for extracting mechanical properties out of the test results (See Section 2.2.5). One of the main issues with this test is the way to model frictional effects between the wedge material and the specimen, that introduces a certain degree of uncertainty to the results. The effect of friction also makes the test more complex. In Figure 30 the results of the fracture test of the three tested WL-DCB specimens are presented. By looking at the unloading curves in all the specimens, it can be seen that the slope of the curves does not follow an expected trend, that should be parallel or of lower slope (due to loss of stiffness after facture) than the slope of the loading curve. Instead, for a very small displacement the reaction load on the wedge reaches almost zero. This is due to the friction between the wedge and the specimen. During unloading the specimen gets stuck in the wedge and it follows the displacement of the wedge. This is the reason for the fast drop in load during unloading. Therefore, the resulting residual displacement after complete unload is mostly related to the friction and not to the residual crack opening width. This presents an issue because the objective of performing an unloading scheme is to record the residual stiffness of the specimen after fracture and also the residual crack width. Anyhow, the crack width can be also studied by optical observation after testing. A second consequence of the friction between the wedge and the sample is the effect on the loading curves during test. As it can be seen in Figure 30, the loading curve of the specimen AS024 is different than the ones of the other two specimens, which are similar. In principle, the shape of the loading curve depends on the elastic behaviour of the material, that is the same for the three specimens, and the friction. In order to ensure the same friction coefficient for all the specimens, a layer of Vaseline was applied in the wedge surface prior to test. However, the resultant load-displacement curve of specimen AS024 suggests that there was a change in the friction conditions during the test and this could be the reason for the change is slope. However, other factors might have caused this change in slope like the rotation of the specimens during loading.

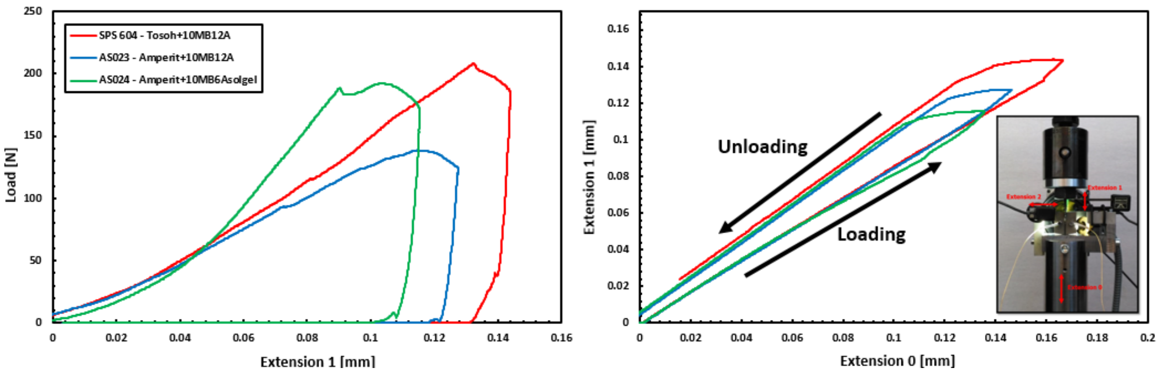

Figure 30 - Load and displacement measured in fracture test of WL-DCB specimens (left). Relation between displacement 1 and displacement 0 (right).

Despite the drawbacks from the frictional effects, these results from the WL-DCB test show great potential for the quantification of strength recovery of self-healing brittle materials as the main objective of the test has been fulfilled, which is the slow and controlled growth of the crack. This is something, in general, achievable with Double Cantilever Beam specimens, but the addition of the chevron notch and the crack guidance groove further help to have a controlled and slow growth. The function of the chevron notch is to create a decreasing stress intensity factor while the crack propagates towards the end of the guidance groove. In Figure 30 the achievement of the slow crack growth can be clearly seen in the load-displacement curves of the three specimens. The gradual decrease of the load for higher displacements is a proof that a controlled crack can be created with the WL-DCB specimens. Besides, there is a higher range for quantifying the strength recovery, in comparison with the BD method. The drop in load and the decrease of stiffness are larger in the WL-DCB test, so there is a higher difference between the virginal and residual strength.

The test was initially set to stop after a drop in load of 10 N (See Section 3.6.2.2.1), however the optical analysis of the cracks after test shows that they did not reach the bottom of the guidance groove in any of the cases, as it can be seen in Figure 31. Therefore, the test could be set to stop at an even higher drop in load in order to have a higher stiffness range for quantification of recovery of load bearing capability. This is equivalent to say that in future developments even more damage can be introduced in the WL-DCB specimens, as compared with the damage introduced in the test already performed.

Figure 31 shows the results of the analysis of crack geometry after test. The crack width has been measured in several points along the crack guidance groove until reaching the point where the crack stops. As mentioned before, in any of the cases the crack reaches the bottom of the crack guidance groove, while all the cracks reached and passed the end of the chevron notch. The specimen AS024 exhibits the longest crack. It is interesting to compare this result with the ones in Figure 30. By comparing the load-displacement curves of the three specimens during fracture it can be seen that the specimen AS024 exhibits the largest displacement, which is in accordance with the obtained crack geometry. Because the crack propagated more during loading, the sample lost more stiffness so the wedge could go deeper into the sample. This is the reason for the larger displacement observed in Figure 30. In the other hand, the lengths of the cracks in specimens AS023 and SPS604 are similar, which is related to the almost equal resultant displacement during fracture (drop in load).

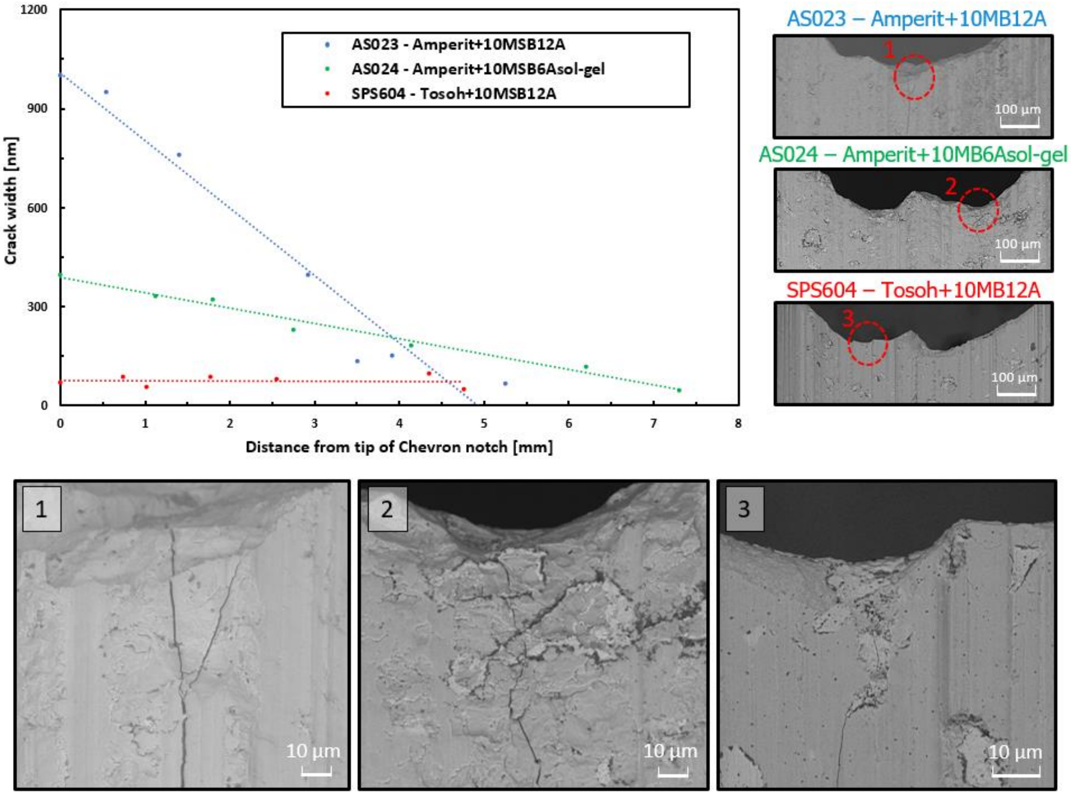

Figure 31 - Crack width distribution after fracture test of WL-DCB specimens

The larger crack length in the specimen AS024 could be explained from the fact that this specimen has been manufactured from Amperit powder, that contains around 5 mol% yttria and preferentially forms the t’ phase (See Section 4.1.1). This phase does not exhibit the toughening mechanism based on stress-induced phase transformation from tetragonal to monoclinic (101), associated with a volume expansion of around 5% that tends to close the crack. This leads to a lower fracture toughness of the material with higher yttria content, as it has been shown by other authors (85). However, it has been reported that the t’ phase might exhibit a different toughening mechanism based on ferroelastic domain shifting (98), so a clear conclusion cannot be drawn about what mechanism predominates over the other. In any case, the general trend is that higher contents of yttria decrease the fracture toughness (98). Therefore, this could be the explanation for the longer crack as compared with specimen SPS604, that has been manufactured with Tosoh 3 mol% yttria powders.

Following the same approach, a longer crack should be also observed in the specimen AS023, but a crack of similar length than specimen SPS604 is observed instead. One possible explanation for this can be the fact that crack initiation point is different in specimen AS023, comparing with the crack initiation points in specimens AS024 and SPS 604. This different crack initiation point is mainly related to the different shape of the chevron notch tip (See Figure 31), that is difficult to make reproducible due to the machining process. The central peak in the tip curvature observed in AS024 and SPS604 displaces the point of maximum stress to the bottom of the two valleys created in the tip, so this is where the crack initiates. However, in AS023 the crack initiates in the center of the chevron notch because it is the most stressed area. This could be the reason for the shorter but wider crack as compared with AS024.

Another important outcome from this test, also observed in the results of the fracture test in the BD specimens, is that there is not a big difference between the load bearing capability of the composites made with Tosoh matrix (3 mol% yttria) and Amperit matrix (5 mol% yttria). Because of the previously explained phenomenon (transformation toughening), normally the reported strength values for YSZ containing 3 mol% yttria are higher than for YSZ with higher yttria contents (85). Also the bigger grain size in the Amperit composites (20-50 times higher) could contribute to decrease the strength. However, the fact that this is not the case in both the WL-DCB and BD test suggests that the strength (maximum load) measured for these samples is mainly determined by the geometry of the specimens and the surface finishing. In the WL-DCB test the length from the top of the specimen to the tip of the chevron counts theoretically as an initial crack mouth opening. Therefore, the length of the crack initiated during testing is negligible with respect to this initial and “artificial” crack created in the sample. The same applies to the grooves machined in the BD samples. This is an advantage because it improves the statistical analysis of strength and, thus, provides a better quantification of healing efficiency for the brittle materials.

As a conclusion, it can be said that the WL-DCB test is a suitable test method for quantification of healing in self-healing brittle materials, because of three reasons: a controlled and slow-growing crack can be achieved. The crack size (width) is lower than 1 μm, which desirable for fully healing the crack within a reasonable time and temperature. Also, since the crack does not reach the bottom of the crack guidance groove, the specimen is quite intact after testing and can be easily handled. Third, the specimen has several degrees of freedom of rotation so it is easier to align, comparing with the BD specimens. Nevertheless, an important drawback from this test is the difficulty to extract mechanical properties due to the uncertainties related to modelling the frictional effects. Besides, there are no analytical models for extraction of mechanical properties so the analysis depends on numerical simulations.

5 Conclusions and Recommendations

5.1. Conclusions

First, the microstructure and healing potential of the alumina encapsulated $MoSi_2B$-based YSZ composite (YSZ-MSBA) has been studied. Next, several methods have been employed for mechanical characterization of the self-healing composites. In this section the main findings are summarized.

The initial composition of the healing particles before sintering does not correspond with the thermodynamic equilibrium for the designed composition of the particles. According to the designed composition, the healing particles containing 6 wt% Al and 12 wt% Al should exhibit a fully hexagonal crystal structure. Instead, the initial healing particles before sintering contain also a small amount of tetragonal phase. This means that during synthesis of the material for the alumina encapsulated $MoSi_2B$-based particles (by melting, casting and subsequent grinding to powders) the Al is not homogeneously distributed in the material. The Al-poor areas have a tetragonal phase after solidifying and the rest has a hexagonal phase. The tetragonal-$MoSi_2$ particles have a poor encapsulation. No alumina shell is created at the surface of boride phases in the healing particles.

Cracks in YSZ-MSBA composites generated by indentation were healed upon exposure to 1100 ºC in laboratory air for 1, 4 and 16 h by SiO_2 that fills the cracks and reacts with the YSZ matrix to form $ZrSiO_4$. In some cases, also Al_2O_3 filled the cracks due to oxidation of remaining Al in the particles. In most of the cases, cracks fractured the healing particles and triggered the healing reaction.

Two novel test methods are proposed to determine the mechanical properties of self-healing ceramics, namely: the Brazilian Disc (BD) test and the Wedge-Loaded Double Cantilever Beam (WL-DCB) test. Controlled crack growth could be achieved in brittle Yttria-Stabilized Zirconia with the two methods.

The BD test is a straightforward method for extraction of mechanical properties of the self-healing material. An analytical model, validated with finite elements analysis, has been used for determining strength of the material. A strength value of around 550 MPa is obtained for the benchmark fully dense YSZ material. The obtained value is reasonable and comparable with other studies reported in literature. The slight difference between the strength of pure YSZ and $MoSi_2B$-based YSZ composites suggests that the addition of healing particles to the TBC does not have a significant effect on the overall strength at room temperature of the material. The results of the tests indicate that the quantification of healing might present the following difficulties. First, the width of the crack (around 5 µm) is relatively large for achieving a complete healing within a reasonable time and temperature. Then, the length of the created crack is almost the size of the diameter. Thus, the integrity of the specimen is compromised due to the small amount of material intact. Also the load drop of around 1 % gives a short range for quantification of healed strength.

The WL-DCB test presents more advantages from the point of view of quantification of healing. A slow-growing and controlled crack is achieved, instead of the almost sudden drop in load of the BD test. Hence, a larger range for quantification of healed strength is obtained. Also the slow crack growth allows to tune the degree of damage that is introduced in the material. Another advantage is that the created cracks are less than 1 μm wide so that the material can be healed within reasonable time and at reasonable temperature. After creating the crack, the specimens remain intact making its handling safer. However, the WL-DCB test presents more difficulties when determining the mechanical properties due to the uncertainties associated with modeling the friction between the wedge and the specimen. Since there are no analytical models for the extraction of properties, this technique relies on the use of inverse analysis through numerical modeling.

The elastic modulus of the YSZ-MSBA composite was studied by means of depth-sensing indentation techniques. A value of 212 GPa was obtained for fully dense benchmark YSZ and a value in the range of 125-160 GPa for porous YSZ, assuming a porosity volume fraction of 10-15 %, which is the typical value for APS TBCs. Young’s modulus values of 440, 375 and 350 GPa were obtained for tetragonal-$MoSi_2$, hexagonal-$MoSi_2$-6 wt%Al and hexagonal-$MoSi_2$-12 wt%Al, respectively. These values can be validated with data from literature. A rule of mixtures for predicting the Young’s modulus of the composite was deviced from the experimental results. A value of 230 GPa is predicted for composites containing tetragonal-$MoSi_2$ particles. An estimated value of 226 and 224 GPa for composites containing hexagonal-$MoSi_2$ particles with 6 and 12 wt%Al, respectively. The rule of mixtures has been validated with experimental results for composites containing 10 vol.% of hexagonal-$MoSi_2$ particles containing 6 wt% Al. The experimental Young’s modulus is 225±25 GPa.

5.2. Recommendations

The microstructure of the healing particles needs optimization by tuning initial composition and processing conditions. The manufacturing of monolithic $MoSi_2$ alloyed with Al and B (in substitution of Si) via spark plasma sintering (SPS) shows good results as they are in accordance with the thermodynamic equilibrium. Hence, one option could to produce monolithic $MoSi_2$ plates (from the as received powders of the external manufacturer) with SPS and grind to powders, followed by mixing and sintering of the composites.

The BD test should be improved by making the controlled cracks shorter and narrower. This could be achieved by making changes in the geometry of the sample and set-up and using the support of numerical modeling. The position and size of the side holes for crack arrest could be changed. Also, it could be considered to make larger the curved area of contact between the holder and the specimen in such a way that the compressive stresses in the load introduction area are made higher.

To avoid the strong influence of the deformation of the Ni plates that accommodate the specimen in the loading jigs in the BD test, the lateral displacement should be used as input for the numerical simulations. This lateral displacement can be measured by means of an extensometer placed in the two edges of the diameter perpendicular to the groove of the specimen. As an alternative, digital image correlation may be considered for measuring the displacement field in the sample.

Regarding the determination of elastic modulus with depth-sensing indentation techniques, more experiments for validation could be considered in order to have a more sound model. Although it is not applicable to the real application, composites with 20, 30, etc. vol.%. particles can be prepared and tested for validating the rule of mixtures.

References

1. **Timoshenko, S. .** *Strength of Materials. Part I: Elementary theory and problems, Second Edition.* D. Van Nostrand Company, 1940.
2. **Nicholls, J. R. .** *Advances in coating design for high performance gas turbines.* Materials Research Society Bulletin, 2003.
3. **Sloof, W. G. .** *Self-healing in coatings at high temperature.* Self Healing Materials, an Alternative Approach to 20 Centuries of Materials Science, 2007.
4. **Padture, N. P. , Gell, M. and Jordan, E. H. .** *Thermal barrier coatings for gas-turbine engine applications.* Science, 2002.
5. **Marino, K. A. , Hinnermann, B. and Carter, E. A. .** *Atomic-scale insight and design principles for turbine engine thermal barrier coatings from theory.* Proceedings of the National Academy of Sciences, 2011.
6. **Chen, L. B. .** *Yttria-stabilized zirconia thermal barrier coatings - a review.* Surface Review and Letters, 2006.
7. **Hille, T. S. , Turteltaub, S. and Suiker, A. S. J. .** *Oxide growth and damage evolution in thermal barrier coatings.* Engineering Fracture Mechanics, 2011.
8. **Sloof, W. G. , Turteltaub, S. , Carabat, A. L. , Derelioglu, Z. , Ponnusami, S.A. and Song, G. M. .** *Crack healing in yttria stabilized zirconia thermal barrier coatings.* IOS Press, 2015.
9. **Osada, T. , Nakao, W. , Takahashi, K. and Ando, K. .** *Self-crack-healing behavior in ceramic matrix composites.* Woodhead Publishing Limited, 2014.
10. **Van der Zwaag, S. and Brinkman, E. .** *Introduction to self-healing materials and the IOP Self-Healing Materials program.* IOS Press, 2015.
11. **Van der Zwaag, S. .** *Self Healing Materials: an alternative approach to 20 centuries of materials science.* Springer, 2007.
12. **Derelioglu, Z. , Carabat, A. L. , Song, G. M. , van der Zwaag, S. and Sloof, W. G .** *On the use of B-alloyed $MoSi_2$ particles as crack healing agents in yttria stabilized zirconia thermal barrier coatings.* Journal of the European Ceramic Society, 2015.
13. **Takahashi, K. , Chu, M. , Kim, B. , Sato, S. and Ando, K. .** *Crack-healing behavior and static fatigue strength of Si_3N_4/SiC crack-healed under cyclic stress.* Journal of the European Ceramic Society, 2003.
14. **Osada, T. , Nakao, W. , Takahashi, K. , Ando, K. and Saito, S. .** *Strength recovery behavior of machined Al_2O_3/SiC nano-composite ceramics by crack-healing.* Journal of the European Ceramic Society, 2007.
15. **Li, S. , Song, G. , Kwakernaak, K. , van der Zwaag, S. and Sloof, W. G. .** *Multiple crack healing of a Ti_2AlC ceramic.* Journal of the European Ceramic Society, 2005.
16. **Ashby, M. J. .** *Materials Selection in Mechanical Design, Forth edition.* Elsevier, 2011.
17. **Mackenzie, J. K. .** *The elastic constants of a solid containing spherical holes.* Proceedings of the Physical Society, 1950.
18. **Green, D. J. .** *An introduction to the mechanical properties of ceramics.* Cambridge Solid State Science Series, 1998.
19. **Spriggs, R. M. .** *Expression for effect of porosity on elastic modulus of polycrystalline refractory materials, particularly aluminum oxide.* Journal of the American Ceramic Society, 1961.
20. **Ramakrishnan, N. and Arunachalam, V. S. .** *Effective elastic moduli of porous ceramic materials.* Journal of the American Ceramic Society, 1993.
21. **Phani, K. K. and Niyogi, S. K. .** *Young's modulus of porous brittle solids.* Journal of Materials Science, 1987.

22. **Roberts, A. P. and Garboczi, E. J. .** *Elastic properties of model porous ceramics.* Journal of the American Ceramic Society, 2000.
23. **Flinn, B. D. , Bordia, R. K. , Zimmermann, A. and Rödel, J. .** *Evolution of defect size and strength of porous alumina during sintering.* Journal of the European Ceramic Society, 2000.
24. **Danzer, R. , Lube, T. , Morrell, R. and Supancic, P. .** *Mechanical Properties of Ceramics.* Handbook of Advanced Ceramics, Elsevier, 2013.
25. **Boley, B. A. and Weiner, J. H. .** *Theory of thermal stresses.* Krieger Publishing Company, 1983.
26. **Griffith, A. A. .** *The phenomena of rupture and flow in solids.* Philosophical Transactions of the Royal Institution of Naval Architects, 1920.
27. **Irwin, G. R. .** *Fracture dynamics.* American Society for Metals, 1948.
28. **Orowan, E. .** *Fracture and strength of solids.* Report of Progress in Physics, 1949.
29. **Quinn, G. D. .** *Mechanical testing of ceramics.* Elsevier, 2016.
30. **Keysight Technologies.** *The revolutionary impact of the Oliver and Pharr technique: on the science of hardness testing.*
31. **Doerner, M. F. and Nix, W. D. .** *A method for interpreting the data from depth-sensing indentation instruments.* Journal of Materials Research, 1986.
32. **Oliver, W. C. and Pharr, G. M. .** *Measurement of hardness and elastic modulus by instrumented indentation: advances in understanding and refinements to methodology.* Journal of Materials Research, 2004.
33. **Shuman, D. J. , Costa, A. L. M. and Andrade, M. S. .** *Calculating the elastic modulus from nanoindentation and microindentation reload curves.* Materials Characterization, 2007.
34. **European Committee for standardization.** *Metallic materials - instrumented indentation test for hardness and materials parameters - Part1: Test method. EN ISO 14577-1.* 2015.
35. **Bolshakov, A. and Pharr, G. M. .** *Influences of pileup on the measurement of mechanical properties by load and depth sensing techniques.* Journal of Materials Research, 1998.
36. **Li, X. and Blushan, B. .** *A review of nanoindentation continuous stiffness measurement technique and its applications.* Materials Characterization, 2002.
37. **Keysight Technologies.** *Continuous Stiffness Measurement (CSM) option.*
38. **ASTM International.** *Standard test method for Vickers indentation hardness of advanced ceramics. C 1327 - 99.* 1999.
39. **Quinn, G. D. and Bradt, R. C. .** *On the Vickers indentation fracture toughness test.* Journal of the American Ceramic Society, 2007.
40. **Feng, Y. and Zhang, T. .** *Determination of fracture toughness of brittle materials by indentation.* Acta Mecanica Solida Sinica.
41. **Nastic, A. , Merati, A. , Bielawski, M. , Bolduc, M. , Fakolujo, O. and Nganbe, M. .** *Instrumented and vickers indentation for the characterization of stiffness, hardness and toughness of zirconia toughened Al_20_3 and SiC armor.* Journal of Materials Science and Technology, 2015.
42. **Niihara, K. .** *A fracture mechanics analysis of indentation-induced Palmqvist crack in ceramics.* Journal of Materials Science Letters, 1983.
43. **Anselmi-Tamburini, U. , Garay, J. E. , Munir, Z. A. , Tacca, A. , Maglia, F. , Chiodelli, G. and Spinolo, G. .** *Spark plasma sintering and characterization of bulk nanostructures fully stabilized zirconia: Part II. Characterization studies.* Materials Characterization, 2004.

44. **Glandus, J. C. and Rouxel, T. .** *Study of the Y-TZP toughness by an indentation method.* Ceramics International, 1991.
45. **Kaliszewski, M. S. , Behrens, G. , Heuer, A. H. , Shaw, M. C. , Marshall, D. B. , Dransmann, G. W. , Steinbrech, R. W. , Pajares, A. , Guiberteau, F. , Cumbrera, F. L. and Domingo-Rodriguez, A. .** *Indentation studies on Y_2O_3-stabilized ZrO_2: I, Development of indentation-induced cracks.* Journal of the American Ceramic Society, 1994.
46. **Niihara, K., Morena, R. and Hasselman, D. P. H. .** *Evaluation of K_{IC} of brittle solids by the indentation method with low crack-to-indent ratios.* Journal of Materials Science Letters, 1982.
47. **Evans, A. G. and Charles, E. A. .** *Fracture Toughness Determination by Indentation.* Journal of the American Ceramic Society, 1976.
48. **Anstis, G. R. , Chantikul, P. , Lawn, B. R. and Marshall, D. .** *A critical evaluation of indentation techniques for measuring fracture toughness: I. Direct crack measurement.* Journal of the American Ceramic Society, 1981.
49. **Carneiro, F. L. L. B. and Barcellos, A. .** *Concrete tensile strength.* Union of Testing and Research Laboratories for Materials and Structures, 1953.
50. **Hertz, H.** *Gesammelte Werke (Collected Works), Leipzig.* 1895.
51. **Hondros, G. .** *The evaluation of Poisson's ratio and the modulus of materials of a low tensile resistance by Brazilian (indirect tensile) test with particular reference to concrete* . Australian Journal of Basic and Applied Science, 1959.
52. **Japaridze, L. .** *Stress-deformed state of cylindrical specimens during indirect tensile strength testing.* Journal of Rock Mechanics and Geotechnical Engineering, 2015.
53. **Pilkey, W. D. and Pilkey, D. F. .** *Peterson's stress concentration factors, third edition.* John Wiley & Sons.
54. **Schijve, J. .** *Fatigue of Structures and Materials, Second Edition.* Springer, 2008.
55. **Odette, G. R. , He, M. Y. and Hribernik, M. L. .** *A chevron notched wedge loaded double cantilever beam test method to measure the initiation and arrest fracture toughness of semibrittle materials with small specimens.* Fusion Materials Semiannual Progress Report, DOE-ER-0313/42, 2007.
56. **Brown, E. N. , White, S. R. and Sottos, N. R. .** *Fatigue crack propagation in microcapsule-toughened epoxy.* Journal of Materials Science, 2006.
57. **Rahmathullah, M. A. M. and Palmese, G. R. .** *Crack-healing behavior of epoxy-amine thermosets.* Journal of Applied Polymer Science, 2009.
58. **Chen, X. , Wudl, F. , Mal, A. K. , Shen, H. and Nutt, S. R. .** *New thermally remendable highly cross-linked polymeric materials.* Macromolecules, 2003.
59. **Freiman, S. W. and Mecholsky, J. J. .** *The fracture of brittle materials.* Wiley, 2012.
60. **Skocek, J. and Stang, H. .** *Inverse analysis of the wedge-splitting test.* Engineering Fracture Mechanics, 2008.
61. **Jin, S., Gruber, D. and Harmuth, H. .** *Determination of Young's modulus, fracture energy and tensile strength of refractories by inverse estimation of a wedge splitting procedure.* Engineering Fracture Mechanics, 2014.
62. **Carabat, A. L., van der Zwaag, S. and Sloof, W. G. .** *Creating a protective shell for reactive $MoSi_2$ particles in high-temperature ceramics.* Journal of the American Ceramic Society, 2015.
63. **Tokita, M. .** *Spark plasma sintering (SPS) method, systems, and applications.* Handbook of Advanced Ceramics, Elsevier Inc., 2013.

64. **Dahl, P. , Kaus, I. , Zhao, Z. , Johnsson, M. , Nygren, M. , Wiik, K. , Grande, T. and Einarsrud, M.-A. .** *Densification and properties of zirconia prepared by three different sintering techniques.* Ceramics International, 2007.
65. **Kessel, H. U. , Hennicke, J. , Kirchner, R. and Kessel, T. .** *Rapid sintering of novel materials by FAST/SPS - Further development to the point of an industrial production process with high cost efficiency.* FCT Systeme GmbH.
66. **Li, K. and Liao, T. W. .** *Surface/subsurface damage and the fracture strength of ground ceramics.* Journal of Materials Processing Technology, 1996.
67. **Roberts, S. G. .** *Depths of cracks produced by abrasion of brittle materials.* Scripta Materialia, 1998.
68. **Osada, T. , Takahashi, K. , Ando, K. and Nakao, W. .** *Advanced machining process using self-healing of machining-induced cracks in mullite/silicon carbide composites.* 2016.
69. **Davis, J. R. .** *Handbook of Thermal Spray Technology.* ASM International, 2004.
70. **Bruce, R. W. , Skelly, D. W. , Viguie, R. and Wortman, D. J. .** *Thermal barrier coating system, EP0987345A1.* European Patent Office, 2000.
71. **Witz, G. , Shklover, V. , Steurer, W. , Bachegowda, S. and Bossmann, H. .** *Phase evolution in yttria-stabilized zirconia thermal barrier coatings studied by Rietveld refinement of x-ray powder diffraction patterns.* Journal of the American Ceramic Society, 2007.
72. **Chin, S. , Anton, D. L. and Giamei, A. F. .** *Advanced $MoSi_2$ compositions.* Final Technical Report for Air Force Office of Scientific Research, 1996.
73. **Liu, X. , Ren, Y. , Xu, H. and Zhao, Z. .** *First-principle investigations on electronic structures and elastic properties of Al-doped $MoSi_2$.* Journal of South University of Technology, Springer, 2010.
74. **Sharif, A. A. , Misra, A. , Petrovic, J. J. and Mitchell, T. E. .** *Alloying of $MoSi_2$ for improved mechanical properties.* Intermetallics, 2001.
75. **Maloy, S. , Heuer, A. H. , Lewandowski, J. and Petrovic, J. .** *Carbon additions to molybdenum disilicide: improved high-temperature mechanical properties.* Journal of the American Ceramic Society, 1991.
76. **Morris, D. G. , Leboeuf, M. and Morris, M. A. .** *Hardness and toughness of $MoSi_2$ and $MoSi_2$-SiC composites prepared by reactive sintering of powders.* Materials Science and Engineering, 1998.
77. **Turchi, P. E. A. and Landa, A. I. .** *Thermodynamic database, lower length scale, Part II: thermodynamic assessment of Al-Mo-Si-U (M3MS-12LL0602092).* Lawrence Livermore National Laboratory, 2012.
78. **Kriegel, M. J. , Foerster, W. , Chmelik, D. , Fabrichnaya, O. , Januschewsky, J. , Kathrein, M. , Sigl, L. S. and Rafaja, D. .** *Diffusion path and growth of intermediate phases in Mo/(Si,B) diffusion couples.* 18th Plansee Seminar, 2013.
79. **Ponnusami, S. A., Turteltaub, S. and Van der Zwaag, S. .** *Cohesive-zone modelling of crack nucleation and propagation in particulate composites.* Engineering Fracture Mechanics, 2015.
80. **Jian, S. , Chang, H. , Tseng, Y. , Chen, P. and Juang, J. .** *Structural and nanomechanical properties of $BiFeO_3$ thin films deposited by radio frequency magnetron sputtering.* Nanoscale Research Letters, 2013.
81. **Luo, J. and Stevens, R. .** *Porosity-dependence of elastic moduli and hardness of 3Y-TZP ceramics.* Ceramics International, 1998.
82. **Nakamura, M., Matsumoto, S. and Hirano, T. .** *Elastic constants of $MoSi_2$ and WSi_2 single crystals.* Journal of Materials Science, 1990.

83. **Westbrook, J. H. and Fleischer, R. L. .** *Intermetallic compounds: basic mechanical properties and lattice defects of intermetallic compounds.* Wiley, p.13, 2000.
84. **Ingel, R. P. and Lewis III, D. .** *Elastic anisotropy in zirconia single crystals.* Journal of the American Ceramic Society, 1988.
85. **Kondoh, J. , Shiota, H. , Kawachi, K. and Nakatani, T. .** *Yttria concentration dependence of tensile strength in yttria-stabilized zirconia.* Journal of Alloys and Compounds, 2004.
86. **Wang, Y. , Duncan, K. , Wachsman , E. D. and Ebrahimi, F. .** *The effect of oxygen vacancy concentration on the elastic modulus of fluorite-structures oxides* . Solid State Ionics, 2007.
87. **Arvanitis, A. .** *Development of multiphase Mo-Si-Al intermetallic alloys.* University of Surrey, 2001.
88. **Tanaka, K. , Nawata, K. , Inui, H. , Yamaguchi, M. and Koiwa, M. .** *Temperature dependence of single-crystal elastic constants of* $Mo(Si, Al)_2$. Intermetallics, 1998.
89. **Qiao, Y. , Zhang, H. , Hong, C. and Zhang, X. .** *Phase stability, electronic structure and mechanical properties of molybdenum disilicide: a first-principles investigation.* Journal of Physics D: Applied Physics, 2009.
90. **Cottom, B. A. and Mayo, M. J. .** *Fracture toughness of nanocrystalline* ZrO_2 *- 3mol%* Y_2O_3 *determined by Vickers indentation.* Scripta Materialia, 1996.
91. **Wade, R. K. and Petrovic, J. J. .** *Fracture Modes in* $MoSi_2$. Journal of the American Ceramic Society, 1992.
92. **Shimizu, H. , Yoshinaka, M. , Hirota, K. and Yamaguchi, O. .** *Fabrication and mechanical properties of monolithic* $MoSi_2$ *by spark plasma sintering.* Materials Research Bulletin, 2002.
93. **Li, H. and Bradt, R. C. .** *The indentation load/size effect and the measurement of the hardness of vitreous silica.* Journal of Non-Crystalline Solids, 1992.
94. **Nix, W. D. and Gao, H. .** *Indentation size effects in crystalline materials: a law for strain gradient plasticity.* Journal of the Mechanics and Physics of Solids, 1998.
95. **Swadener, J. G. , George, E. P. and Pharr, G. M. .** *The correlation of the indentation size effect measured with indenters of various shapes.* Journal of the Mechanics and Physics of Solids, 2002.
96. **Lo, W. , Campbell, A. M. , Luo, J. and Stevens, R. .** *Indentation-induced deformation and microcracking of highly textured superconducting* $(Bi, Pb)_2Sr_2Ca_2Cu_3O_x$ *ceramic.* Journal of Materials Research, 1995.
97. **SpecialMetals.** *Material Database - Nickel 200 & 201 (UNS N02200/W.Nr. 2.4066).*
98. **Mercer, C. , Williams, J. R. , Clarke, D. R. and Evans, A. G. .** *On a ferroelastic mechanism governing the toughness of metastable tetragonal-prime (t') yttria-stabilized zirconia.* Proceedings of the Royal Society A, 2007.
99. **Kosmac, T. , Oblak, C. , Jevnikar, P. , Funduk, N. and Marion, L. .** *The effect of surface grinding and sandblasting on flexural strength and reliability of Y-TZP zirconia ceramic.* Dental materials, 1999.
100. **Tosoh Corporation.** *Tosoh zirconia powder, specification and typical properties, grades: TZ-3Y, TZ-3YS, TZ-3YB, TZ-3YSB.*
101. **Barsoum, M. W. .** *Fundamentals of ceramics.* Series in Materials Science and Engineering, IOP Publishing, 2003.